Work function modification studies for energy applications:

from surface chemical functionalisation to plasmonic tuning

Hugo Domínguez Andrade

School of Physics

May 2017

A thesis submitted to the University of Bristol in accordance with the requirements for award of the degree of Doctor of Philosophy in the Faculty of Science, School of Physics.

Main text word count ≈ 42000

Abstract

This thesis studies the modification of the surface work function from the perspective of its potential application to the field of energy generation. In this case, improving thermionic electron emission from diamond surfaces is the focus of this thesis, as a diamond based device can be used for power generation when implemented as a thermionic energy converter. The success of diamond-based thermionic energy converters strongly relies on the quality and stability of the diamond surface, which has to provide a low work function and a negative electron affinity. These characteristics, low work function and negative electron affinity, are achieved by terminating the diamond surface with a monolayer of hydrogen. However, the poor stability of this surface at high temperatures, at which a thermionic energy converter would operate, is the main drawback for the successful development of diamond-based devices.

Thermionic emission from diamond surfaces was studied, culminating with the proposal of a new theoretical model for thermionic emission from hydrogenated diamond surfaces. This new model, to the best of the author's knowledge, is the first to successfully reproduce the behaviour of the thermionic emission current from hydrogenated diamond surfaces, including the decrease of emission current due to the desorption of hydrogen. As a consequence, the new model allows the extraction of additional information about the surface properties of diamond, like the hydrogen activation energy of desorption E_d or the Richardson constant A. Additionally, it is now possible to relate the components of the emission current with certain surface phases or chemical states of hydrogen on the diamond surface. This finding led to the conclusion that, for <100> single crystal diamond, most of the emission at high temperatures comes from flat terraces with a C(100)-(2×1):H reconstruction. Therefore, in order to improve thermionic emission from diamond, surface treatments should be applied to the surface to promote the formation of this surface phase. In addition, single crystal diamond proved to be a much better emitter than polycrystalline diamond by emitting 1.5 mA/cm^2 as compared to 0.3 mA/cm^2 emitted by the polycrystalline diamond.

An alternative method for the modification of the surface work function was investigated in order to assess its potential application to diamond surfaces. This method consists on the use of light excited plasmo-electric potentials. This phenomenon is quite novel, so the research on this thesis is more focused on increasing our understanding of the physics of this effect that on its immediate application to diamond surfaces. Hence, plasmo-electric potentials on silver nanoplates deposited on indium-tin-oxide were analysed. By studying the transient behaviour of plasmo-electric potentials, it was found that they are surprisingly long ($\tau \approx 100$ s), which is unusual for a plasmonic-based effect, that normally operates on the picosecond regime. It was concluded that this was caused by the charge transport characteristics of the nanoplate-substrate interface. This is because plasmo-electric potentials are caused by the transfer of electrons in or out the nanoplate, which modifies its electrochemical potential and in turn its work function. Moreover, it was found that plasmo-electric potentials are present on the same nanoplate with opposite signs, which is believed to be caused by impurities deposited on the surface of the nanoplate. Lastly, in order to apply plasmo-electric potentials to improve thermionic emission more research is needed to better understand the physics of this phenomenon. However, it was found that plasmo-electric potentials could have a strong relation with plasmon-assisted catalysis, which could open a new and exciting pathway for novel research.

Acknowledgements

The journey though the black seas of doubt and inexperience trying to reach the unexplored lands of unknown scientific wisdom has been an enriching experience, both on a scientific and on a personal level. Reaching the shores of these new lands of knowledge wouldn't have been possible without the help of Ben Truscott, Julian Anaya and Sara Nuñez, who were much needed lighthouses during the many difficult moments throughout this trip.

The crew that sailed with me on this voyage (James Thomas, Zamir Othman, Alex Croot, Petros Androvitsaneas, Sara Halliwell and others) were a source of experience and encouragement as well as camaraderie, that helped us all to reach the promised land. Not, of course, without a few bruises due to the rough seas.

I would like to thank Neil Fox for enrolling me on this vessel with the promise of unexpected adventures and mythical treasures. The journey didn't disappoint in the least.

Finally, I would like to show my thanks to Cristina, who unknowingly boarded this ship with me, and stayed there despite the her permanent doubts about the sanity of the whole enterprise.

Godspeed to all of you.

Author's declaration

I declare that the work in this dissertation was carried out in accordance with the requirements of the University's Regulations and Code of Practice for Research Degree Programmes and that it has not been submitted for any other academic award. Except where indicated by specific reference in the text, the work is the candidate's own work. Work done in collaboration with, or with the assistance of, others, is indicated as such. Any views expressed in the dissertation are those of the author.

SIGNED: DATE:

Contents

I do not pretend to start with precise questions. I do not think you can start with anything precise. You have to achieve such precision as you can, as you go along.

-Bertrand Russell

Introduction

1

This chapter begins with the definition of key surface science concepts that are relevant to this work. Then an explanation of the physics of electron emission is provided, with an emphasis on thermionic emission, followed by a summary of the main properties of diamond. After that, the field of plasmonics is briefly introduced. Subsequently, the last section of this chapter identifies the aims and motivations for this thesis.

1.1 Surface concepts

1.1.1 Work function

The work function (WF) of a surface is a property that accounts for the minimum energy that is necessary to remove an electron from that surface and place it at an infinitely large distance from the surface[1]. Another way of visualising the concept of WF is examining the potential experienced by an electron at a surface-vacuum interface. The electrons in the near surface of a bulk material experience a periodic potential caused by the positively charged atomic nuclei, but as they approach the surface they encounter a surface potential barrier that is responsible for keeping electrons from escaping the solid. This surface potential barrier is the WF (see Fig.1).

The expression for the WF, derived by Lang & Kohn [2], is:

$$\phi = \Delta\phi - \bar{\mu} \qquad (1.1)$$

where ϕ is the WF, $\Delta\phi$ is the change in electrostatic potential across the surface dipole layer created by the spillage of electrons at the surface, μ is the electrochemical potential and $\bar{\mu}$ is the chemical potential. Additionally:

$$\bar{\mu} = \mu - \phi(-\infty) \qquad (1.2)$$

where $\phi(-\infty)$ the potential of an electron deep in the bulk or the mean interior potential (see Fig.1).

The concept of WF is key for the present work and is examined more thoroughly in Chapter 5.

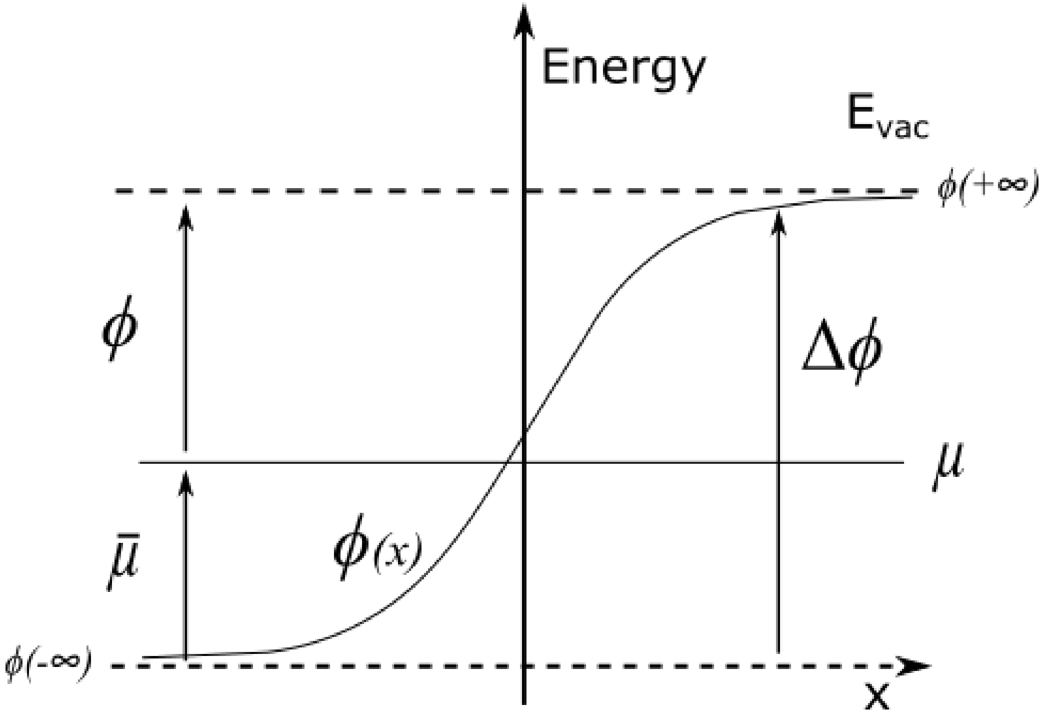

Figure 1: Plot of the electron potential on the interface between a metal and vacuum. The left side of the plot represents the potential of an electron in the bulk material ø(-∞) while the right side represents the potential of an electron in vacuum ø(+∞). μ is the electrochemical potential, $\bar{\mu}$ is the chemical potential and ø is the WF.

1.1.2 Electron affinity

Traditionally, electron affinity (EA) is known in the field of chemistry as the amount of energy released or spent when an electron is added to a neutral atom or molecule in a gaseous state to form a negative ion[3].

$$X + e^{-} \rightarrow X^{-} + E_{EA} \qquad (1.3)$$

However, in both surface and solid state physics, EA is the energy necessary to move an electron from the edge of the conduction band at the surface of a solid to the vacuum, and is represented as χ (see Fig.2)[4].

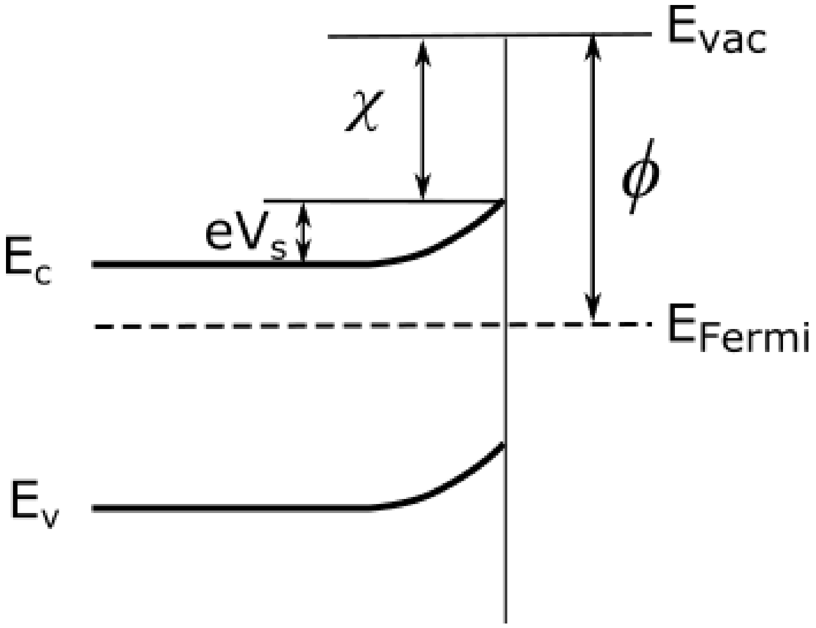

Figure 2: Schematic band diagram of a semiconductor surface. ϕ is the WF, χ is the EA, eVs is the band bending, E_F the Fermi level, E_C the conduction band minimum and E_V the valence band minimum.

This concept is related to the WF by the following expression:

$$\phi = \chi + eV_s + (E_c - E_F) \qquad (1.4)$$

where ϕ is the WF, eV_s is the band bending and (E_C - E_F) denotes the difference between the Fermi level and the conduction band minimum. Similarly to the WF, the EA is also greatly affected by surface states.

In semiconductors, the EA value can be made negative *via* surface modification. This has the effect that the vacuum potential energy level lies below the conduction band minimum at the surface, so there is a much reduced barrier for the emission of the electrons into the vacuum of thermalised electrons from the conduction band minimum[5].

1.2 Electron emission

The emission of electrons from the surface of a material can be triggered by a number of physical mechanisms. These mechanisms all have in common the fact that they need to supply energy to the electrons residing inside the material to surmount a surface potential barrier. The electrons on the near surface of any solid experience a periodic potential generated by the atomic nuclei, but as they approach the surface they encounter a potential barrier. This barrier is responsible for keeping the electrons from escaping the solid (see Fig.1). Therefore, if an electron is to leave the solid and be emitted, it must overcome this surface potential previously defined above as WF.

There are four main mechanisms to overcome this surface potential: photoelectric effect, secondary electron emission, field emission and thermionic emission.

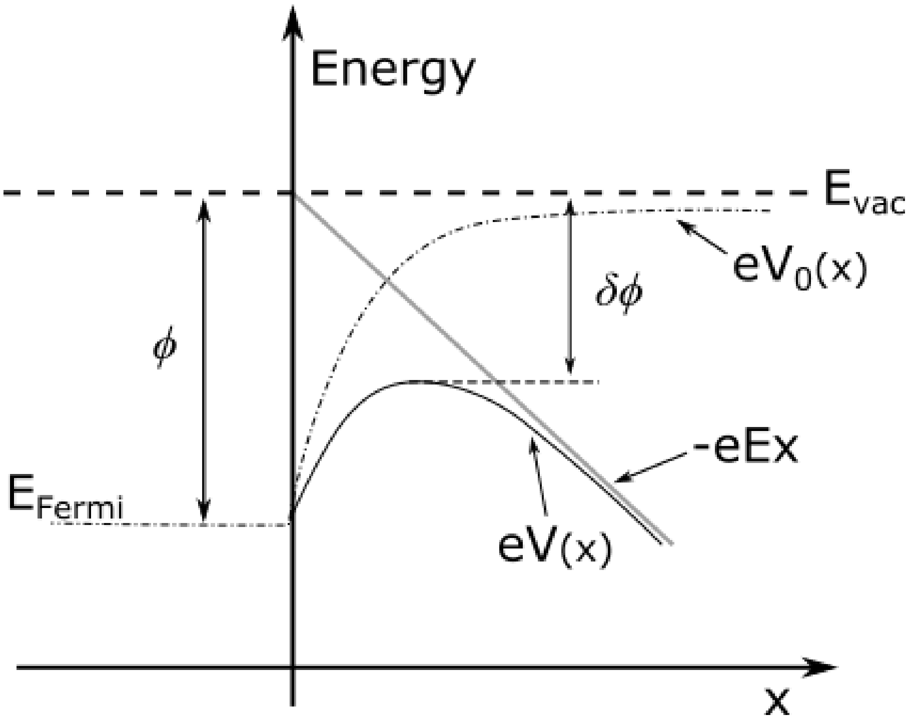

Figure 3: Surface potential energy near a metal-vacuum interface. The dashed curved line represents the surface potential barrier of the surface ($eV_0(x)$), while the solid curved line represents the same but with an electric field of strength E applied. ϕ is the WF, $\delta\phi$ represents the WF lowering due to the applied electric field, E_{vac} is the energy of the vacuum level and E_{Fermi} is the Fermi level. The horizontal axis represents the distance from the surface whose zero is on the intersection with the vertical axis.

In the case of field emission[6], a strong electric field is applied to the surface of the solid, which lowers the surface potential barrier to such an extent that electrons can surmount the barrier *via* quantum tunnelling and be emitted without the supply of additional energy. Conversely, in the other three cases (photoelectric effect[7], secondary electron emission[8] and thermionic emission), electrons are supplied with additional energy so that they can overcome the existing surface potential barrier (see Fig.3). In the case of photoelectric effect this energy is provided by incident photons while in secondary electron emission the energy is provided by incident primary electrons or ions[9].

1.2.1 Thermionic emission

Thermionic emission (TE) is the phenomenon by which electrons are thermally induced to be emitted from the surface of a material. If the temperature of a certain material increases, so does the energy of its electrons and if this energy is higher than the surface potential barrier or WF, electrons will be emitted.

The research of TE phenomena started in the 19th century, when Becquerel, and later on Guthrie[10], reported that in the vicinity of incandescent objects there was evidence of electrical charge being generated. Their reports were followed by others developed by Geitel & Elster in the 1880s where the charge collected by a metallic plate in the vicinity of an incandescent object was examined under various conditions[11]. At the same time, TE was observed by Edison which led the TE phenomenon to be labelled by Preece[12] as the Edison effect.

Later, with the discovery of the electron by Thomson[13] it was possible for Richardson to elaborate a more detailed theory of TE that led to the development of the following equation, known as the Richardson-Dushman equation[14] (RDE):

$$J(T,\phi) = AT^2 e^{-\frac{\phi}{kT}} \qquad (1.5)$$

where J is the TE current per square meter in Amperes, A is the Richardson constant, ϕ is the WF of the emitting surface, T is the temperature of the surface and k is the Boltzmann constant.

The equation above describes pure TE. There are, however, also hybrid TE processes. One of these is photon-enhanced TE[15], which uses thermal energy to thermionically emit photo excited electrons. Conversely, we have field-enhanced TE[1], which uses an electric field to lower the surface potential barrier causing an increase in TE current.

1.2.2 Applications of thermionic emission: thermionic energy converters

The first application of TE was devised by Edison, who patented a voltage regulating device[16]. A few years later Fleming patented the vacuum tube or diode which was used to rectify an alternating current[17]. This component quickly became an essential part of most of the electronic devices in the first part of the 20th century, finding applications in radio, television, analogue computers and radars.

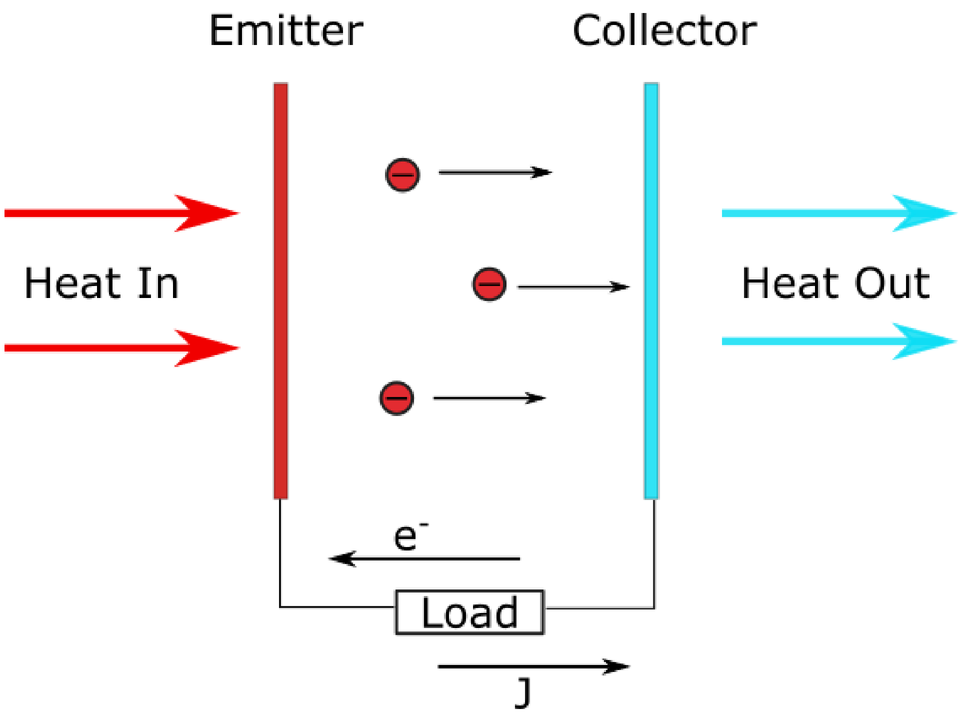

Figure 4: TEC diagram consisting of two parallel plates electrically connected through an electrical load. Heat is transferred into the emitter to increase its temperature and cause TE.

Thermionic energy converters (TEC) are another important application of TE. TEC directly convert heat into electricity by making use of the TE to move electronic charge from a hot electrode to a cooled electrode where kinetic energy is dissipated and potential energy carried by the charge is passed through an electrical load to generate power (see Fig.4).

The simplest configuration of a TEC is two parallel plates separated by a small distance that are electrically connected to a load. One of the plates is then heated to the point where it starts emitting electrons *via* TE while the other plate is kept cool and harvests the electrons emitted by the opposite plate. The former plate is called the ‘emitter’ and the latter ‘collector’.

The surface of the emitter should have a WF as low as possible to maximise emission current. For that purpose, traditionally TEC are constructed in an enclosed chamber filled with a low pressure of caesium gas. Caesium has the property of lowering the WF of metals when it is bonded to its surface[18]. However, its bond to the surface is weak and it evaporates easily at high temperatures.

Therefore, the presence of caesium gas generates a dynamic equilibrium between evaporation and adsorption that ensures that the caesium coverage of the emitter is maximised.

The TEC has no moving parts and it is fairly simple to fabricate, which increases the reliability of the device. This led in the 1980s to the development of TEC for aerospace applications generally using radioactive sources as a heat source[19,20]. Additionally, some researchers have also tried to develop TEC for domestic use[21] using gas cogeneration techniques achieving efficiencies of 13%[22,23]. However, TEC technology never made it to the consumer market and has been relegated to niche applications.

1.2.3 Thermionic emission from H terminated diamond

Diamond can work as a thermionic emitter but TE from diamond was found to be dependent on its surface termination. More specifically, hydrogen termination was explored. The hydrogen termination lowers the WF of the surface and causes it to have a negative electron affinity (NEA) that enables TE[24,25] as mentioned earlier in this chapter. NEA occurs when the WF of a surface has such a value that the vacuum energy level lies below the conduction band minimum so that it is easy for electrons in the conduction band to escape to vacuum[26].

Field-assisted TE has been reported for nitrogen doped diamond films with a hydrogen termination[27]. In several of these studies the fitting of the RDE to the TE data produced values for the WF of diamond of ≈ 1.5 eV [28], 1.9 eV [29] and 1.44 eV [30].

Boron-doped diamond without hydrogen termination was tested for TE[31] at temperatures above 1000 °C and the results showed that there is indeed TE. But the emission is of just a few nanoamps, which is well below the reported values for other dopants, and the work function provided by the RDE fitting was 4.43 eV.

Phosphorus-doped hydrogen terminated diamond has been found to exhibit thermionic emission with a WF of 1.18 eV [30]. A similar result is found for sulphur doped hydrogen terminated diamond[32], in this case with a WF of 2.5 eV.

The role in TE of the interface between the diamond and the substrate used to support it was also studied by Koeck *et al*[33]. It was revealed that the substrate material has a substantial influence on the maximum current. This is, of course, under the assumption that the charge is supplied to the surface through the substrate-diamond interface.

Summarising, nitrogen-doped diamond with hydrogen termination seems to have the best TE generating higher currents than other alternatives. However, the desorption of hydrogen at high temperatures hampers the viability of the use of diamond as a thermionic device. This is because the desorption of hydrogen leads to the loss of NEA and the decay of TE current in a short period of time[34]. This matter will be discussed in depth in Chapter 4.

1.3 Diamond

1.3.1 General properties

Carbon occurs in nature either combined with other elements, making some compounds that are essential to life, or existing in a purer form like graphite or diamond. In its ground state, carbon has six electrons (C: $1s^2 2s^2 2p^2$), of which two are core electrons and four are valence electrons distributed among *s* and *p* orbitals. When carbon bonds to carbon, these valence electrons form either 3-fold or four-fold coordinated structures. On the graphite case, carbon atoms have an sp^2 hybridisation where the atoms are covalently bonded to the three nearest neighbours laying on the same plane forming a honeycomb network, while the remaining electron forms a *p* orbital perpendicular to this plane. This fourth electron is weakly bonded and makes graphite electrically conductive.

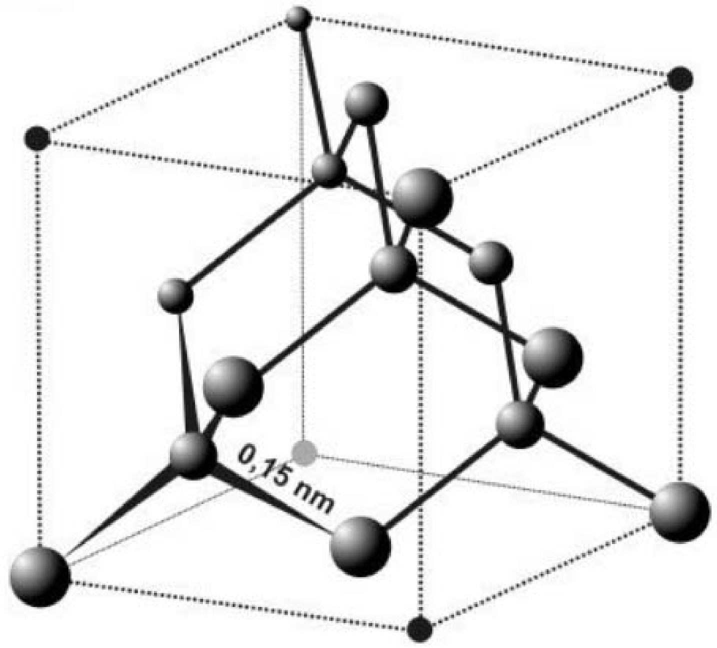

Figure 5: Diamond atomic structure.

Conversely, when carbon has an sp^3 hybridisation, the four electrons are bonded to the four nearest carbon atoms forming a σ covalent bonded structure which is known as diamond (see Fig.5). This structure is a face centred cubic lattice (FCC) with a unit cell length of a_0 = 3.57 Å at room temperature[5] containing eight atoms and a bond length of 1.54 Å. This gives diamond a mass density of 3516 kg/m^3 and an atomic number density of 1.76×10^{23} cm^{-3}.

This high density is responsible for the outstanding properties of diamond. Diamond is one of the hardest known materials with a value of 10 on the Mohs hardness scale. The densely packed structure of diamond creates an ideal medium for the propagation of phonons and that is the reason for diamond's extremely high thermal conductivity, that can be as high as 2000 W/mK at room temperature[35].

1.3.2 Diamond doping

Diamond is a wide-bandgap semiconductor with a bandgap of 5.47 eV [36]. Similarly to other semiconductors, the electrical properties of diamond can be modified *via* doping of the lattice with impurities.

It is possible to create p-type diamond by doping it with boron, which replaces one of the carbon atoms on the lattice. Boron is a substitutional dopant that has three valence electrons and therefore it acts as an acceptor. The activation energy for the boron impurity is 0.37 eV above the valence band of the diamond which makes it a shallow acceptor[37]. Moreover, boron incorporates very well into the diamond lattice during the growth of diamond with chemical vapour deposition methods. This allows for high atomic concentrations (10^{10}- 10^{21} at/cm^3) allowing boron doped diamond to have metallic conductivities of the order of 5-100 mΩ [38].

Regarding the n-type doping of diamond, there are several elements that can incorporate into diamond and act as a donor impurity. But so far the most successful candidate has been nitrogen, which incorporates substitutionally on diamond with ease. However, nitrogen is a deep donor that lies 1.7 eV below the conduction band. This means that at room temperature there are no impurities ionised and the nitrogen-doped diamond is an insulator. It is then necessary to increase the temperature of the doped diamond up to around 300 °C to start ionising nitrogen impurities and increase electrical conductivity. This means that the use of nitrogen doped diamond in electronic devices, like p-n junctions, is not feasible.

Apart from nitrogen, there are other elements that could be used to obtain n-type diamond such as phosphorus or sulphur. But their activation energies, 0.6 eV for phosphorus[39] and 0.5-0.75 eV for sulphur[40] are still too high for the material to be usable at room temperature. Therefore, more research is still needed on this topic, both experimentally and theoretically, to produce a reliable n-type diamond.

1.3.3 Diamond surface

The electronic properties of a surface are largely determined by its atomic structure. Normally, un-terminated surfaces have a high energy because of the presence of dangling bonds. In order to stabilise the surface, it reconstructs by forming new bonds or it is passivated with adsorbates. In the case of diamond and its <100> surface, the key interest for this thesis, each carbon atom has two dangling bonds. This leads to a (2×1) reconstruction[41] that was experimentally confirmed a couple decades later by Bobrov *et al*[42]. Moreover, if the diamond surface is terminated by hydrogen, the surface reconstructs with a C(100)-(2×1):H structure[43] as shown in Fig.6.

The hydrogen termination of the diamond surface confers on it some interesting properties, including that the EA of the surface becomes negative by shifting the vacuum level below the conduction band minimum of the diamond. Therefore, it is a property with important implications for applications like electron emission[44] or renewable energy[21].

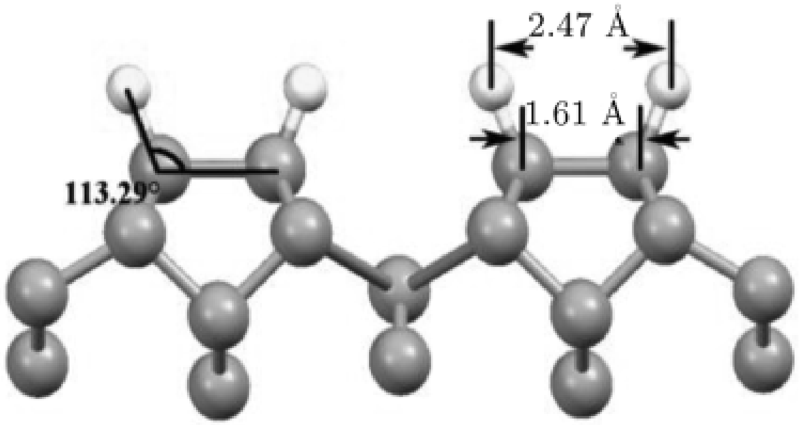

Figure 6: Surface atomic structure of hydrogen terminated diamond on the <100> orientation: C(100)-(2×1):H. Grey spheres are carbon atoms and white spheres are hydrogen atoms.

The reduction of the EA to achieve an NEA is strongly linked to the reduction of the WF (see sect.1.1.2) and it is caused by the formation of a surface dipole[18]. When hydrogen bonds to the carbon atoms on the surface, it loses its electron to the carbon. This causes the hydrogen to be positively charged while the carbon is negatively charged. Thus, they form a dipole pointing inwards into the surface. This dipole lowers the surface potential barrier of diamond and consequently reduces its WF and EA[45].

Another property of hydrogen terminated diamond is the fact that the surface becomes insulating while under vacuum conditions. Conversely, if the surface is exposed to air, p-type conductivity is detected. This change in the surface behaviour was shown to be caused by the presence of adsorbates and gave rise to the development of the 'transfer doping model'[46].

1.4 Plasmonics: interaction between light and nanoparticles

The illumination of a metallic nanoparticle with light causes the conduction electrons of the metal to interact with the incident electromagnetic radiation. For the case of extended metal surfaces, this interaction drives a propagating collective oscillation of electrons known as surface plasmon polariton[47]. In the case of metallic nanoparticles, these electron oscillations are confined within the extent of the nanoparticle, being unable to propagate outside the boundaries of the particle and in turn are termed localised surface plasmons (LSP)[48,49]. These LSP, also referred to as "plasmonic antenna effect" by some authors[50], are interwoven with other effects that are present when exciting nanoparticles with light, including electric field enhancement and hot carrier generation are the two most important of these effects.

The confinement of the electron oscillation in such a limited volume creates a resonance that leads to the appearance of highly localised intense electric fields called ‘nodes’ or ‘hot spots’[51]. These nodes have been mapped *via* electron energy loss spectroscopy (EELS)[52,53], scanning near-field optical microscopy (SNOM)[54] and other techniques[55] for a range of different morphologies and materials. Moreover, this local-field enhancement effect has been applied to the development of surface enhanced Raman spectroscopy[56]. This was possible thanks to the fact that intense fields greatly amplify the Raman signal to the point that single molecules can be detected[57,58].

The excitation of LSP on nanoparticles significantly increases the interaction of the latter with incoming photons which might excite electrons out of their primitive energy level. The newly created electron-hole pairs are referred to as ‘hot carriers’[59]. These have high energies, above the Fermi level, and decay through electron-electron and electron-phonon interactions on a timescale of a few nanoseconds[60,61]. Photocatalysis[62–65], localised heating[66,67] or photovoltaic devices[68,69] are a few examples of applications of the hot carriers. However, recently a new effect associated with LSP apart from the two mentioned above has been reported. This effect is termed plasmoelectric potential and is discussed in detail in Chapter 5.

1.5 Motivation and outline of this thesis

The overarching objective of this thesis is to study the modification of the WF for energy applications. But the thesis revolves around TE from diamond, which, as other TE materials, has a strong dependence on the property of WF. In this thesis we examine two methods of modifying the WF of a material. One is the traditional method of chemisorbed adsorbates while the other is a recently reported phenomenon called plasmo-electric potential (PEP). An outline of the content of this thesis is detailed below.

Chapter 2 introduces the theory behind the experimental methods and analysis techniques used in this thesis.

Chapter 3 is the first experimental chapter and reports on the development of a plasmonic heating system used to test some of the diamond samples used in Chapter 4.

Chapter 4 describes an alternative model for TE that accounts for the effect of hydrogen desorption on the TE current and allows the extraction of parameters like WF and hydrogen energy of desorption from TE data.

Chapter 5 examines the possibility of using PEP to lower the WF of a surface for TE applications. This chapter is exploratory and studies the nature of the PEP in depth to gauge the possibilities of its applications.

Chapter 6 summarises the results of the previous chapters and proposes several possibilities for future work.

Acronyms

WF: Work Function

EA: Electron Affinity

TE: Thermionic Emission

RDE: Richardson-Dushman Equation

TEC: Thermionic Energy Converters

NEA: Negative Electron Affinity

FCC : Face Centred Cubic

LSP: Localised Surface Plasmons

EELS: Electron Energy Loss Spectroscopy

SNOM: Scanning Near-Field Optical Microscopy

PEP: Plasmo-Electric Potential

List of figures

References

1. Hölzl, J., Schulte, F. K. & Wagner, H. *Solid Surface Physics*. **85,** (Springer-Verlag, 1979).

2. Lang, N. D. & Kohn, W. Theory of Metal Surfaces: Work Function. *Physical Review B* **3,** 1215–1223 (1971).

3. McNaught, A. D. & Wilkinson, A. *IUPAC Compendium of Chemical Terminology*. *IUPAC Compendium of Chemical Terminology* (IUPAC, 2014). doi:10.1351/goldbook.I03352

4. Oura, K., Katayama, M., Zotov, A. V., Lifshits, V. G. & Saranin, A. A. *Surface Science*. (Springer Berlin Heidelberg, 2003). doi:10.1007/978-3-662-05179-5

5. Ibach, H. *Physics of Surfaces and Interfaces*. (Springer Berlin Heidelberg, 2006). doi:10.1007/3-540-34710-0

6. Fowler, R. H. & Nordheim, L. Electron Emission in Intense Electric Fields. *Proceedings of the Royal Society A: Mathematical, Physical and Engineering Sciences* **119,** 173–181 (1928).

7. Millikan, R. A. A Direct Photoelectric Determination of Planck's 'h'. *Physical Review* **7,** 355–388 (1916).

8. Bruining, H. & De Boer, J. H. Secondary electron emission. *Physica* **5,** 17–30 (1938).

9. van Elsbergen, V., Bachmann, P. K. & Juestel, T. 16.3: Ion-Induced Secondary Electron Emission: A Comparative Study. *SID Symposium Digest of Technical Papers* **31,** 220 (2000).

10. Guthrie, F. On a New Relation between Heat and Electricity. *Proceedings of the Royal Society of London* **21,** 168–169 (1872).

11. Geitel, H. . & Elster, J. Ueber die Electricitätserregung beim Contact verdünnter Gase mit galvanisch glühenden Drähten. *Annalen der Physik und Chemie* **37,** 315–329 (1889).

12. Preece, W. H. On a Peculiar Behaviour of Glow-Lamps When Raised to High Incandescence. *Proceedings of the Royal Society of London* **38,** 219–230 (1884).

13. Thomson, J. J. Cathode rays. *Philosophical Magazine* **44,** 293 (1897).

14. Richardson, O. W. Thermionic phenomena and the laws which govern them. *Nobel Lecture* (1929).

15. Schwede, J. W. *et al.* Photon-enhanced thermionic emission for solar concentrator systems. *Nature materials* **9,** 762–7 (2010).

16. Edison, T. A. Electrical Indicator. 10–21 (1884).

17. Fleming, J. A. Improvements in Instruments for Detecting and Measuring Alternating Electric Currents. (1904).

18. Taylor, J. B. & Langmuir, I. The Evaporation of Atoms, Ions and Electrons from Caesium Films on Tungsten. *Physical Review* **44,** 423–458 (1933).

19. Gryaznov, G. M. *et al.* Thermoemission reactor-converters for nuclear power units in outer space. *Soviet Atomic Energy* **66,** 414–418 (1989).

20. Mills, J. C. & Dahlberg, R. C. Thermionic systems for DOD missions. in *AIP Conference Proceedings* **217,** 1088–1092 (AIP, 1991).

21. Fraser, D. A., Tanner, P. G. & Irving, A. D. Developments in thermionic energy converters. *IEE Proceedings - Science, Measurement and Technology* **152,** 1–6 (2005).

22. Veltkamp, W. B., van Kemenade, H. P. & Sampers, W. F. J. Combustion Heated Thermionic Systems. in *SAE Technical Paper* (SAE International, 1992). doi:10.4271/929355

23. van Kemenade, E. & Veltkamp, W. Design of a thermionic converter for a domestic heating system. in *Intersociety Energy Conversion Engineering Conference* (American Institute of Aeronautics and Astronautics, 1994). doi:10.2514/6.1994-4209

24. van der Weide, J. *et al.* Negative-electron-affinity effects on the diamond (100) surface. *Physical Review B* **50,** 5803–5806 (1994).

25. Takeuchi, D., Ri, S.-G., Kato, H., Nebel, C. E. & Yamasaki, S. Negative electron affinity on hydrogen terminated diamond. *physica status solidi (a)* **202,** 2098–2103 (2005).

26. Hatta, A. *et al.* Electron emitter device of NEA diamond thin film. *Applied Surface Science* **117–118,** 592–596 (1997).

27. Koeck, F. a. M., Garguilo, J. M. & Nemanich, R. J. On the thermionic emission from nitrogen-doped diamond films with respect to energy conversion. *Diamond and Related Materials* **13,** 2052–2055 (2004).

28. Koeck, F. A. M. & Nemanich, R. J. Low temperature onset for thermionic emitters based on nitrogen incorporated UNCD films. *Diamond and Related Materials* **18,** 232–234 (2009).

29. Suzuki, M., Ono, T., Sakuma, N. & Sakai, T. Low-temperature thermionic emission from nitrogen-doped nanocrystalline diamond films on n-type Si grown by MPCVD. *Diamond and Related Materials* **18,** 1274–1277 (2009).

30. Koeck, F. a. M., Nemanich, R. J., Balasubramaniam, Y., Haenen, K. & Sharp, J. Enhanced thermionic energy conversion and thermionic emission from doped diamond films through methane exposure. *Diamond and Related Materials* **20,** 1229–1233 (2011).

31. Paxton, W. F. *et al.* Thermionic emission characterization of boron-doped microcrystalline diamond films at elevated temperatures. *physica status solidi (a)* **209,** 1993–1995 (2012).

32. Koeck, F. a. M. & Nemanich, R. J. Sulfur doped nanocrystalline diamond films as field enhancement based thermionic emitters and their role in energy conversion. *Diamond and Related Materials* **14,** 2051–2054 (2005).

33. Koeck, F. a. M. & Nemanich, R. J. Substrate-diamond interface considerations for enhanced thermionic electron emission from nitrogen doped diamond films. *Journal of Applied Physics* **112,** 113707 (2012).

34. Paxton, W. F., Howell, M., Kang, W. P. & Davidson, J. L. Influence of hydrogen on the thermionic electron emission from nitrogen-incorporated polycrystalline diamond films. *Journal of Vacuum Science & Technology B, Nanotechnology and Microelectronics: Materials, Processing, Measurement, and Phenomena* **30,** 21202 (2012).

35. Barman, S. & Srivastava, G. P. Temperature dependence of the thermal conductivity of different forms of diamond. *Journal of Applied Physics* **101,** 123507 (2007).

36. Koizumi, S., Nebel, C. & Nesladek, M. *Physics and Applications of CVD Diamond*. (Wiley-VCH Verlag GmbH & Co. KGaA, 2008). doi:10.1002/9783527623174

37. Collins, a. T. The Optical and Electronic Properties of Semiconducting Diamond. *Philosophical Transactions of the Royal Society A: Mathematical, Physical and Engineering Sciences* **342,** 233–244 (1993).

38. Fryda, M. *et al.* Fabrication and application of Diachem® electrodes. *Diamond and Related Materials* **12,** 1950–1956 (2003).

39. Koizumi, S., Kamo, M., Sato, Y., Ozaki, H. & Inuzuka, T. Growth and characterization of phosphorous doped {111} homoepitaxial diamond thin films. *Applied Physics Letters* **71,** 1065–1067 (1997).

40. Nakazawa, K. *et al.* Cathodoluminescence and Hall-effect measurements in sulfur-doped chemical-vapor-deposited diamond. *Applied Physics Letters* **82,** 2074–2076 (2003).

41. Verwoerd, W. S. A study of the dimer bond on the reconstructed (100) surfaces of diamond and silicon. *Surface Science* **103,** 404–415 (1981).

42. Bobrov, K., Mayne, a. J., Hoffman, a. & Dujardin, G. Atomic-scale desorption of hydrogen from hydrogenated diamond surfaces using the STM. *Surface Science* **528,** 138–143 (2003).

43. Bobrov, K. *et al.* Atomic-scale visualization and surface electronic structure of the hydrogenated diamond C(100)-(2x1):H surface. *Physical Review B* **68,** 195416 (2003).

44. Cui, J. B., Ristein, J. & Ley, L. Low-threshold electron emission from diamond. *Physical Review B* **60,** 135–142 (1999).

45. O'Donnell, K. M. *et al.* Diamond Surfaces with Air-Stable Negative Electron Affinity and Giant Electron Yield Enhancement. *Advanced Functional Materials* n/a-n/a (2013). doi:10.1002/adfm.201301424

46. Ley, L., Ristein, J., Meier, F., Riedel, M. & Strobel, P. Surface conductivity of the diamond: A novel transfer doping mechanism. *Physica B: Condensed Matter* **376–377,** 262–267 (2006).

47. Barnes, W. L. Surface plasmon–polariton length scales: a route to sub-wavelength optics. *Journal of Optics A: Pure and Applied Optics* **8,** S87–S93 (2006).

48. Stockman, M. I. Nanoplasmonics: The physics behind the applications. *Physics Today* **64,** 39–44 (2011).

49. Maier, S. A. *Plasmonics: Fundamentals and Applications*. **1,** (Springer US, 2007).

50. Gao, S., Ueno, K. & Misawa, H. Plasmonic Antenna Effects on Photochemical Reactions. *Accounts of Chemical Research* **44,** 251–260 (2011).

51. Stockman, M. I., Pandey, L. N. & George, T. F. Inhomogeneous localization of polar eigenmodes in fractals. *Physical Review B* **53,** 2183–2186 (1996).

52. Nelayah, J. *et al.* Mapping surface plasmons on a single metallic nanoparticle. *Nature Physics* **3,** 348–353 (2007).

53. Mayer, M. *et al.* Controlled Living Nanowire Growth: Precise Control over the Morphology and Optical Properties of AgAuAg Bimetallic Nanowires. *Nano Letters* **15,** 5427–5437 (2015).

54. Alonso-González, P. *et al.* Resolving the electromagnetic mechanism of surface-enhanced light scattering at single hot spots. *Nature Communications* **3,** 684 (2012).

55. Viarbitskaya, S. *et al.* Tailoring and imaging the plasmonic local density of states in crystalline nanoprisms. *Nature Materials* **12,** 426–432 (2013).

56. Fleischmann, M., Hendra, P. J. & McQuillan, A. J. Raman spectra of pyridine adsorbed at a

silver electrode. *Chemical Physics Letters* **26,** 163–166 (1974).

57. Sigle, D. O. *et al.* Observing Single Molecules Complexing with Cucurbit[7]uril through Nanogap Surface-Enhanced Raman Spectroscopy. *The Journal of Physical Chemistry Letters* **7,** 704–710 (2016).

58. Kneipp, K. *et al.* Single Molecule Detection Using Surface-Enhanced Raman Scattering (SERS). *Physical Review Letters* **78,** 1667–1670 (1997).

59. Brongersma, M. L., Halas, N. J. & Nordlander, P. Plasmon-induced hot carrier science and technology. *Nature Nanotechnology* **10,** 25–34 (2015).

60. Brown, A. M., Sundararaman, R., Narang, P., Goddard, W. A. & Atwater, H. A. Nonradiative Plasmon Decay and Hot Carrier Dynamics: Effects of Phonons, Surfaces, and Geometry. *ACS Nano* **10,** 957–966 (2016).

61. Méjard, R. *et al.* Energy-Resolved Hot-Carrier Relaxation Dynamics in Monocrystalline Plasmonic Nanoantennas. *ACS Photonics* **3,** 1482–1488 (2016).

62. Kamat, P. V. Photophysical, photochemical and photocatalytic aspects of metal nanoparticles. *Journal of Physical Chemistry B* **106,** 7729–7744 (2002).

63. Zhou, L. *et al.* Aluminum Nanocrystals as a Plasmonic Photocatalyst for Hydrogen Dissociation. *Nano Letters* **16,** 1478–1484 (2016).

64. Swearer, D. F. *et al.* Heterometallic antenna-reactor complexes for photocatalysis. *Proceedings of the National Academy of Sciences of the United States of America* **113,** 8916–20 (2016).

65. Robatjazi, H., Bahauddin, S. M., Doiron, C. & Thomann, I. Direct Plasmon-Driven Photoelectrocatalysis. *Nano Letters* **15,** 6155–6161 (2015).

66. Adleman, J. R., Boyd, D. A., Goodwin, D. G. & Psaltis, D. Heterogenous catalysis mediated by plasmon heating. *Nano Letters* **9,** 4417–4423 (2009).

67. Hoheisel, W., Jungmann, K., Vollmer, M., Weidenauer, R. & Träger, F. Desorption stimulated by laser-induced surface-plasmon excitation. *Physical Review Letters* **60,** 1649–1652 (1988).

68. Atar, F. B. *et al.* Plasmonically enhanced hot electron based photovoltaic device. *Optics Express* **21,** 7196 (2013).

69. Clavero, C. Plasmon-induced hot-electron generation at nanoparticle/metal-oxide interfaces for photovoltaic and photocatalytic devices. *Nature Photonics* **8,** 95–103 (2014).

A tidy laboratory means a lazy chemist.

-Jöns Jacob Berzelius

Experimental Methods 2

This chapter begins with a detailed description of the instrument used to perform heating and thermionic emission measurements that was designed and built during this PhD. In the following sections, there is an explanation of the main characterisation techniques used in this work with an emphasis on scanning probe microscopy techniques. Lastly, there is a general explanation of the microwave plasma reactors used to modify the diamond surface and a section on sample preparation.

2.1 Thermionic Energy Converter simulator

The thermionic energy converter simulator (TECsim) is a test rig used for controlled laser heating of different materials in a vacuum environment while measuring their temperature and thermionic emission (TE) in real time. The TECsim is also equipped with a residual gas analyser (RGA) so that it is possible to monitor in real time the concentration of different gases inside the testing environment.

The main advantages of the TECsim are the fast heating rate due to its laser heating system, low thermal inertia, very accurate temperature control (temperature is maintained within a $\pm$ 0.1 K interval from the temperature setpoint), programmable temperature ramps and very low electrical noise due to a double thermo-electrical decoupling. The distance between the sample and the collector of electrons can also be remotely controlled before and during the experiment with a motorised mechanism.

The heating and thermionic tests described in this thesis were all carried out using the TECsim. This system was designed to provide a testing platform for both the plasmonic heating structures described in Chapter 3 and the different thermionic materials described in Chapter 4. Owing to its specific characteristics the system can also be used to perform temperature programmed desorption[1] experiments.

This system operates in high vacuum (HV) conditions. This is necessary as in thermionic emission the mean free path of electrons needs to be long enough to allow them to travel from the sample cathode emitter to the collector electrode, which are separated by a gap of $\sim 200\ \mu\text{m}$. Otherwise, collisions with gas particles would reduce the mean free path making measurements impossible.

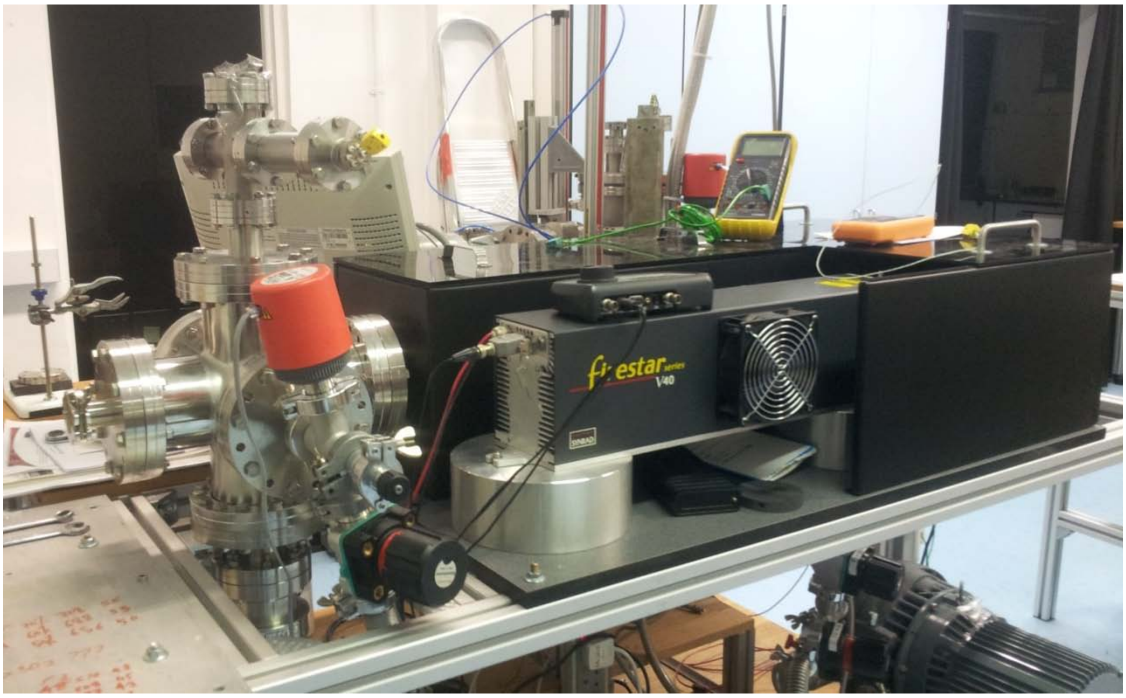

Figure 1: TECsim vacuum chamber and CO_2 laser source.

2.1.1 Chamber and vacuum system

The sample stage and collector assembly of the TECsim is enclosed in a stainless steel vacuum chamber. The chamber has a 6-way cross shape and an approximate volume of 7 - 8 L. The chamber is pumped by a turbomolecular pump (Edwards, Edwards EXT 75DX CF63) in series with a scroll pump (Leybold, Scrollvac SC 30D) which was also used to establish rough vacuum.

The pressure is measured with a Penning gauge for pressures above 1×10^{-2} mTorr and with a Pirani gauge for pressures below that. The base pressure for the system is P≈1×10^{-7} mTorr.

In order to vent the chamber, air was admitted through a needle valve. Several borosilicate viewports are installed on the chamber in order to have optical access to the sample for temperature measurement purposes using optical pyrometry. Ceramic insulated feedthroughs are used to feed all the electric signals in and out of the chamber.

2.1.2 Sample stage and collector assemblies

The TECsim, depicted in Fig.8, has been designed to support a standard sample size of a 10 × 10 mm square. But other sizes are also possible with a simple modification of the set-up. The sample sits on top of a quartz plate to minimise thermal heat conduction losses and to achieve electrical insulation from the chamber. The sample is fixed in place with molybdenum (Mo) clamps attached to the quartz plate. The area of the quartz plate under the sample has been machined so that it is hollow to provide a direct optical path for the laser for heating purposes.

The quartz plate is attached onto a detachable stainless steel ring that can be easily removed from the system to facilitate sample exchange. This ring sits on a second machined quartz plate to again avoid thermal loss and achieve electrical insulation from the surroundings. These two quartz plates form a double thermo-electrical decoupling layer that is key to achieve a system with low electrical noise. Experience with similar systems showed that spurious leakage currents are a major problem on TE measurements, and so the TECsim was designed to avoid these with the double decoupling layer. Quartz was chosen as the material for the decoupler due to its excellent electrical and thermal (≈ 1.5 W m^{-1} K^{-1}) insulating properties[2]. However, the softening point of quartz is around 1050 °C, where it begins to lose mechanical stability. This limits the maximum temperature at which the TECsim can operate.

The second quartz plate sits on a square stainless steel frame connected in the corners to four stainless steel rods that make the sample stage to be suspended from the top flange of the vacuum chamber. This flange is removed and place on a special holder so that easy access to the whole sample stage attached to it is possible while in air. Electrical contact is made to the sample through the Mo clamps that are connected to an electrical connector made of copper wire *via* a tungsten (W) wire to avoid melting due to the high working temperatures of the device. A thermocouple is fixed to the first quartz plate so that the thermocouple junction is firmly pressed against the sample to ensure correct temperature measurement.

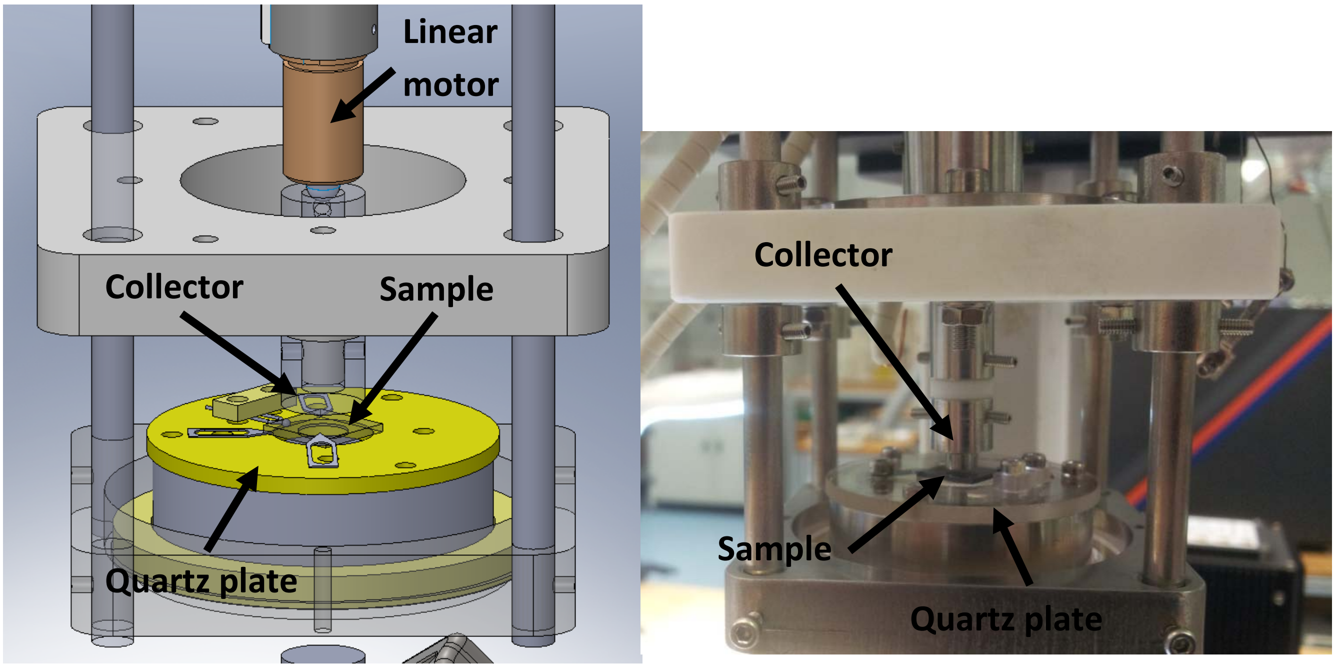

Figure 2: TECsim sample stage and collector assembly. (Left): CAD model. (Right): Final parts assembled.

On top of the sample stage sits the collector assembly. The collector electrode harvests the electrons emitted by the sample during TE experiments. The collector assembly consists of a stainless steel electrode connected to a copper connector *via* a W wire in a similar fashion to the sample clamps described previously. The collector is cylindrical and is easily interchangeable. A series of collectors with different diameters were manufactured for this project in order to be able to adapt to different sample sizes.

The collector is attached to a thermo-electrical decoupler made out of borosilicate machinable ceramic known commercially as MACOR, which is designed to be cylindrical. This MACOR decoupler has the same function as the quartz decoupler but for this case, more specific shapes were required that could only be obtained by machining. Thus, the use of MACOR allowed for precise mechanical machining despite being a ceramic insulator. This decoupler is connected to a vacuum-compatible motorised linear shift (Thorlabs.Inc, Z825BV). So in this case the decoupler has a double function: it avoids any electrical noise from reaching the collector and protects the motor from the high temperatures achieved on the collector. Temperatures on the collector can reach a few hundred degrees in the worst case while the motor's maximum working temperature is around ≈ 60 °C.

This motor controls the size of the vacuum gap between the sample emitter cathode and collector in real time both prior to and during experiments. The motor has a theoretical linear resolution of 40 nm but the actual resolution is limited by the backlash of the reduction gear box inside the motor so that the real value of the linear resolution≈isl µm. This motor is mounted on a thermo-electrical decoupling MACOR square plate that is attached to the 4 stainless steel rods suspended from the top chamber flange and positioned above the stainless steel frame of the sample stage.

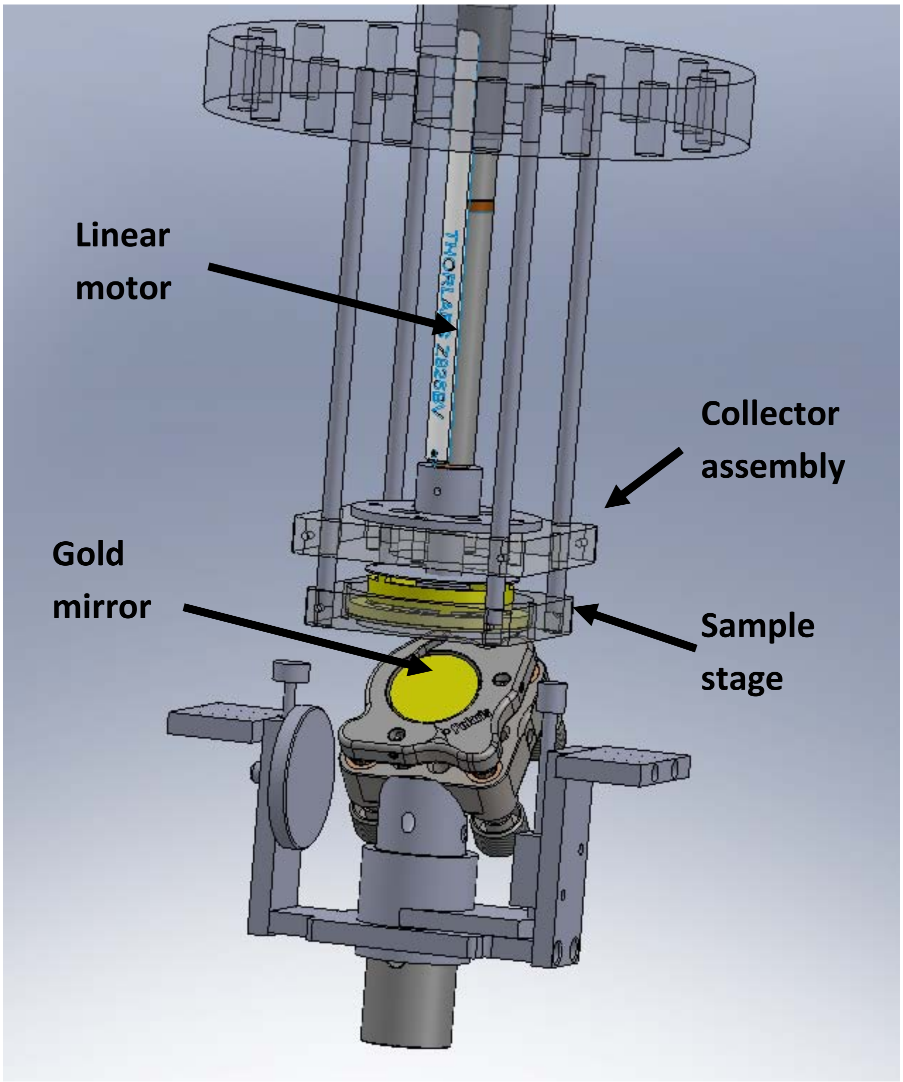

Figure 3: TECsim assembly with linear motor, collector assembly and sample stage attached to the top flange of the chamber. The Au mirror is mounted on a special mirror mount attached to the chamber on a fixed position.

2.1.3 Heating/Laser system

Heating of the emitter cathode samples was achieved by using a continuous wave CO_2 laser (Synrad, Firestar V40 series) with wavelength of λ= 10.6 µm (infrared and invisible to the eye) and an output power of P= 40 W. The advantages of using a laser heating system are discussed in Chapter 3. This laser is linearly polarised with a TEM 00 mode. The beam diameter is 2.5 mm and the beam divergence is < 7 mrad. This laser is air cooled and remotely controlled with a control unit supplied by the same manufacturer. The laser beam is guided towards the chamber by 2 gold-coated copper mirrors and feeds into the chamber through a ZnSe window (Thorlabs.Inc, WG71050-G). Once inside the chamber, the beam is defected upwards by an gold coated copper mirror so that it can reach the sample mounted on the sample stage.

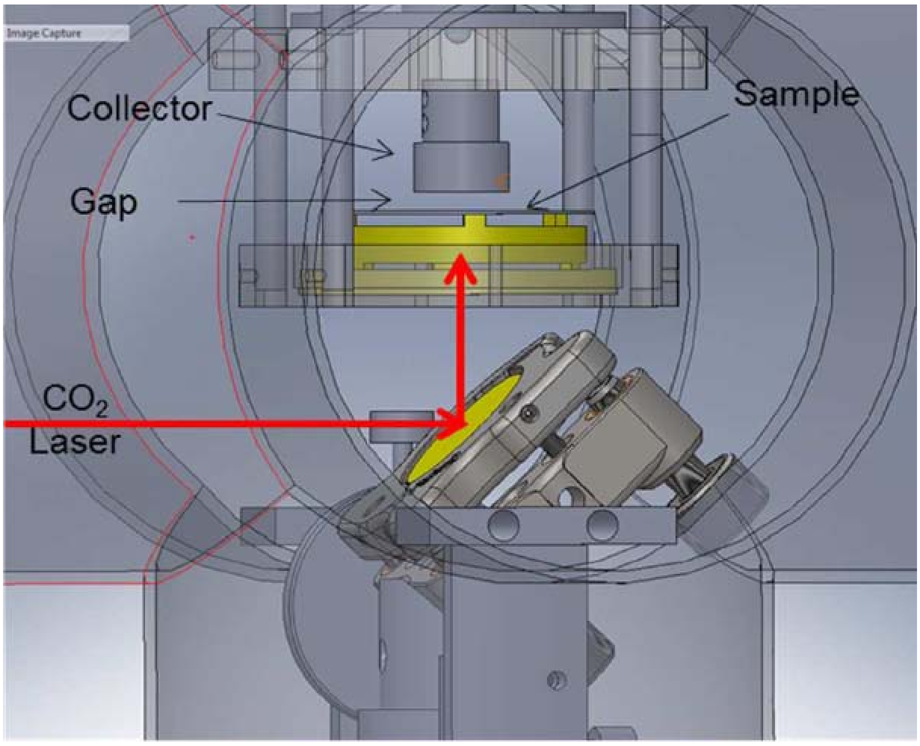

Figure 4: Laser beam path inside the TECsim.

The gold mirror inside the chamber is mounted on a precision vacuum-compatible mirror mount (Thorlabs.Inc, Polaris K1 kinematic mount) that is attached onto a 25 mm diameter beam pole. This beam pole is mounted on a custom-made mechanism that allows for easy mirror alignment as well as a solid and mechanically stable mounting point. It was necessary to build such a mechanism because of the reduced dimensions of the chamber and the absence of any mounting points for the mirror on the inner surfaces of the chamber.

The laser could heat any material as long as it possessed a fair absorbance at the wavelength of the laser. However the main samples used for heating were free-standing polycrystalline boron-doped diamond (BDD TM100, Element 6) and molybdenum (Mo) plates. Boron-doped diamond (BDD) has a high absorbance due to its high doping level and high number of grain boundaries and lattice dislocations. Conversely, Mo plates are quite reflective at the wavelength of the laser.

So in order to reach high temperature, a laser surface modification process had to be applied to their back surface before use. This is discussed in depth in Chapter 3.

2.1.4 Electrical configuration

The TECsim operates on a pseudo open-circuit configuration where the different elements are connected in series. The circuit starts from the collector and ends at the sample. Although there is no physical connection between sample and collector across the gap, when thermionic emission occurs, electrons travel from the sample to the collector through the vacuum closing the electrical circuit. This causes the gap to behave like a voltage controlled current source, regulated by the voltage bias applied by a power supply.

The collector is electrically connected to a regulated variable linear DC power supply (Mastech, HY3003D) so that the collector can be positively biased to attract the electrons emitted from the sample. The power supply is connected in series to an ammeter (Keithley 2750, Tektronix) that then returns the connection to the sample. The error of the reading on the range of the measurements for this thesis is calculated as follows: $\varepsilon = \pm (6 \times 10^{-5} \times \text{reading} + 6 \times 10^{-7})$

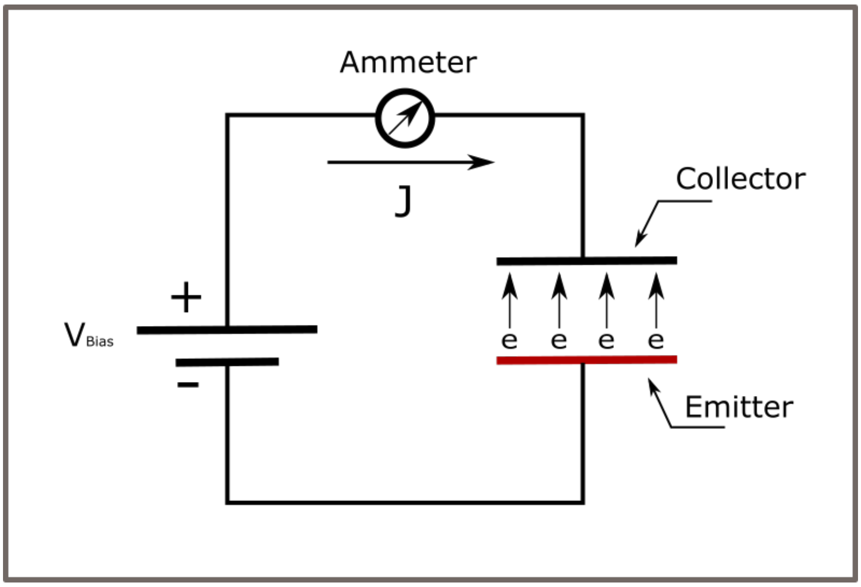

Figure 5: TECsim electric circuit diagram.

2.1.5 Temperature measurement

For the experiments carried out in the TECsim, temperature is one of the most important experimental parameters. In TE experiments, the emission current is a quadratic function of the temperature, making the current extremely sensitive to temperature. For heating experiments the importance of measuring the correct temperature is obvious. Therefore great care had to be taken to achieve accurate temperature readings.

The temperature of the samples on the TECsim is measured simultaneously with a thermocouple (TC) and a pyrometer. The TC is a standard type-K thermocouple with a measurement range from -200 °C to 1350 °C. It is clamped on the quartz plate that supports the sample in such a way that the TC junction is pressing firmly against the sample to ensure a good contact throughout the experiment.

The temperature is also monitored with a two colour pyrometer (Spotmeter R160, Land Instruments International. Ltd). This pyrometer has two detectors each sensitive to a different wavelength: detector 1: λ_1= 1.0 μm and detector 2: λ_2= 1.5 μm. This allows the pyrometer to work in ratio mode, so that the measurements are independent of the different emissivities of the material for the different wavelengths of emitted radiation and therefore improving the accuracy of the measurements. The temperature range of the pyrometer combining the two detectors is 250 °C - 1600 °C, while the ratio mode range is 550 °C - 1600 °C. The resolution of the pyrometer is R = 0.1 K and the uncertainty $U = 2.5 \times 10^{-3} \times T$ or 2 K, whichever is higher.

This pyrometer has an adjustable focal length ranging from 300 mm to ∞. The spot size of the pyrometer, the circular area over which the thermal radiation is collected to perform the measurements, is dependent upon the focal distance reaching a minimum for a circle 2 mm in diameter and a focal length of 300 mm. Due to design constraints the pyrometer measures the samples from the side, and as the samples are typically only 0.5 mm high, they represent a difficult target for optical pyrometers. For the correct operation of the pyrometer, the target object has to fill as much as possible of the spot size to provide accurate readings. In our case the target area is smaller than the spot size, but as the pyrometer is a 2-colour type, it counteracts the effects of a partially filled area.

2.1.6 Residual Gas Analyser

The TECsim has a residual gas analyser (RGA) (Dycor LC-D series RGA, Ametek.Inc) incorporated onto the chamber. This RGA carries out gas mass spectrometry on the residual gases inside the vacuum chamber, and it can detect variations of the partial pressure of gasses in real time. This is used to detect molecules desorbing from the sample surface. The RGA used for this study can detect atomic/molecular masses ranging from 1 amu to 100 amu. The working pressure range is 1×10^{-14} mbar to 1×10^{-4} mbar. The RGA uses electrons emitted from a hot filament to ionise the gas molecules present in the chamber, which are then directed towards a quadrupole mass analyser that filters the ions according to their mass to charge ratio (*m/z*) so that they are registered by a detector.

2.1.7 Control and automation system

The TECsim is a semi-automated system which can be programmed to automatically perform a series of heating-cooling routines while recording a series of variables, like temperature or current, for later analysis. The automation of the TECsim has been implemented using LabView (Labview, National Instruments), a visual programming language. A specific program, or virtual instrument (VI) for the case of LabView, has been created to control the TECsim. This VI interfaces with most of the devices that are connected to the TECsim allowing data acquisition and instrument control. The data acquisition or inputs for the VI are: thermocouple, pyrometer, ammeter, and pressure gauge; while the instrument control or output is the CO_2 laser.

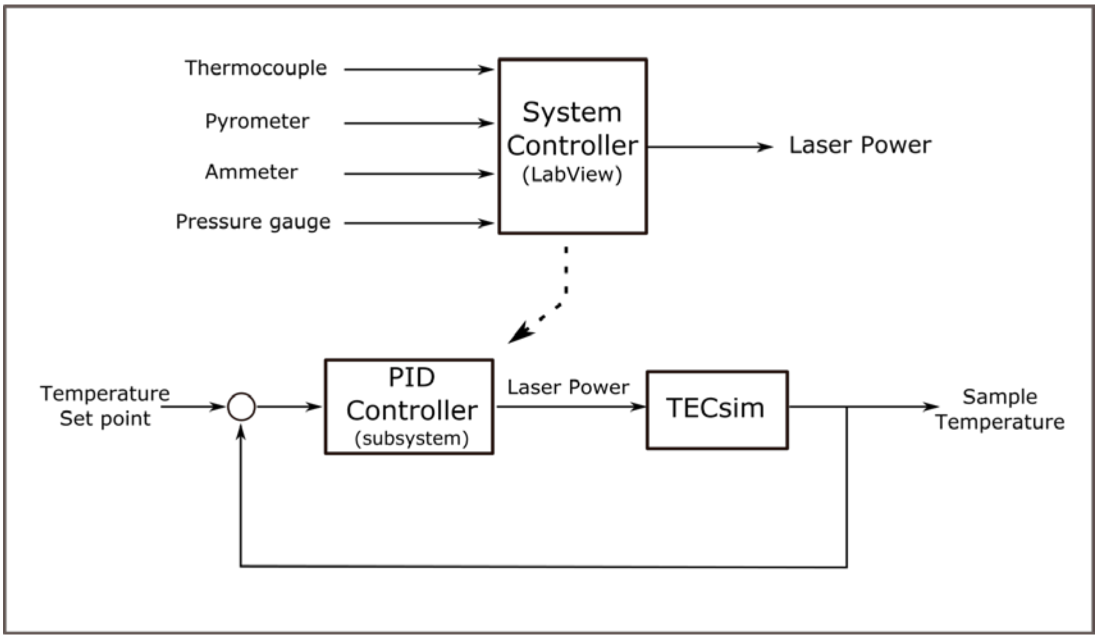

Figure 6: (Top): Inputs and outputs of the TECsim system controller. (Bottom): PID regulator diagram.

The VI has implemented a proportional integral derivative (PID) closed-loop controller that adjusts the laser power to maintain the temperature of the sample at the desired value indicated by a setpoint. The controller can maintain the sample temperature within 0.1 K of the setpoint value. This PID controller is also used to created heating-cooling routines for the sample, allowing multiple ramp-up, hold and ramp-down events to be performed according to a pre-programmed sequence.

2.2 Work function measurements techniques

When measuring the work function (WF), there are two clearly different sets of techniques: absolute methods and relative methods. As the name indicates, the absolute methods provide an absolute value of the WF, whereas the relative methods provide a value relative to a reference electrode. So to obtain the absolute value, it is necessary to calibrate the reference electrode against a sample of known WF. The absolute methods rely on electron emission from the sample under examination. This electron emission can be stimulated thermally (thermionic emission), with high electric fields (field emission) or with light irradiation (photoelectron emission). The relative methods rely on the contact potential difference between a sample and a reference electrode that are ohmically connected. Among these types of methods is the vibrating capacitor method, also known as the Kelvin probe method. The following is an explanation of some of the methods relevant to this study.

2.2.1 Thermionic emission

When a homogeneous monocrystalline metal surface is heated to a high enough temperature, electrons may leave its surface if their thermal energy has increased enough to overcome the potential energy surface barrier of the solid. This phenomenon is called thermionic emission (TE). The current density per unit area is given by the Richardson-Dushman equation[3]:

$$J = AT^2 e^{-\frac{\phi}{k_B T}} \qquad (2.1)$$

$$A = \frac{4\pi m k_B^2 e}{h^3} = 120 \ \frac{A}{cm^2 K} \qquad (2.2)$$

where A is the Richardson constant, T is the temperature in Kelvin, ϕ is the WF of the surface, k_B is the Boltzmann constant, e is the electron charge, m is the electron mass and h is the Planck constant. A typical TE experiment (see Fig.5) consists of two parallel plates separated by a small vacuum gap of less than 1 mm. One electrode is the heated sample or ‘emitter’ and the other is the cooler ‘collector’. The emitter is heated to a certain elevated temperature so that it emits electrons that are harvested by the collector. Subsequently, the current can be plotted against temperature. Then, by fitting the Richardson-Dushman equation to the current plot, the absolute value of ϕ can be found. This method has been employed during this PhD and carried out on the TECsim apparatus described previously.

Once the TE starts, the gap between emitter and collector is filled with a cloud of electrons that prevent the electrons emitted from the surface reaching the collector due to Coulomb repulsion. This is known as the 'space-charge effect'. To mitigate this space charge, a small accelerating electric field needs to be applied between the emitter and the collector. However, this voltage lowers the potential barrier of the surface by the so called Schottky effect[4] so a correction must be applied to find the real WF value from the TE experiment (see Fig.7).

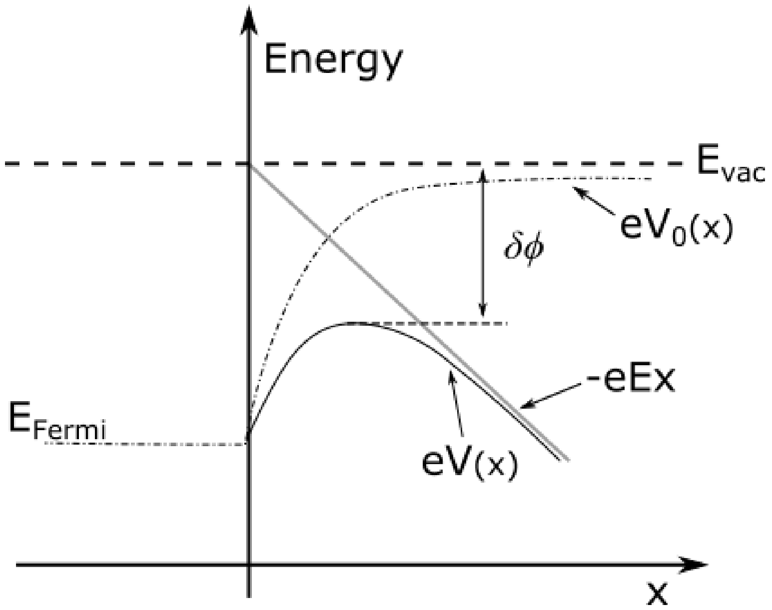

Figure 7: Schottky effect diagram. Variation of the surface potential energy on a metal surface. $V_o(x)$ is the image potential, $V(x)$ is the corrected potential if an electric field E is applied, x_o is the position of the potential maximum, eV_∞ is the position of the vacuum level, ε_0 is the vacuum permitivity, E_F is the Fermi level and $\delta\phi$ is the WF decrease due to the applied external field.

If we assume that the surface potential has an inverse hyperbolic shape:

$$V_0(x) = \frac{e}{16\pi\varepsilon_0 x} \qquad (2.3)$$

where V_0(x) is the image potential, V(x) is the corrected potential in an electric field E is applied, x_0 is the position of the potential maximum, eV_∞ is the position of the vacuum level, ε_0 is the vacuum permitivity, E_F is the Fermi level and $\delta\phi$ is the WF decrease due to the applied electric field.

If an electric field E is applied, this leads to a lowering of the potential barrier by:

$$\delta\phi = e\left[\sqrt{\left(\frac{e}{4\pi\varepsilon_o}\right)\sqrt{E}}\right] \qquad (2.4)$$

An alternative method of finding the value of the WF, apart from fitting the Richardson-Dushman equation to the data, is to measure the saturation current J for different temperatures T and electric fields E. Then it is possible to plot $\ln J\ vs\ E^{\frac{1}{2}}$, which is called a Schottky plot, to extrapolate the value of J for E=0 for a number of different temperatures. Then, these values of $J(E=0)=J_0$ are used to build a Richardson plot or $\ln\frac{J_0}{T^2}\ vs\ \frac{1}{T}$. The slope of this plot leads to a value called the Richardson WF or ϕ^*.

$$\phi^* = -k_\mathrm{B}\left[\frac{\mathrm{d}\left(\ln\frac{J_0}{T^2}\right)}{\mathrm{d}\left(\frac{1}{T}\right)}\right] \qquad (2.5)$$

By combining Eq.3 and Eq.5 we obtain:

$$\phi = \phi^* + T\left(\frac{\mathrm{d}\phi}{\mathrm{d}T}\right) \qquad (2.6)$$

which relates the true WF, ϕ with the Richardson WF, ϕ *. However, the term $\mathrm{d}\phi/\mathrm{d}T$ is not constant with temperature so the assumption that for $T\to 0$, $\phi^* \approx \phi$ is not necessarily true.

2.2.2 Ultraviolet Photoelectron Spectroscopy

Ultraviolet photoelectron spectroscopy (UPS) makes use of the photoelectric effect. If an electron on the surface of a material absorbs an incoming photon and acquires enough energy to overcome the surface potential barrier (WF), the electron can be ejected from the material. This phenomenon was explained by Einstein in 1905, who introduced the following formula:

$$E_k = h\nu - \phi \qquad (2.7)$$

where, E_k is the kinetic energy of the emitted electrons. h the Planck constant, ν the frequency of the incoming photon and ϕ the WF of the surface. UPS can be used to determine the absolute WF of a surface by illuminating it with a helium I source lamp with an energy of 21.22 eV and analysing the electron emission intensity I_e vs E_k. This gives an averaged absolute value for the WF of the surface.

2.2.3 Kelvin probe & the vibrating capacitor method

This technique is based on the vibrating capacitor method developed by Kelvin[6] and Zisman[7]. This method produces a relative value between the WF of two surfaces: the sample and the reference electrode. This value is the contact potential difference or *CPD*.

$$CPD = \phi_{ref} - \phi_{sample} \qquad (2.8)$$

This *CPD* creates an electric field between the two electrodes. The implementation of this technique is as follows. Two parallel plates are brought to within a close distance, one being the reference electrode and the other the sample to be analysed. These two plates are connected with an ammeter and a DC voltage source. The plates can be vibrated relative to each other causing a periodic change in the gap that separates them (see Fig.8). The two plates form a capacitor with a capacitance *C* given by:

$$C = \varepsilon_{\mathrm{r}}\varepsilon_0 \frac{A_{\mathrm{plate}}}{d} \qquad (2.9)$$

where ε_{r} is the relative permittivity, ε_0 is the vacuum permittivity A_{plate} is the area of the plates and d is the gap distance between the plates.

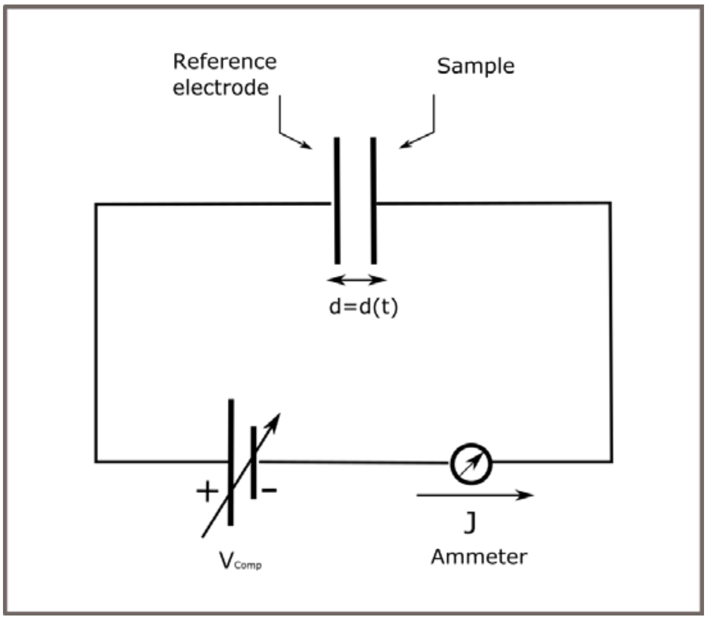

Figure 8: Vibrating capacitor method diagram.

If one of the plates vibrates with respect to the other, the gap between the plates changes and so does the capacitance. This in turn, creates a current through the circuit connecting the plates, given by:

$$i = V_{\text{plates}} \frac{dC}{dt} \qquad (2.10)$$

where V_{plates} is the potential difference between the two plates given by the sum of *CPD* and compensation voltage from the voltage source (V_{comp}):

$$\mathrm{V}_{\text{plates}} = CPD + V_{\text{comp}} \qquad (2.11)$$

Therefore, in order to obtain the *CPD*, V_{comp} has to be adjusted so that V_{plates} and consequently the current flow drop to zero. This means that:

$$CPD = -V_{\text{comp}} \qquad (2.12)$$

2.3 Atomic force microscopy

Following the ground-breaking invention of the scanning tunnelling microscope by Binnig Rohrer[8] in 1982, atomic force microscopy (AFM) was developed a few years later in 1986 by Binnig, Quate & Berger[9]. In AFM, a cantilever terminated by a sharp tip is brought to contact with the surface and rastered across it while mapping its topography, achieving a lateral and height resolution of less than a nanometre. There is a number of subtypes of AFM but this study is concerned with non-contact AFM (nc-AFM) and its variant Kelvin probe force microscopy (KPFM).

2.3.1 Non-contact AFM

As its name indicates, in nc-AFM the tip does not touch the sample, which avoids the wearing of the tip and makes it convenient for hard and soft samples. However, it needs a high quality factor *Q*, which usually can only be obtained under vacuum conditions. There are two modes of operation: amplitude modulation and frequency modulation, but we are only focused on the frequency modulation mode that was first introduced by Albrecht *et al*[10] in 1991.

In frequency modulation mode, a cantilever is vibrated at its near resonant frequency with an amplitude of a few nanometres. Then, when the tip gets closer to a surface, the vibration frequency of the cantilever changes producing a frequency shift (Δf) with respect to the natural frequency due to van der Waals forces arising from the interaction between tip and surface. This occurs in such a way that the closer the tip of the cantilever is to the surface the larger the change in resonant frequency. Moreover, as the tip operates at very close distances from the surface, the interaction forces are repulsive, which causes a negative frequency shift ($0 > \Delta f$).

Therefore, by using a phase-locked loop that tracks the cantilever's resonance frequency it is possible to control and maintain the tip-surface distance and scan it across the surface using either a constant height or a feedback mode. We can describe the oscillation of the tip by its equation of motion:

$$m\ddot{z} + \frac{m\omega_0}{Q}\dot{z} + kz = F_{\mathrm{ts}} + F_0\cos(\omega_{\mathrm{d}}t) \qquad (2.13)$$

where k is the cantilever spring constant, Q the quality factor, F_{ts} the tip-surface interaction, F_0 the amplitude of the driving force, m the mass of the cantilever,and ω_{d} the angular frequency of the driving force. The natural frequency of the cantilever in free space without tip-sample interaction ($F_{\mathrm{ts}}=0$) is:

$$\omega_0 = 2\pi f_0 = \sqrt{\frac{k}{m^*}} \qquad (2.14)$$

where m^* is the specific mass of the cantilever that takes account of its geometry. However, when the tip is close to a surface, it interacts with a number of short-range and long-range forces like van der Waals forces, electrostatic forces or chemical binding forces, among others. These in turn change the resonant frequency of the cantilever.

Solving Eq.2.13 for small amplitude oscillation and small force gradients we obtain an approximation for the frequency shift, which shows that attractive forces alter the frequency shift towards lower frequencies and *vice versa*:

$$\Delta f_0 = -\frac{f_0}{2k}\frac{\partial F_{\mathrm{ts}}}{\partial z} \qquad (2.15)$$

2.3.2 Kelvin probe force microscopy

KPFM is an implementation at small scale of the Kelvin probe method or vibrating capacitor method (see sect.2.2.3) using nc-AFM developed initially by Nonnenmacher *et al* [11]. With KPFM it is possible to perform simultaneous mapping of the topography of the surface and the local WF. However, the lateral resolution of the WF mapping is lower than that of the topography due to the fact that both the area under the tip and its surroundings contribute to the WF value.

In our implementation of the Kelvin method, the vibrating capacitor is formed by the sample and the vibrating cantilever. But in this case, instead of using the current between the two capacitor plates as a control parameter, KPFM uses the electrostatic force. In this way, the extreme sensitivity of nc-AFM to force gradients can be fully exploited. Two voltages are applied to the tip simultaneously in KPFM: A compensation DC voltage (V_{dc}) and an AC excitation voltage with an amplitude V_{ac} and a frequency ω_{ac}. This oscillating voltage induces a cantilever oscillation with the frequency ω_{ac}. So, if we consider the tip-sample system as a capacitor, the electrostatic force between the plates is[12]:

$$F_{el} = -\frac{1}{2}\frac{\partial C}{\partial z}\left[V_{dc} - CPD + V_{ac}\sin\omega_{ac}t\right]^2 \qquad (2.16)$$

where $\frac{\partial C}{\partial z}$ is the capacitance gradient between tip and sample. The *CPD* is:

$$CPD = \frac{\Delta\phi}{e} = \frac{(\phi_{sample} - \phi_{tip})}{e} \qquad (2.17)$$

where *e* is the electron charge.

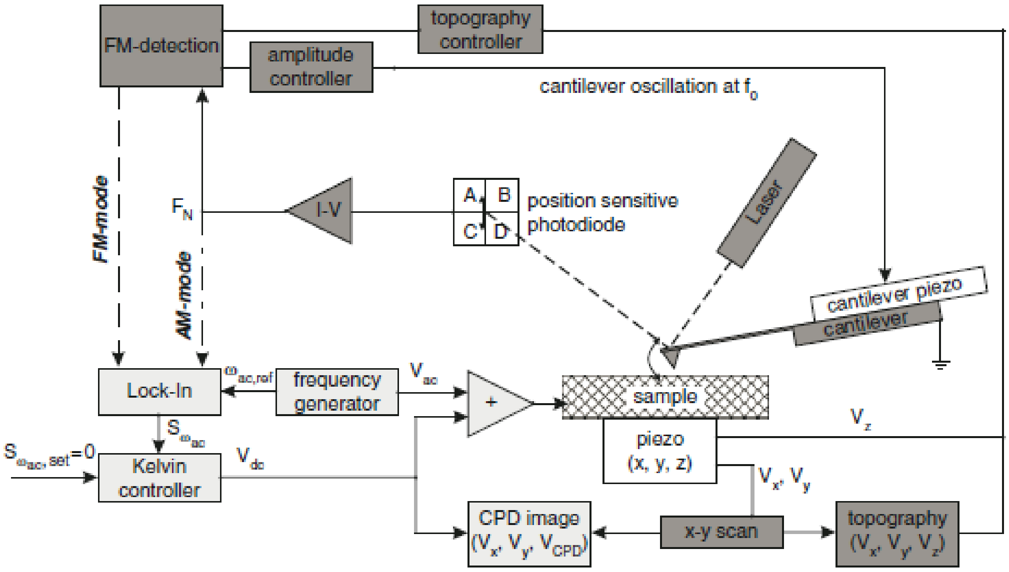

Figure 9: Block diagram of the KPFM electronic set up. Dashed lines correspond to frequency-modulation mode and dashed-dotted line to amplitude-modulation mode. Taken from[12].

If we divide Eq.2.16 into different components we have:

$$F_{dc} = -\frac{\partial C}{\partial z}\left[\frac{1}{2}(V_{dc} - CPD)^2 + \frac{V_{ac}^2}{4}\right]; \qquad (2.18)$$

$$F_{\omega_{ac}} = -\frac{\partial C}{\partial z}(V_{dc} - CPD)V_{ac}\sin\omega_{ac}t\ ; \qquad (2.19)$$

$$F_{2\omega_{ac}} = \frac{\partial C}{\partial z}\frac{V_{ac}^2}{4}\cos 2\omega_{ac}t \qquad (2.20)$$

If nc-AFM is operating in frequency-modulation mode, the applied oscillating voltage results in an oscillation of the frequency shift of the cantilever Δf with a frequency ω_{ac} that is detected with a lock-in amplifier. So according to Eq.2.16 and Eq.2.19 the signal is proportional to the force gradient:

$$\Delta f_0(\omega_{\mathrm{ac}}) \propto \frac{\partial F_{\omega_{\mathrm{ac}}}}{\partial z} = \frac{\partial^2 C}{\partial z^2}(V_{\mathrm{dc}} - CPD)V_{\mathrm{ac}}\sin\omega_{\mathrm{ac}}t \qquad (2.21)$$

The ω_{ac} has to be chosen carefully, as if it is too low there will be cross-talk with the topography signal, while if it is too high the signal intensity of the electrostatic force decreases, which hampers the frequency-shift detection. Therefore, by monitoring the frequency shift of the cantilever and applying a compensation voltage V_{dc} it is possible to determine the *CPD* between the tip and sample. This can be used to calculate the WF of the sample by calibrating the tip against a material with a known work function.

2.3.3 Laser-assisted KPFM

For this study we have used a laser to excite samples made of nanoparticles deposited on semiconducting films while scanning them with KPFM. This technique, although it has some similarities with surface photovoltage microscopy[13] and might be confused with it, it is substantially different from the latter both in its goals and implementation.

Here, we used laser-assisted KPFM (LA-KPFM) in order to study the plasmoelectric potentials[14] generated in nanoparticles upon illumination (see Fig.10).

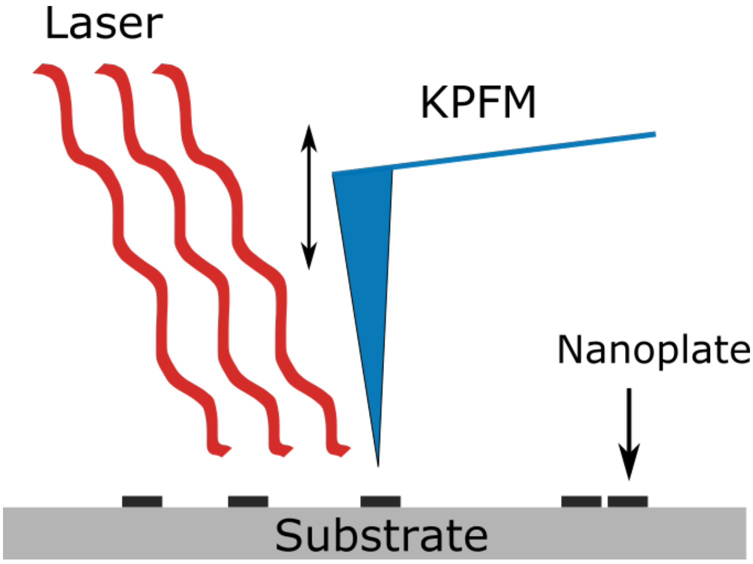

Figure 10: Laser assisted KPFM diagram.

For our setup, a continuous wave infrared diode laser with circular polarisation and a maximum output power of 11.8 mW, measured after the fibre, was coupled to a multimode optical fibre with a core diameter of 50 µm to guide the beam towards a "cage" optical system. This "cage" system is equipped with a beam collimator and an optical lens (*f*=300 mm) used to focus the beam onto the surface of the sample through a borosilicate viewport (the sample is inside a UHV chamber). The beam arrives at the sample with an oblique angle of 28° relative to the surface of the sample, and the plane of incidence forms a 63° angle from the longitudinal axis of the sample. Under these conditions, the laser spot on the sample is an ellipsoid with a short axis of ≈1.4 mm and a long axis of ≈3 mm. The KPFM measurements were performed in the centre of this ellipsoid. In order to avoid any light contamination, all the viewports of the vacuum chamber were sealed to stop light entering the chamber. The pressure gauge of the system was also switched off due to the fact that it is an incandescent filament that emits radiation at the resonant frequencies of our sample.

LA-KPFM was performed using platinum-iridium-coated silicon cantilevers (PPP-NCHPt, Nanosensors) with a frequency of f ≈300 kHz, a force constant of F_n = 10-130 N/m and a tip radius R_t < 25 nm. The KPFM was operated in frequency modulation mode with a V_{ac} = 1 V.

2.3.4 Tip calibration procedure

In order for KPFM to provide absolute values of WF, the WF of the tip of the cantilever has to be calibrated against a surface of known WF. For this study, highly oriented pyrolytic graphite (HOPG) was used as a calibration source. HOPG is a convenient source for calibration as it is easy to clean in UHV conditions and not prone to contamination. HOPG was annealed at 500 °C for 16 h in UHV until the pressure of the chamber was 1×10^{-9} mbar. Then, it was allowed to cool down for 1 h while the pressure of the chamber decreased rapidly to 8.4×10^{-11} mbar.

For the tip calibration, a series of 12 KPFM point scans were performed on the cleaned HOPG. Each scan was 150 × 150 pixels which equates to 22500 pixels/image. Then each image was post-processed by fitting a Gaussian function to the *CPD* histogram to extract the peak value of the *CPD* measured with the tip. Once all the images were post-processed, the average of all the peak values was calculated as $CPD_{\text{tip-HOPG}} = 0.3796$ eV with a standard error of $SE = 0.00469$ eV (see Fig.11).

As HOPG has a WF of $\phi_{\text{HOPG}} \approx 4.6$ eV[15–19] , the WF of the tip was calculated with the following formula:

$$CPD = \emptyset_{HOPG} - \emptyset_{tip} \qquad (2.22)$$

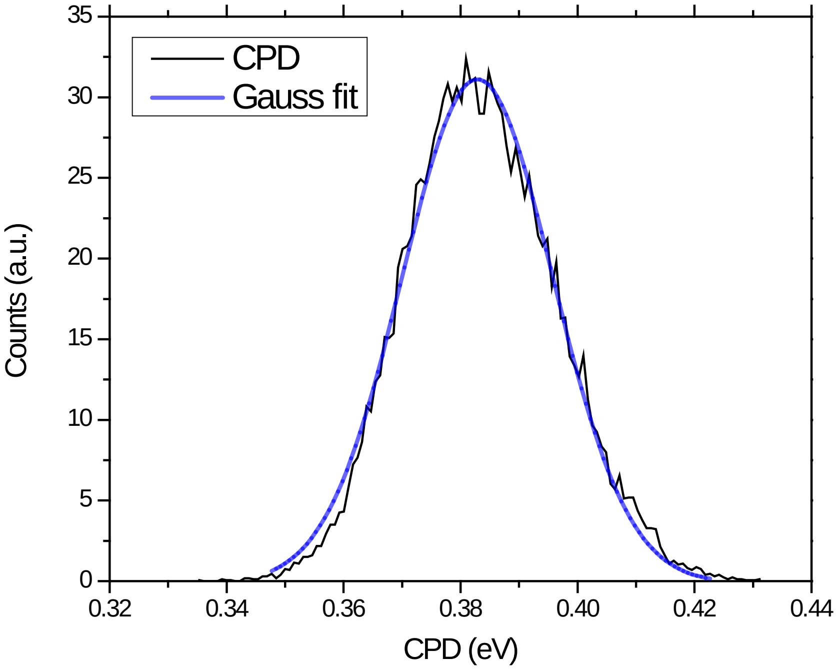

Figure 11: Example of a Gauss function fitting to the *CPD* distributions of one of the calibration point scans in HOPG.

where *CPD* is the contact potential difference as measured by KPFM, ϕ_{HOPG} is the HOPG WF and ϕ_{tip} is the WF of the tip. The WF of the tip was estimated to have a value of $\phi_{\mathrm{tip}} \approx 4.22$ eV.

2.3.5 Instrument: Scanning Probe Microscope Omicron VT XA

The LA-KPFM measurements performed in this PhD were carried out using a SPM Omicron VT XA (Scientia-Omicron, Germany). This instrument is a UHV scanning probe microscope that can perform a number of different techniques including: nc-AFM, KPFM, contact mode AFM and conductive AFM and STM.

The instrument is equipped with the following *in situ* surface fabrication techniques:

-Quad e-beam evaporator (Mantis Depositions, Quad): This hosts 4 independent crucibles to perform physical vapour deposition with metals or organic substances that can be controlled individually.

-Single e-beam evaporator (Focus, EFL 3): Used for physical vapour deposition. It has a single crucible and it is mounted facing the scanning stage so that evaporation can performed while scanning.

-Oxygen cracker (Mantis Deposition Ltd, MGC-75): This ionises oxygen gas molecules to produce a stream of atomic oxygen that can be directed towards the sample.

Figure 12: Omicron VT AFM XA Scanning probe microscope.

-Argon sputterer: This ionises Ar gas and accelerates the ions directing them against the sample. It is also used to clean surfaces.

-Heating arm: This instrument can heat samples up to 1500 °C and it is used to anneal samples and to remove adventitious contaminants from the surface of samples.

The Omicron microscope can control the temperature of the sample while it is being analysed within a temperature range from 30 K to 500 K. For sample cooling, a helium flow cryostat is fitted, while heating is achieved using a closed feedback loop controlled heating resistor. All the systems described previously are encased in a stainless steel UHV chamber. The chamber vacuum is maintained with a series of pumps. The chamber has a rotary pump that lowers the pressure down to 1×10^{-2} mbar connected to a turbomolecular pump that takes the pressure to the 1×10^{-9} mbar regime. An ion pump lowers the pressure further to 1×10^{-10} mbar. The final base pressure of 5×10^{-11} mbar is achieved by the periodic activation of a titanium sublimation pump every 12 hours.

In order to isolate the system from mechanical vibrations, the instrument is mounted on top of a 23 tonne concrete slab suspended on pneumatic actuators that acts as a low-pass frequency filter for mechanical vibrations, so that only vibrations with a frequency lower than 16 Hz can bypass the slab and reach the instrument. The instrument is also equipped with an optical system to feed a laser beam into the chamber and focus it on the sample (see sect.2.1.3) to enable the realisation of LA-KPFM experiments.

2.4 X-ray Photoelectron Spectroscopy

X-ray photoelectron spectroscopy (XPS) was developed by Siegbahn [20] in the 1950s, and it is a photoelectron spectroscopy technique that provides information about the elemental composition of a material and the electronic or oxidation state of those elements as well as other information. Its original name ‘electron spectroscopy for chemical analysis’ (ESCA) was more specific in showing the capabilities of this technique. XPS is a very surface sensitive technique, as it samples only the first 10 nm of material. This number can be reduced by performing XPS at a grazing angle to reduce the penetration depth of the X-rays. The XPS technique is based on the photoelectric effect and the sample is excited with X-rays, in contrast to UPS explained earlier (see Sect.2.2.2) which uses ultraviolet light. In XPS, the X-rays are used to extract the core electrons from the different elements and these are then analysed to measure their kinetic energy,

E_k. From knowledge of the kinetic energy, it is possible to obtain the binding energy (E_b) of the core electrons:

$$E_k = h\nu - E_b - \phi \qquad (2.23)$$

where h is the Planck constant, ν the frequency of the incoming X-ray photon and ϕ the WF of the analyser. Then the electron intensity signal is plotted against E_b, where the peaks of the plot represent the binding energies of the different elements present in the sample. Usually, a wide scan is performed first to have a preliminary idea of the elements present in the sample, followed for a series of scans focused on the energy ranges of interest at higher energy resolution.

The light source used for these experiments is either a non-monochromatic Mg-K (1254 eV) or a monochromatic Al-K (1487 eV) source. As mentioned earlier, XPS can offer information on the oxidation state of the components of a sample. Each element has an associated binding energy, but the oxidation state of the atoms will shift the binding energy on the XPS spectra. If there is an increase in the negative charge of an atom, the binding energy will shift toward lower values, and *vice versa*. Lastly, XPS is a technique that requires ultra-high vacuum to work, because electrons need to have a long enough mean free path so that they can travel through the focusing lenses and electron energy analysers that are necessary to implement this technique.

2.4.1 Instrument: nanoESCA

The nanoESCA[21] system is a multipurpose instrument that implements several surface analysis techniques. Among these techniques are UPS, XPS, angle-resolved photoelectron spectroscopy (ARPES) and low energy electron diffraction (LEED). The unit employed for the experiments in this PhD was a nanoESCA mark1 located in CEA-Saclay (France) composed of two UHV chambers. One chamber is used for sample preparation while the other is used solely for sample analysis. The preparation chamber is equipped with the usual surface preparation techniques such as sample heating or Ar sputtering.

The analysis chamber is equipped with an energy-filtered photoelectron emission microscope (EF-PEEM) with a double hemispherical analyser[22]. The samples can be excited with an X-ray source, a He I source or a Hg source. This configuration allows WF mapping with an energy resolution of ≈ 100 meV , lateral resolution of ≈ 200 nm , and elemental mapping with the same lateral resolution. Traditional UPS and XPS are also possible. The instrument operates under UHV conditions with a base pressure of $\approx 5\times10^{-11}$ mbar.

2.5 Electron microscopy and associated techniques

2.5.1 Scanning Electron Microscopy

Scanning electron microscopy (SEM) is a microscopy technique that creates images of a sample by rastering a focused electron beam over its surface. SEM can achieve a resolution of around 1 nm. This technique is performed under high vacuum conditions to provide a mean free path for electrons long enough that they can travel through the multiple electromagnetic lenses that focus and guide the beam of electrons without suffering collisions.

The samples need to be conductive, at least on their surface, and properly grounded, otherwise samples will charge up and start hampering the imaging process. The typical SEM apparatus has an electron gun that generates electrons. This can be made out a Tungsten filament that generates electrons by thermionic emission or a lanthanum hexaboride LaB_6 crystal that generates electron with the same mechanism. Electrons produced in the electron gun are focused by condenser lenses and then pass through deflector plates that scan the electron beam across the sample. Once electrons hit the sample they produce, through a series of elastic and inelastic scattering, secondary electrons that are captured by the secondary electron detector in order to form an image of the sample.

Other types of electrons are also produced, such as Auger electrons that carry information on the elemental composition of the surface, or backscattered electrons. Fluorescence X-rays are also produced as a result of the electron-beam-sample interactions. These X-rays can be used to analyse the chemical composition of the sample through a technique called energy dispersive X-ray spectroscopy (EDX or EDS).

2.5.2 Transmission Electron Microscopy

In transmission electron microscopy (TEM), a beam of electrons is passed through a thin sample and are subsequently detected by a CCD to form an image of the sample. The sample is usually deposited on a support grid made typically of copper on other material with low reactivity. For the electrons to be transmitted through the sample, it needs to be very thin. This limits the use of TEM to small structures (thickness $\approx$ 100 nm) or requires elaborate sample preparation procedures (e.g. ion-beam thinning) to adapt the sample to this technique. TEM is able to achieve very high resolution, reaching atomic resolution in some cases[23].

Similarly to the SEM, the electrons are generated by a W or LaB_6 electron gun and are then focused and shaped into a beam by a series of electromagnetic lenses and passed through the sample to finally reach an electron detector. TEM also needs high vacuum to guarantee a long mean free path for electrons.

2.5.3 Electron Energy Loss Spectroscopy

A technique closely associated with TEM is electron energy loss spectroscopy (EELS). EELS provides information about chemical composition and also oxidation states of the atoms present on the surface of a sample[24]. This technique is usually implemented on the same instrument used for TEM. When a beam of electrons with a narrow range of kinetic energies passes through a TEM sample, they will experience inelastic scattering causing an energy loss. This can be caused by a series of phenomena like phonon excitation, plasmon excitation, inner- and intra-band transitions and inner-shell ionisations. The energy of the transmitted electrons is detected by an electron spectrometer, and by analysing the spectra it is possible to discern the binding energies corresponding to the atoms present in the sample.

2.6 Fourier Image Spectroscopy

In order to characterise the optical response of a certain material, in our case a silver nanoplate-indium tin oxide system discussed in Chapter 5, a custom-built Fourier image spectroscopy setup[25] has been used. This setup provides information on the reflectance/transmittance and absorbance of light for a range of wavelengths and angles of incidence of the incoming light. This technique has been implemented by using a white-light transmission microscope with a high numerical aperture (NA) (NA=0.75) objective lens as collector and a low NA objective (NA=0.1) as condenser. A quantitative measurement of the angular reflectance or transmittance in a specular configuration can be obtained by scanning the back focal plane image of the high NA collector with a fibre-coupled spectrometer. In our case the experiments were carried out at normal incidence, with a white-light source and in transmission mode.

2.7 Microwave Chemical Vapour Deposition Reactor

Microwave chemical vapour deposition reactors (MW-CVD) use concentrated microwave power inside a resonator chamber to create gas plasmas at high temperature. Although normally used for diamond film synthesis, the technique is applicable to other substances. In this work we used a MW-CVD reactor to hydrogen terminate the surfaces of diamond samples by exposing their surfaces to hydrogen plasma for a period of time. This plasma was generated and maintained in a custom-designed MW reactor[26] with a power of 2 kW and at 2.45 GHz power supply (Muegge GmbH) and generator (see Fig.13).

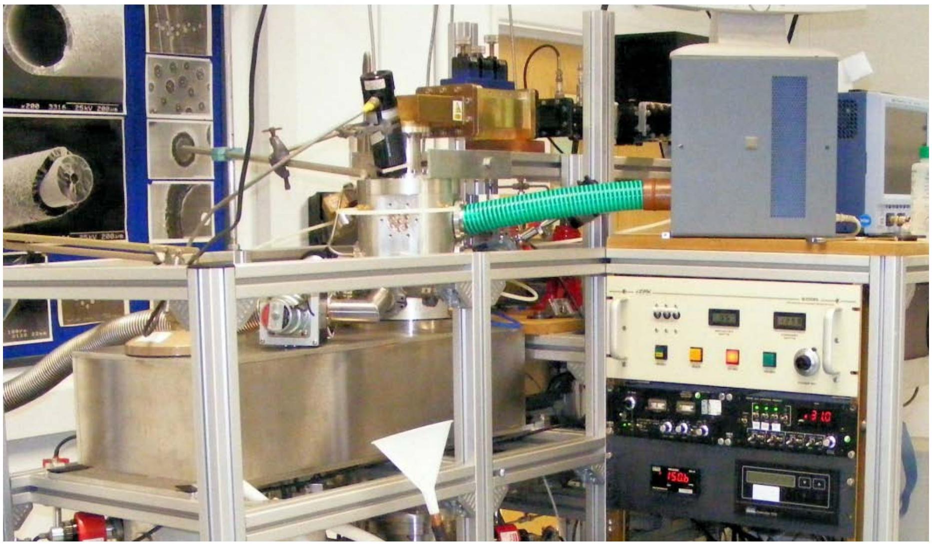

Figure 13: Microwave CVD reactor used for hydrogen termination of diamond surfaces.

The reactor is in the form of a vertical cylinder with an approximate volume of $\approx$ 0.6 L, while the MW power is fed into the top of the chamber via a waveguide and antennae, through a quartz window which acts as a vacuum seal. The gas (hydrogen in our case) flow into the chamber was controlled with mass flow controllers and fed into the chamber with stainless steel pipes. The chamber is pumped down through a flexible stainless steel pipe by a two-stage rotary pump (Edwards E2M8). Stable pressure during operation is achieved with a feedback-loop-controlled throttle valve between the pump and the chamber. The temperature of the substrate is monitored in real time by a one-colour pyrometer.

2.8 Laser micromachining system

A laser micromachining system (Alpha 532, Oxford Lasers) has been used to produce gratings on molybdenum foil. The system has a frequency-doubled Nd:YAG diode-pumped solid-state laser with a wavelength of λ=532 nm. The laser is Q-switched and can be pulsed at different frequencies (1-50 kHz). The energy per pulse can also be controlled. The output power is > 2.5 W @ 10 kHz and the laser spot has a circular shape and a diameter of around $\approx$ 5 μm. The sample is mounted on an electronically controlled stage that allows for movement in the *x* and *y* directions. The range of movement is 150 mm for both axes and the movement resolution is around $\approx$ 1 μm.

The stage and the laser are mounted on a granite frame to dampen mechanical vibrations, while the frame itself is enclosed in a protective metallic enclosure.

Figure 14: Laser micromachining system used in the fabrication of plasmonic gratings.

2.9 Sample preparation

2.9.1 Molybdenum gratings

Plasmonic gratings were prepared on 10 × 10 mm squares of 99% pure molybdenum foil (Goodfellow, Cambridge. Ltd) anneal tempered, with a thickness of 250 µm. The 10 × 10 mm squares were cut from a 100 × 100 mm foil by a water-jet cutting system (Physics Dept workshops), as mechanical methods were found to distort the samples. The substrates have also been cut by laser micromachining using a Nd:YAG laser system (see sect.2.8) at 74.4 J cm^{-2}, 1 kHz repetition rate and with a laser firing distance of 0.2 µm. The flatness of the samples was essential, as the laser machining process used to engrave the gratings is extremely sensitive to the position of the sample relative to the focal point of the laser.

The Gaussian spatial energy distribution of the laser-beam profile combined with the high ablation threshold of molybdenum, allowed us to obtain features smaller than the laser spot size at the focus position. In order to obtain the same groove morphology in all samples, they have all been produced with the same laser firing frequency (15 kHz) and 8 passes per groove. Using a 5-µm-diameter laser spot with a 40 mm focal lens we can obtain circular features with a diameter of

3 µm on the molybdenum substrate. Following there is a table summary with the laser manufacturing parameters for the samples produced.

Table 1: Set of plasmonic gratings produced in molybdenum substrates. A and U are the values of the laser attenuators, E_{pulse} is the energy per laser pulse, Speed is the laser spot speed when patterning the sample, d_f is the laser firing distance, pitch is the period of the patterned grating and FF is the filling factor (see Ch.4 sect 3.3.1). For the samples in the light blue background the FF is kept constant while the pitch is varied and for the samples in light red background the pitch is kept constant and the FF is varied.

Sample	A (%)	U (%)	E_{pulse} (µJ/pulse)	Speed (mm/s)	d_f (µm)	Pitch (µm)	FF
P10.6_FF80	20	55	10	15	1	10.6	80
P10.5_FF80	20	90	15.6	15	1	10.5	80
P10.4_FF80	20	90	15.6	15	1	10.4	80
P10.3_FF80	20	91	15.6	15	1	10.3	80
P10_FF20	20	100	28	22.5	1.5	10	20
P10_FF50	45	100	50	22.5	1.5	10	50
P10_FF80	30	100	30	15	1	10	80

2.9.2 Hydrogen terminated diamond

Two different types of samples were used in order to fabricate hydrogen-terminated diamond samples: single-crystal and polycrystalline (microcrystalline) diamond. The former is a square nitrogen-doped single-crystal diamond grown by the high temperature high pressure method[27] (purchased from Element Six, UK) with a thickness of ≈500 µm and lateral dimensions of 9.5×9.5 mm. The polycrystalline samples used a free-standing boron-doped diamond (BDD) purchased from Element Six (TM100, square slab 10×10 mm) with a thickness of ≈500 µm) onto which was deposited a thin film of ≈2 µm of nitrogen-doped diamond using the MWCVD reactor in the School of Chemistry). This BDD substrate was chosen because of its high laser absorbance. As the samples were intended for TE testing on the TECsim system described previously (Sec.2.1) that employs a laser heating system, maximising the absorbance of the sample is an important feature of the substrates.

The hydrogen termination process was performed in a MW-CVD reactor described previously (see Sect.2.7) by exposing the diamond surface to a hydrogen plasma. The process had three steps:

1-Surface cleaning: MW Power P_{MW}=900 W, hydrogen pressure p_H=62 Torr, substrate temperature T_{sub}=720°C, time t_1= 120 s.

2-Hydrogen termination: P_{MW}=680 W, P_H=20Torr, T_{sub}=450°C, time t_2= 240 s.

3-Cool down: P_{MW}=0 W, P_H=20 Torr, $T_{sub}\rightarrow$20°C, time t_3= 120 s.

Following the termination process the samples would be immediately stored under Ar to prevent surface contamination.

2.9.3 Silver nanoplates on Indium Tin Oxide

Flat silver nanoplates (NanoComposix 1050 nm, PVP NanoXact Silver Nanoplates, mass concentration 0.022 mg/ml) have been selected as plasmonic resonators in order to avoid sudden height variations during the KPFM measurements. The KPFM technique requires conductive substrates, therefore the silver nanoplates have been prepared on top of a transparent conductive substrate formed by 100 nm of indium tin oxide (ITO) with a fully oxygenated surface on top of glass substrate (ITO glass substrate, Ossila).

The colloids with a diameter of 170 nm were deposited by the centrifuge sedimentation method[28]. The substrate was immersed in a 300 μl solution of silver nanoplates colloids diluted by 600 mL of deionized (DI) water with the ITO side towards the rotation axis. Then, 60 μL of 0.1 M HCl was added and the vials were immediately centrifuged at 6000 rpm for 13 minutes. The sample was finally rinsed thoroughly with DI water. The remaining water was evaporated by placing the sample on a hot plate at 80 ˚C. A sample control was also prepared following the same procedure except with the ITO/glass substrate immersed just in DI water and 60 μL of 0.1 M HCl.

Acronyms

TECsim: Thermionic Energy Converter simulator

TE: thermionic Emission

UHV: Ultra High Vacuum

BDD: Boron Doped Diamond

TC: Thermocouple

VI: Virtual Instrument

PID : Proportional Integral Derivative

AFM: Atomic Force Microscopy

nc-AFM: non contact-Atomic Force Microscopy

KPFM: Kelvin Probe Force Microscopy

HOPG: Highly Oriented Pyrolytic Graphite

UPS: Ultraviolet Photoelectron Spectroscopy

XPS: X-ray Photoelectron Spectroscopy

SEM: Scanning Electron Microscopy

EDX or EDS: Energy Dispersive X-rays Spectroscopy

TEM: Transmission Electron Microscopy

MW-CVD: Microwave Chemical Vapour Deposition

NA: Numerical Aperture

List of figures

List of tables

References

1. King, D. A. Thermal desorption from metal surfaces: A review. *Surface Science* **47,** 384–402 (1975).

2. Abdulagatov, I. . *et al.* Thermal conductivity of fused quartz and quartz ceramic at high temperatures and high pressures. *Journal of Physics and Chemistry of Solids* **61,** 779–787 (2000).

3. Richardson, O. W. Thermionic phenomena and the laws which govern them. *Nobel Lecture* (1929).

4. Schottky, W. No Title. *Physikalische Zeitschrift* **15,** 872 (1914).

5. *Solid Surface Physics*. **85,** (Springer-Verlag, 1979).

6. Thomas, W. (Lord K. No Title. *Phil.Mag.* **46,** 82 (1898).

7. Zisman, W. A. A new method of measuring contact potential differences in metals. *Review of Scientific Instruments* **3,** 367 (1932).

8. Binnig, G. & Rohrer, H. Scanning tunneling microscopy. *Surface Science* **126,** 236–244 (1983).

9. Binnig, G., Quate, C. F. & Gerber, C. Atomic Force Microscope. *Physical Review Letters* **56,** 930–933 (1986).

10. Albrecht, T. R., Grütter, P., Horne, D. & Rugar, D. Frequency modulation detection using high-Q cantilevers for enhanced force microscope sensitivity. *Journal of Applied Physics* **69,** 668 (1991).

11. Nonnenmacher, M., O'Boyle, M. P. & Wickramasinghe, H. K. Kelvin probe force microscopy. *Applied Physics Letters* **58,** 2921 (1991).

12. *Kelvin Probe Force Microscopy*. **48,** (Springer Berlin Heidelberg, 2012).

13. Loppacher, C. *et al.* FM demodulated Kelvin probe force microscopy for surface photovoltage tracking. *Nanotechnology* **16,** S1–S6 (2005).

14. Sheldon, M. T., van de Groep, J., Brown, a. M., Polman, A. & Atwater, H. a. Plasmoelectric potentials in metal nanostructures. *Science* **828,** (2014).

15. Schroeder, P. G., Nelson, M. W., Parkinson, B. A. & Schlaf, R. Investigation of band bending and charging phenomena in frontier orbital alignment measurements of para-quaterphenyl thin

films grown on highly oriented pyrolytic graphite and SnS2. *Surface Science* **459,** 349–364 (2000).

16. Zhou, Y. *et al.* A Universal Method to Produce Low-Work Function Electrodes for Organic Electronics. *Science* **336,** 327–332 (2012).

17. Suzuki, S., Bower, C., Watanabe, Y. & Zhou, O. Work functions and valence band states of pristine and Cs-intercalated single-walled carbon nanotube bundles. *Applied Physics Letters* **76,** 4007–4009 (2000).

18. Hansen, W. N. & Johnson, K. B. Work function measurements in gas ambient. *Surface Science* **316,** 373–382 (1994).

19. Takahashi, T., Tokailin, H. & Sagawa, T. Angle-resolved ultraviolet photoelectron spectroscopy of the unoccupied band structure of graphite. *Physical Review B* **32,** 8317–8324 (1985).

20. Siegbahn, K. & Edvarson, K. β-Ray spectroscopy in the precision range of 1 : 105. *Nuclear Physics* **1,** 137–159 (1956).

21. Renault, O. *et al.* Energy-filtered XPEEM with NanoESCA using synchrotron and laboratory X-ray sources: Principles and first demonstrated results. *Surface Science* **601,** 4727–4732 (2007).

22. Escher, M. *et al.* NanoESCA: imaging UPS and XPS with high energy resolution. *Journal of Electron Spectroscopy and Related Phenomena* **144–147,** 1179–1182 (2005).

23. Kisielowski, C. *et al.* Detection of Single Atoms and Buried Defects in Three Dimensions by Aberration-Corrected Electron Microscope with 0.5-Å Information Limit. *Microscopy and Microanalysis* **14,** 469–477 (2008).

24. Egerton, R. F. Electron energy-loss spectroscopy in the TEM. *Reports on Progress in Physics* **72,** 16502 (2009).

25. López-García, M. *et al.* Enhancement and Directionality of Spontaneous Emission in Hybrid Self-Assembled Photonic-Plasmonic Crystals. *Small* **6,** 1757–1761 (2010).

26. Cheesman, A. *et al.* Application of a Quantum Cascade Laser for Time-Resolved, in Situ Probing of CH 4 /H 2 and C 2 H 2 /H 2 Gas Mixtures during Microwave Plasma Enhanced Chemical Vapor Deposition of Diamond. *The Journal of Physical Chemistry A* **110,** 2821–2828 (2006).

27. Pal'yanov, Y. *et al.* Crystal growth and characterization of HPHT diamond from a phosphorus-carbon system. *Diamond and Related Materials* **12,** 1510–1516 (2003).

28. Sheldon, M. T. *et al.* Nanophotonics. Plasmoelectric potentials in metal nanostructures. *Science (New York, N.Y.)* **346,** 828–31 (2014).

Every mathematician knows
it is impossible to understand
an elementary course in
thermodynamics.

-V.I. Arnold

Molybdenum gratings as plasmonic heaters

3

In this chapter, a laser powered heating method for diamond thin films based on plasmonic gratings is described. This method was developed and optimised in order to carry out the thermionic emission tests described in Chapter 4, for which high temperatures (≈ 1000 °C) and accurate temperature control were necessary. This chapter begins with a short introduction to plasmonic coupling and plasmonic heating followed by a derivation of the equilibrium thermal equation for the considered thermal system. A morphological and optical characterisation of the plasmonic samples is then presented along with simulations of the behaviour of the samples with different design parameters. Finally, the results of heating experiments for the different samples are presented, discussed and compared with the thermal model for the system.

3.1 Introduction

3.1.1 Plasmonic heating

Surface plasmon polaritons (SPP) (see Ch.1 sect.1.4) are known to produce localised heating effects[1]. When a SPP is excited on a metallic grating or nanoparticle, electrons are brought up to high-energy states out of equilibrium. After a few picoseconds, the excited electrons decay through electron-electron and electron-phonon interactions causing the energy of the electrons to be transmitted to the metal lattice[2]. This produces an increase of the temperature of the metallic substrate[3].

Plasmonic heating has a number of advantages that made it a suitable candidate to be used as the heating technique to carry out thermionic emission experiments in diamond thin films. The heating is performed using a laser. Given the small mass of the samples, the laser enables a very fast and precise control over the sample temperature thanks to the very low thermal inertia of the system and the fact that the laser power can be changed instantly. Furthermore, the laser cannot produce any spurious currents on the sample that could affect the measurement of thermionic currents. This is not the case with resistive heaters, for example, traditionally used for this kind of experiments.

Diamond thin films can be grown in a variety of substrates like tungsten, molybdenum, platinum[4], copper, silicon or silicon carbide[5]. Usually, plasmonic structures are fabricated in noble metals like gold, silver or platinum[6] but their low melting points ($\approx$ 1000°C) make them unsuitable for high temperature applications. Molybdenum (Mo) was the material selected to implement the plasmonic heating method because it is an optimum substrate for diamond growth[7,8], it is a refractory metal with good mechanical and thermal stability at high temperatures and its optical properties in the far infrared are suitable for plasmonic excitation[9,10] (see Fig.1).

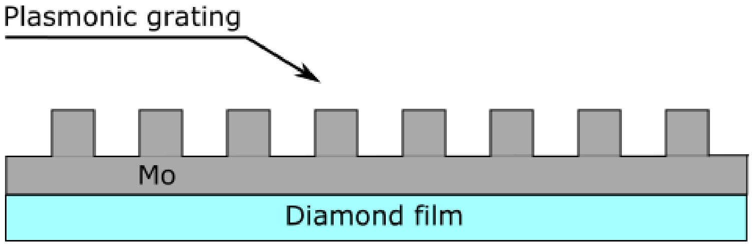

Figure 1: Diagram of the final heating system with a plasmonic grating patterned on one side of a Mo substrate; while the other side is used to grow a diamond film.

Heating of the Mo substrates was performed with a high power CO_2 laser, and in order to achieve high temperatures ($\approx$ 1000 °C), their absorptivity for the wavelength of the CO_2 laser (λ = 10.6 μm) was increased by patterning plasmonic gratings[11]. These gratings were patterned on the back of the substrate, opposite to the side where the diamond is grown (see Fig.1).

The heating efficiency of refractory microstructures by excitation of SPP in the far infrared (λ = 10.6 μm) is studied in this chapter. More specifically, the dependence of the maximum achievable temperature with the period and filling factor (FF) of the structure will be investigated.

3.1.2 Light coupling by plasmonic gratings

SPP are collective electron oscillations propagating in the interface between a metal and a dielectric. They are caused by the coupling of electromagnetic radiation (light) to the free electrons of the metal[12].θ

In order to create a SPP at an interface, it is necessary to match the in-plane momentum $k_x=|k|\cdot sin\theta$ of the incoming photons and the propagation constant of the SPP at the interface β. There are a variety of strategies to achieve this, but in this case the grating coupling method was the selected option. This method involves structuring or patterning the metal with periodic grooves[13,14]. Other alternatives for light coupling, like prism or nanoparticle coupling, were not adequate for the experimental conditions of the thermionic emission tests.

A patterned structure can achieve momentum matching when the following condition is fulfilled:

$$\beta = \overrightarrow{k_x} = |\vec{k}| \cdot sin\theta \pm vg \qquad (3.1)$$

where $g = 2\pi/a$ is the reciprocal vector of the grating, $v = 1,2,3,...$, a is the periodicity of the structure on the interface, $\vec{k}$ is the incident wave vector and $\overrightarrow{k_x}$ is the in-plane propagation wave vector [11]. In essence, when light with a wavelength λ is to be coupled by the grating method to an interface to excite a SPP, a structure needs to be patterned on the surface with a period $a \approx \lambda$ with $a < \lambda$.

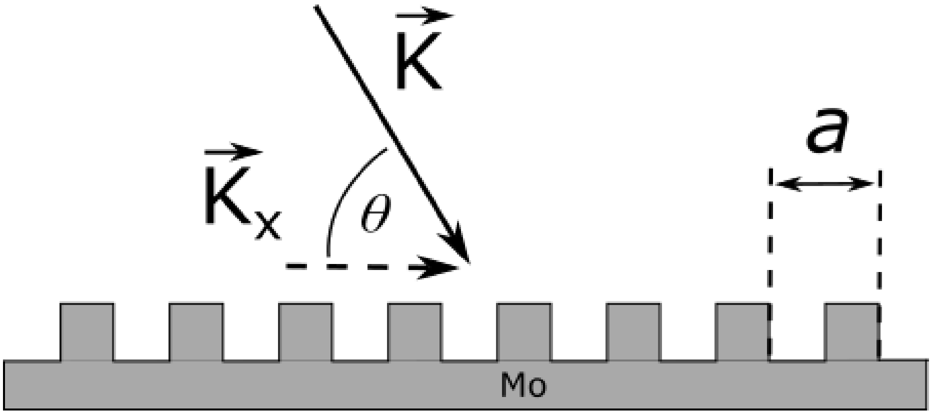

Figure 2: Diagram of momentum matching of light and SPP with the grating technique. *K* is the total momentum of the incident photons and k_x is the x or component or momentum component parallel to the interface between metal and dielectric, while *a* is the period of the patterned structure or grating.

In our case, the condition of Eq.1 is fulfilled when $a \approx 10.6$ µm. Once the coupling conditions are satisfied, the incoming light is trapped on the interface between metal and air (or vacuum), enhancing the interaction of light with the Mo substrate.

3.2 Sample characterisation

3.2.1 Morphology of molybdenum gratings

A series of linear gratings have been produced in molybdenum to study the effects of the plasmon coupling conditions. The parameters studied were the period or pitch and the filling factor (FF) of the structure. FF is the ratio between the filled space and the unfilled space of the periodic structure as it is depicted in Fig.3 (Right) and expressed in Eq.1.

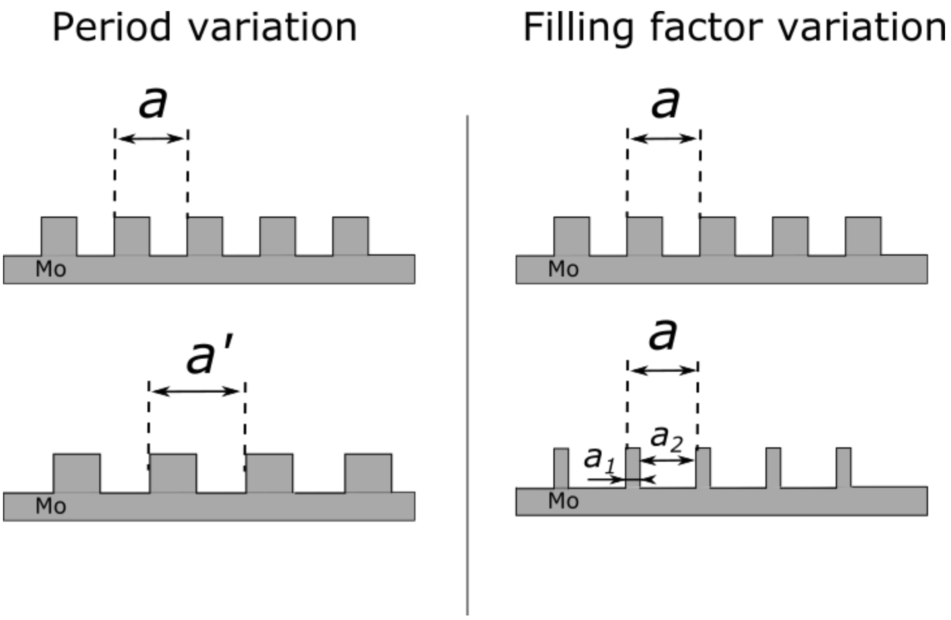

Figure 3: Representation of the two grating parameters studied in this chapter. (Left): Variation of the period or pitch of the structure. (Right): Variation of the filling factor.

$$FF = \frac{a_1}{a_2} \cdot 100 \qquad (3.2)$$

Two batches of samples were produced: the first batch had a fixed *FF*=80% while the period of the structure was changed from 10.3 µm to 10.6 µm. For the second batch, the period was fixed at 10 µm and the *FF* was changed from 20% to 80% (see Ch.2 sect 2.8.1).

Fig.4 shows optical microscope images of the surface of bare unpatterned Mo (a) and three different preliminary grating couplers with; a 10.6 µm pitch (b), 15.0 µm pitch (c) and 20.0 µm pitch (d). All of them show the same groove geometry with slight local differences due to the surface roughness of the bare molybdenum substrates.

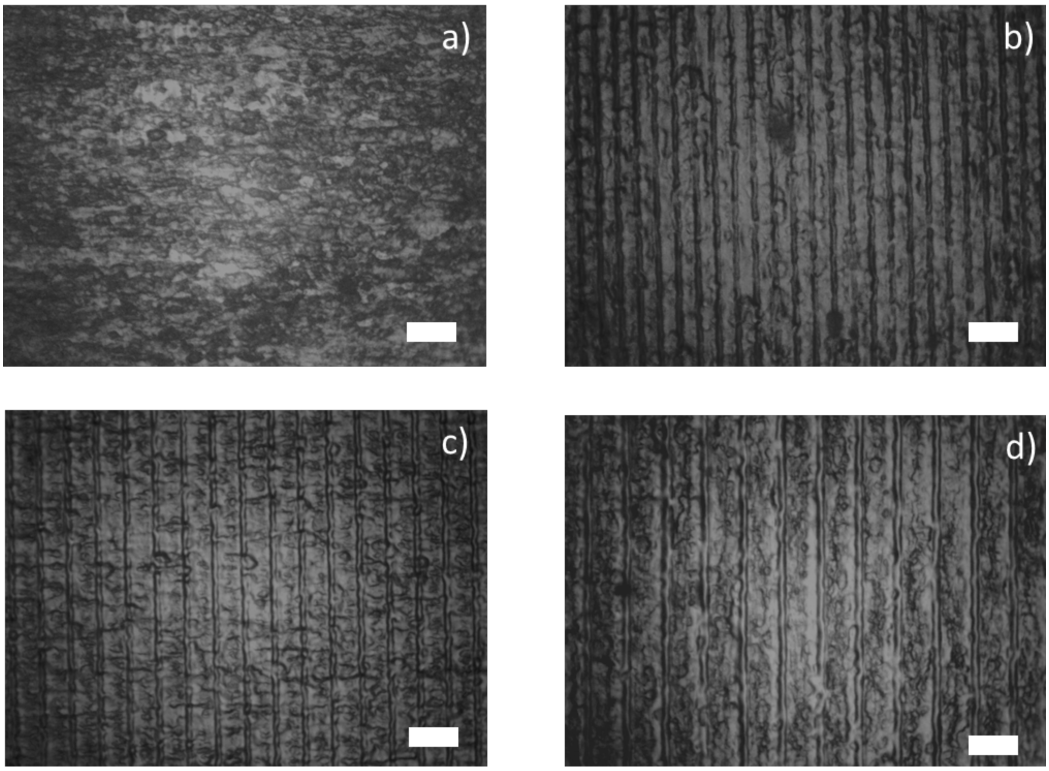

Figure 4: Optical microscope images of gratings patterned on Mo substrates with FF=80 for different periods: a) Bare Mo substrate and laser-structured samples with periods of: b) 10.6 μm, c) 15.0 μm and d) 20.0 μm. Objective magnification 50x. Scale bar 25 μm.

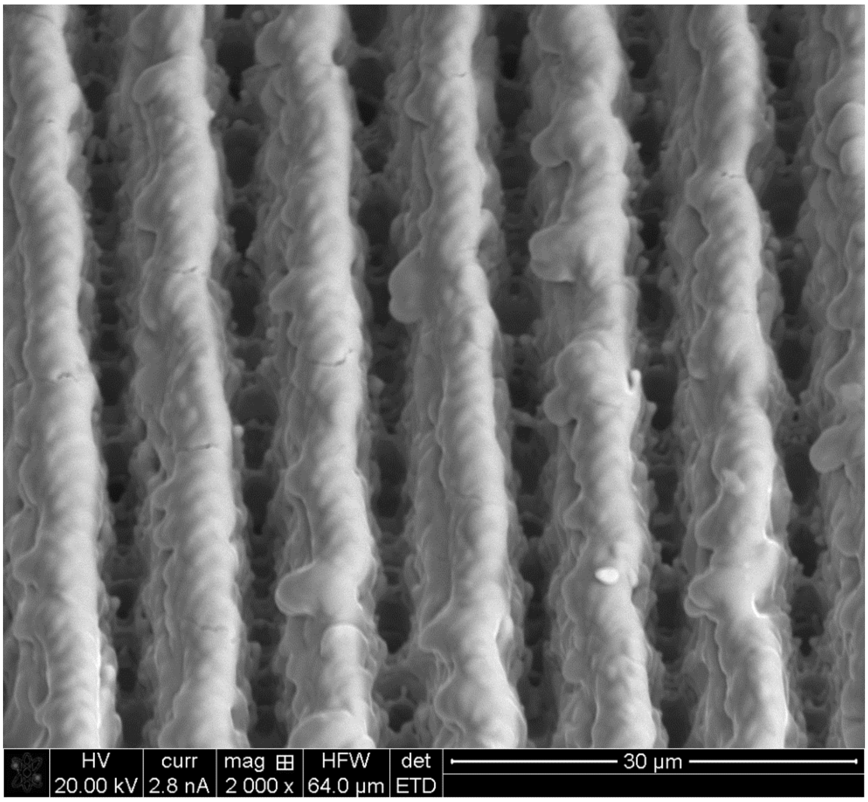

Figure 5: SEM image of a plasmonic grating patterned on a Mo substrate Period= 10.6 μm , FF=20%.

The morphology of the samples will be the convolution of the engraved pattern and the intrinsic surface morphology of the molybdenum substrate. This adds some randomness to the samples but the effect is constant across all samples and shouldn't hinder the analysis of the laser coupling.

Fig.5 shows a high-magnification SEM image of a plasmonic grating on a Mo substrate with a FF=20% and a period of 10.6 µm. As it can be seen, the structure of the grating is periodic even though the surface of the gratings is not uniform due to the fabrication process. Ultimately, this could lead to increased absorption due to light scattering.

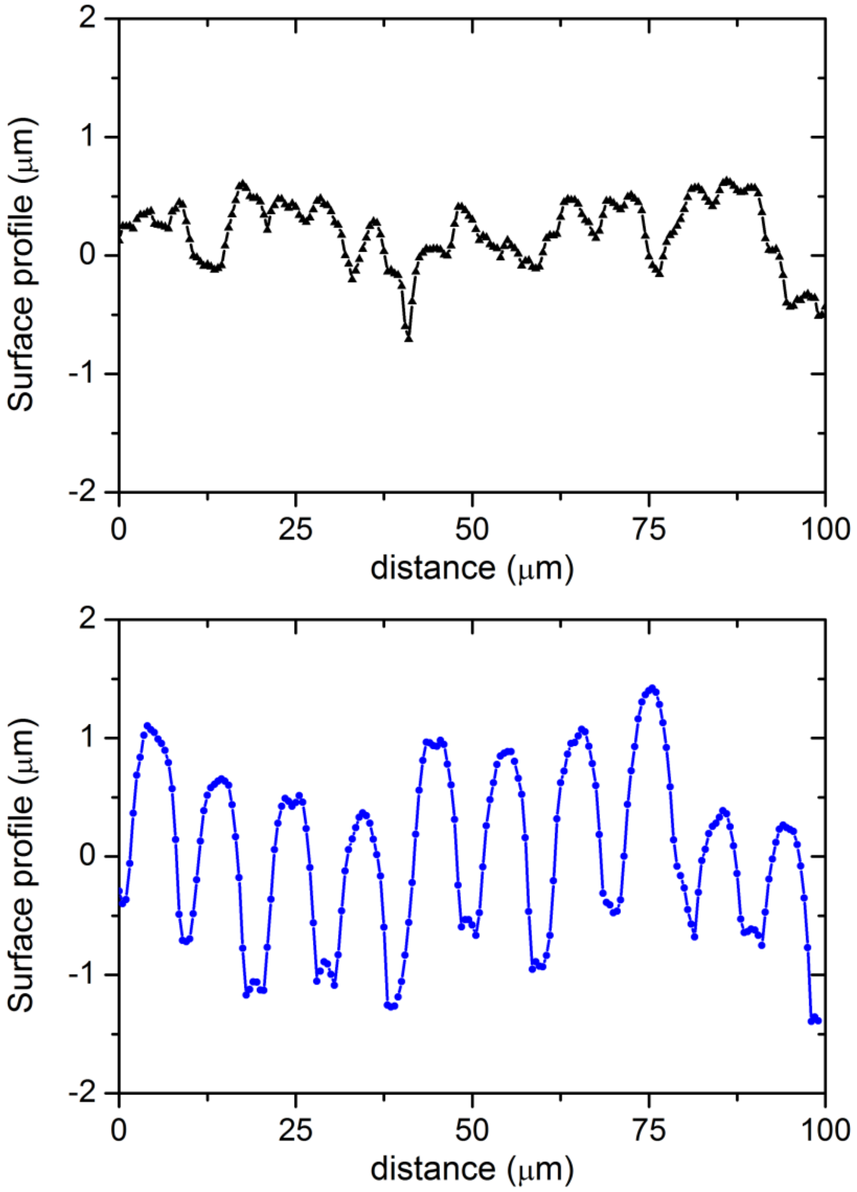

Figure 6: Surface profilometry data of the bare Mo substrate (Top) and of the plasmonic grating structures (Bottom).

Surface profile measurements were performed on the bare Mo substrate and on the Mo gratings to characterise the roughness of the bare Mo and the depth of the grooves of the gratings. The peak to valley roughness of the bare Mo substrate is ≈ 1 µm (see Fig.6). Conversely, the depth of the grooves on the gratings was found to change depending on the width or FF of the grating due to the laser fabrication method. The depths of the grooves range from ≈ 2 µm to ≈ 5 µm.

3.2.2 Simulations of molybdenum gratings: effect of period and filling factor

Simulations of the optical response of the plasmonic gratings on Mo were carried out by finite element analysis to confirm the values of the design parameters of the gratings. The effects of different periods and different FF were studied.

The first series of simulations were concerned with the effect of changing the period on the plasmonic structure while keeping the FF and the depth of the grooves constant. Fig.7 shows the reflectance plots for polarised light perpendicular to the gratings at normal incidence for gratings for a range of periods between 10 µm and 11 µm. The depth of the grooves and the groove width are kept constant at 1 µm and 5 µm, respectively.

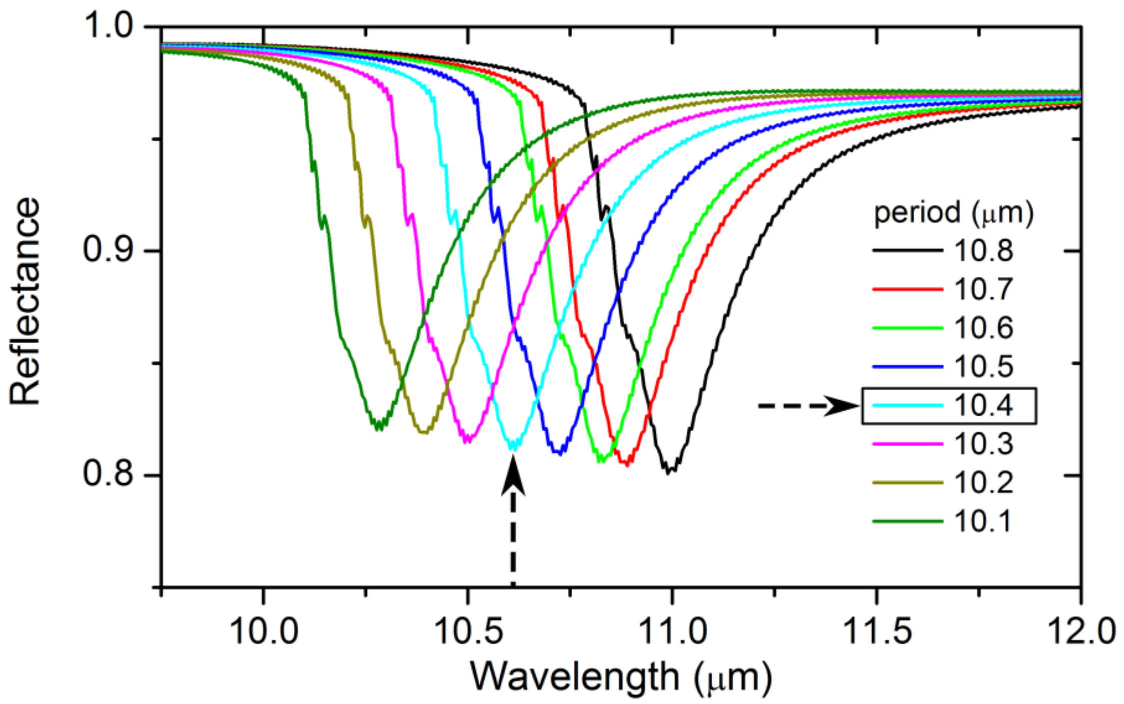

Figure 7: Simulation of reflectance *vs* wavelength plots at normal incidence for polarised light perpendicular to the plasmonic grating for gratings with different periods. All gratings have a depth of 1 µm and a groove width of 5 µm. Note how the absorption peak changes as the period of the grating is changed. Vertical black arrow shows the position of λ = 10.6 µm and the horizontal arrow indicates the optimum theoretical grating period. c

It can be seen on Fig.7 that the period of the grating has a strong influence on the reflectance peak. As the period of the structure increases the peak of the reflectance increases accordingly almost by the same magnitude. According to the simulation and taking into account that the wavelength of the laser to be coupled to these gratings is 10.6 µm, the optimum grating period seems to be ≈ 10.4 µm. This is in agreement with the plasmonic theory explained in sect 3.1.2.

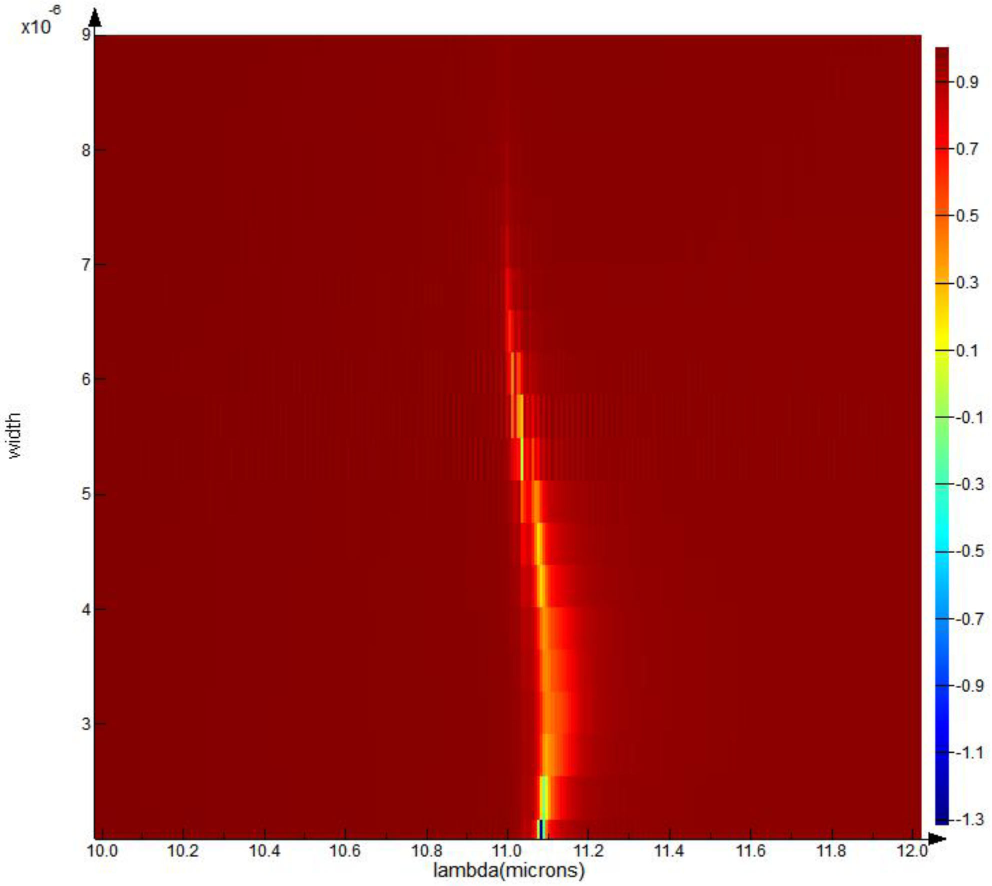

Figure 8: Change of the reflectance with the variation of the groove width on the grating. The simulation is done for normal incidence with the linear polarisation of the laser perpendicular to the plasmonic grating. The vertical axis represents the width of the grooves on the grating, the horizontal axis is the wavelength and the colour scale bar is the reflectance. The period of the grating was kept constant at 11 µm while the depth of the groove was kept at 0.5 µm. The width of the groove is varied between 2 and 9 µm. Simulation provided by collaborator Sara Nuñez Sanchez.

Conversely, Fig.8 represents the change of the reflectance peak with the variation of the FF. The vertical axis represents the width of the grooves on the grating, the horizontal axis is the wavelength and the colour scale bar is the reflectance. The period of the grating was maintained constant at a value of 11 µm, the depth of the groove was kept at 0.5 µm and the width of the grooves was varied between 2 to 9 µm.

The plot shows how the reflectance peaks are affected by changes on the width of the grooves. Increasing the width initially shifts the resonance wavelength towards higher values. But shortly after reaching a value of 4 µm, the resonance wavelength returns to its original value, which suggests that increasing the width of the groove too much seems to degrade the effect of the grating. This is manifested by the uniform high reflectance across the whole range of wavelengths. This means that the light is not absorbed anymore and the effect of the grating has ceased to function. Therefore, in principle the best design for a grating should be one with a FF of 50% or higher.

3.3 Theoretical thermal analysis: equilibrium equation

The thermal system that is being considered here is a 10 × 10 mm square Mo foil with a thickness of 0.25 mm. The only energy input to the system is the laser focused on the patterned side of the foil. Conversely, there is heat loss *via* radiation through all the surfaces of the foil and heat loss *via* conduction through the parts of the foil in contact with the sample holder. The experiments are carried out under high vacuum condition (see Ch.2 sect.2.1.1), so there is no heat loss due to convection.

Once the illumination of the laser is activated, a steady state is eventually reached. From that point on the energy balance of the system can be expressed by the following equation:

$$P_{laser} = R \cdot P_{laser} + P_{rad} + P_{cond} \qquad (3.3)$$

where P_{laser} is the power of the incident laser, R is the reflectivity of the patterned side of the foil for the wavelength of the laser (λ = 10.6 µm), P_{rad} is the radiation heat loss and P_{cond} is the conduction heat loss (see Fig.9).

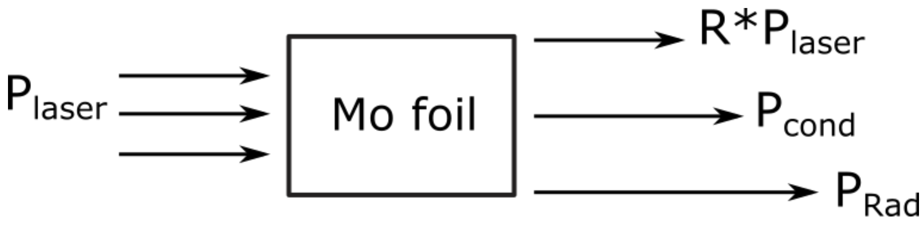

Figure 9: Diagram of the different heat fluxes on the Mo substrate thermal system. P_{laser} is the power of the incoming laser, R is the reflectivity on the grating side for the wavelength of the laser, P_{cond} is the heat loss due to conduction losses and P_{rad} is the heat loss due to radiation losses.

The heat loss due to radiation can be expressed by:

$$P_{rad} = \varepsilon_{Mo}\sigma A(T^4 - T_C^4) \qquad (3.4)$$

where $\varepsilon \approx 0.1$ is the total hemispherical emissivity of the Mo, $\sigma = 5.670367 \times 10^{-8}$ is the Stephan-Boltzmann constant, $A = 2 \times 10^{-4}$ m^2 is the radiation area of the foil, T is the steady state temperature of the foil in Kelvin and $T_c = 300$ K is the temperature of the surroundings, which in this case is the wall of the vacuum chamber (see Ch.2 sect.2.1.1).

The emissivity of the Mo is dependent on the surface oxidation[16] and the temperature[17] as well as roughness. In our case the surface is very lightly oxidised and the emissivity can be calculated by the formula proposed by Paradis *et al*[18]. The values of emissivity *vs* temperature according to this formula are plotted in Fig.10. If we take into consideration that radiation is not relevant at low temperatures (T < 350°C), it is possible to fix the emissivity at a value of $\varepsilon \approx 0.1$ taking into account the range of temperatures that were reached during the thermionic emission experiments.

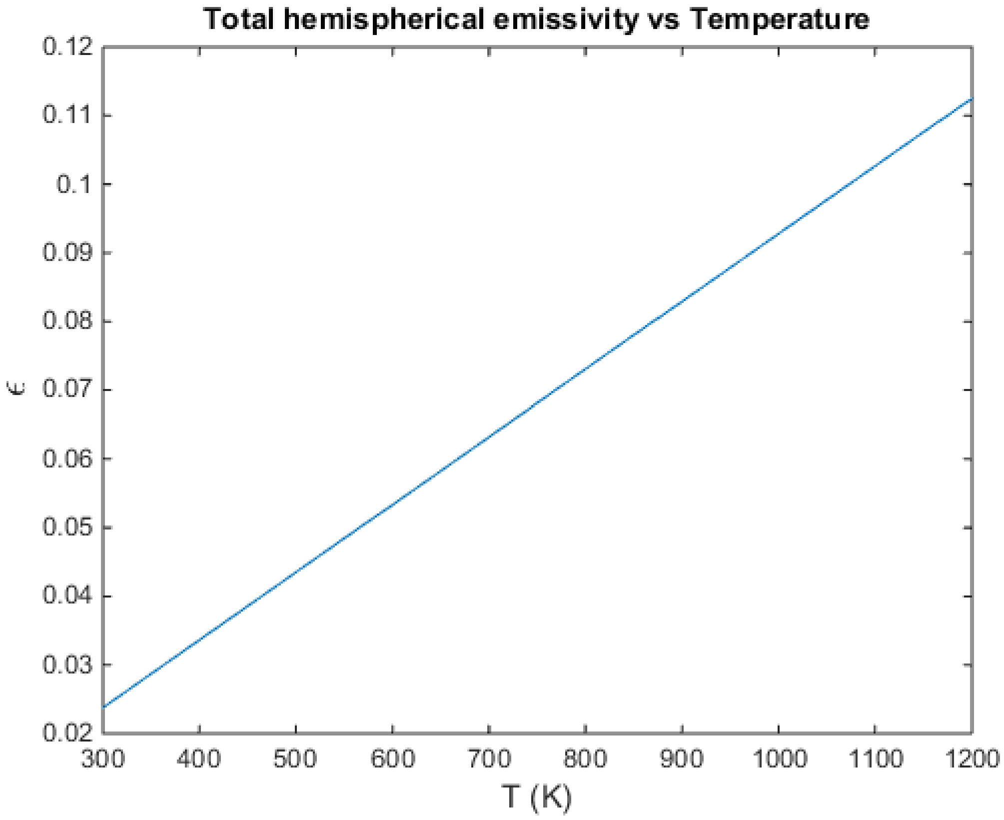

Figure 10: Plot of the total hemispherical emissivity ε versus temperature T. According to the formula by Paradis *et al*[18].

Heat loss by conduction happens through the quartz sample holder where the sample rests. Hence, it is possible to model this heat loss as a heat flux through a "uniform wall" with a known thermal conductivity and a certain contact surface area between the foil and the quartz sample holder. Therefore, the heat loss due to conduction is given by[19]:

$$P_{cond} = \frac{\kappa_{Quartz} A_c (T - T_{cold})}{t} \qquad (3.5)$$

where $k_{\text{quartz}} \approx 1.5$ W/mK [20] is the thermal conductivity of the quartz holder, $A_c \approx 4.96 \times 10^{-6}$ m^2 is the contact area between the Mo foil and the sample holder, T is the temperature of the Mo foil, $T_{\text{cold}} = 300$ K is the temperature at the other side of the wall (in this case at the other side of the quartz substrate) and $t \approx 1.5 \times 10^{-2}$ m is the thickness of the quartz substrate.

If we replace the terms of Eq.3.4 and Eq.3.5 in Eq.3.3, rearrange the terms and take into account that $A_{\text{abs}} = 1\text{-}R$, we obtain:

$$P_{laser}(T) = \frac{2\varepsilon\sigma A}{A_{abs}} T^4 + \frac{\kappa_{Quartz}\, A_c}{A_{abs}\, t} T - \left(\frac{2\varepsilon\sigma A}{A_{abs}} {T_C}^4 + \frac{\kappa_{Quartz}\, A}{A_{abs}\, t} T_{cold} \right) \qquad (3.6)$$

which we can simplify to:

$$P_{laser}(T) = C_4 T^4 + C_1 T - C_o \qquad (3.7)$$

where:

$$C_4 = \frac{2\varepsilon\sigma A}{A_{abs}} \ , \ C_1 = \frac{\kappa_{Quartz}\, A_c}{A_{abs}\, t} \ , \ C_0 = \left(\frac{2\varepsilon\sigma A}{A_{abs}} {T_C}^4 + \frac{\kappa_{Quartz}\, A}{A_{abs}\, t} T_{cold} \right) \qquad (3.8)$$

The coefficient C_4 in Eq.3.8 represents the contribution of radiation to the heat loss while C_1 represents the same for conduction heat loss. However, both of them are influenced by the absorbance of the grating A_{abs}, as the other parameters are constant. Therefore, if the coupling conditions of the grating to the incoming radiation are improved, A_{abs} should increase, causing a reduction of C_4 and C_0.

Fitting Eq.3.6 to the plots of T *vs* laser power for different samples and examining the values of C_4 and C_1 should provide an indication of the variation on A_{abs} due to the different grating coupling conditions.

3.4 Heating experiments

3.4.1 Polarisation dependence

The laser used for the heating experiments is linearly polarised and in order to couple to the plasmonic grating the polarisation needs to be perpendicular to the grooves of the grating because otherwise the incident light won't be able to couple to the plasmon[11]. Therefore, in order to determine the presence of plasmon coupling due to the grating on the Mo substrates, a grating with a period of 10.6 μm and a FF of 80% was tested with the laser polarisation parallel and perpendicular to the grooves.

The experiments in this and the following sections have been performed using the TECsim instrument (see Ch.2 -Sect.2.1).

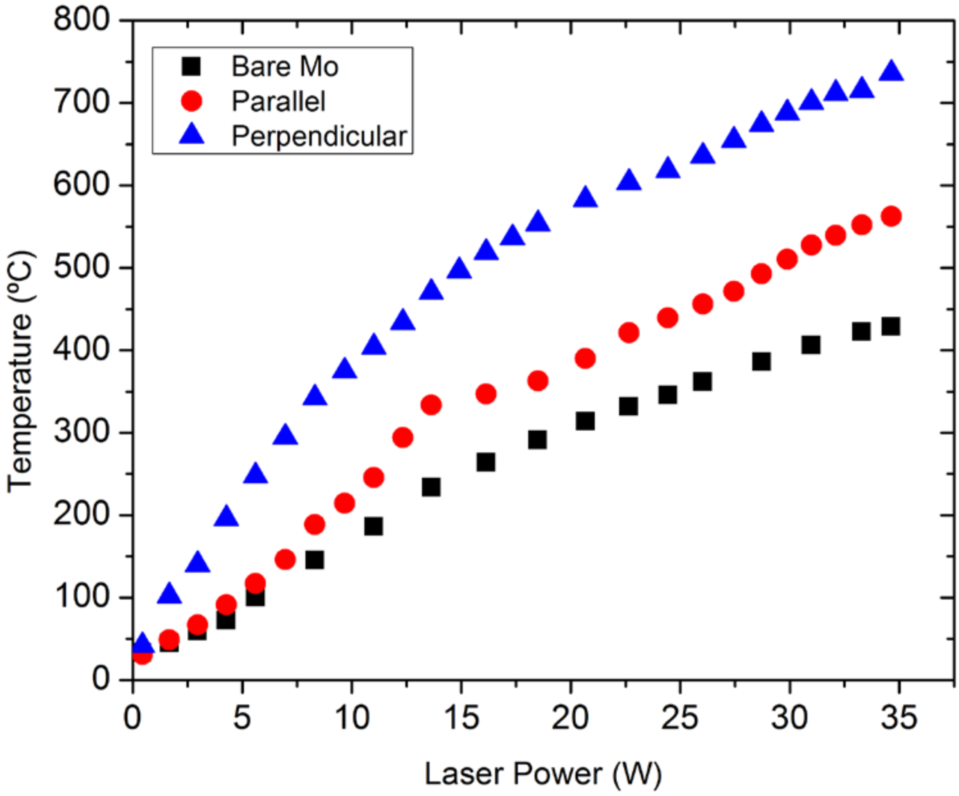

Figure 11: Steady state temperature *vs* laser power plot of a Mo substrate with a FF=80% and a period of 10.6 μm. The sample was tested with the laser polarisation parallel to the grating (red circles) and perpendicular to it (blue triangles). The black squares are the temperatures for a bare Mo substrate included as a reference. The error in the temperature axis (Y axis) is 2°C for T < 527°C and 2.5 × 10^{-3} × T for T > 527°C. Which at the maximum temperature of this plot is 2.4°C.

The experiments of this and the following sections were carried out using the following method: the samples were introduced on the TECsim under high vacuum conditions. Then they were illuminated with a linearly polarised high power laser (λ = 10.6 μm) with the polarisation perpendicular (or parallel, just in this case) to the gratings at a fixed power until the steady state regime was reached. It was then when the temperature was recorded, right before increasing the laser power to achieve the next testing temperature. The laser power used ranged from 0 W to 35 W.

Fig.11 shows the steady state temperature *vs* laser power plot for the sample described above. It confirms the presence of a clear difference between the parallel and perpendicular test, which is consequence of increased absorbance caused by the plasmon coupling on the grating.

The increase of temperature for the parallel test in comparison with the bare Mo might be caused by the scattering of light inside the grooves (see Fig.5) and a potential misalignment of the grating with respect to the laser polarisation.

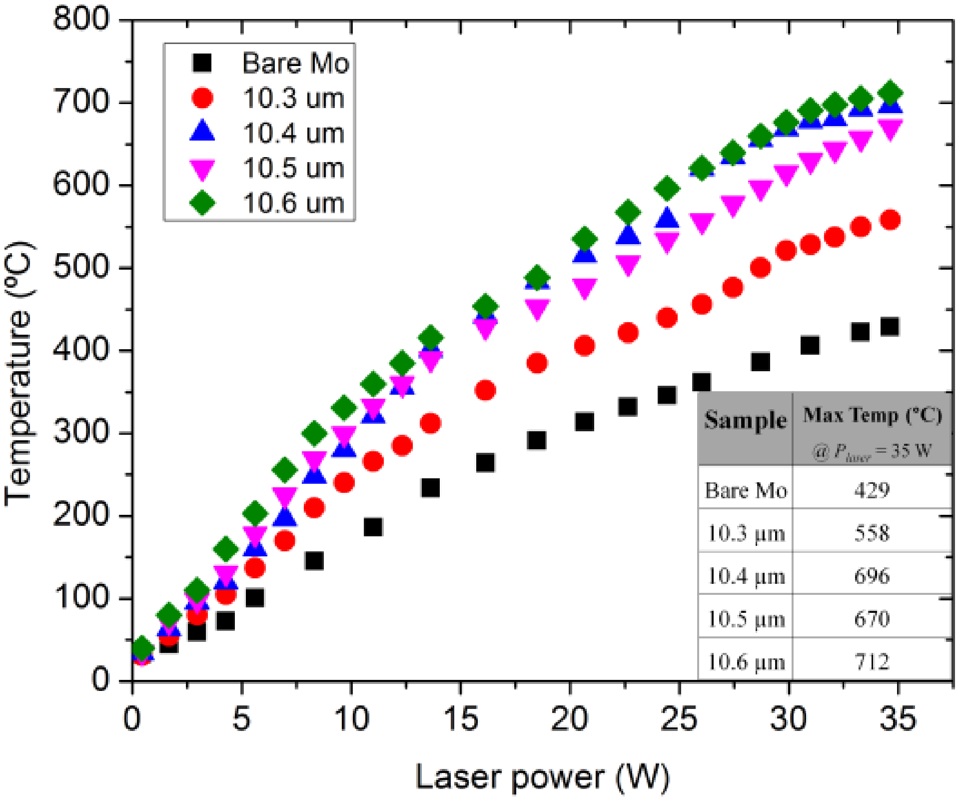

Sample	Max Temp (°C) @ P_{laser} = 35 W
Bare Mo	429
10.3 μm	558
10.4 μm	696
10.5 μm	670
10.6 μm	712

Figure 12: Steady state temperature *vs* laser power of Mo substrates with different grating periods and a FF=80%. (Insert): Maximum steady state temperature achieved at maximum laser power P_{laser}= 35W. The error in the temperature axis (Y axis) is 2°C for T < 527°C and 2.5 × 10^{-3} × T for T > 527°C. Which at the maximum temperature of this plot is 2.4°C.

3.4.2 Period variation

The effect of the period of the plasmonic grating on the maximum temperature achieved by the patterned Mo substrate is studied in this section. Gratings patterned with periods ranging from 10.3 µm to 10.6 µm and a fixed FF = 80% have been tested on the TECsim instrument (see Ch.2 - Sect.2.1).

The steady state temperatures *vs* laser power of Mo substrates with gratings of different periods and that of a bare Mo substrate are plotted on Fig.12. All Mo gratings cause an increase of the steady state temperature when compared to the bare Mo substrate.

The temperature of all samples seems to follow the same trend. The sample that achieves the highest temperature $T \approx 712$ °C while at the maximum laser power is that with a grating period of 10.6 µm. The sample with a period of 10.4 µm, however, reaches an already satisfactory temperature, very close to that achieved by the sample with a period of 10.6 µm. This agrees with the results of the simulation presented in Sect 3.3.2.

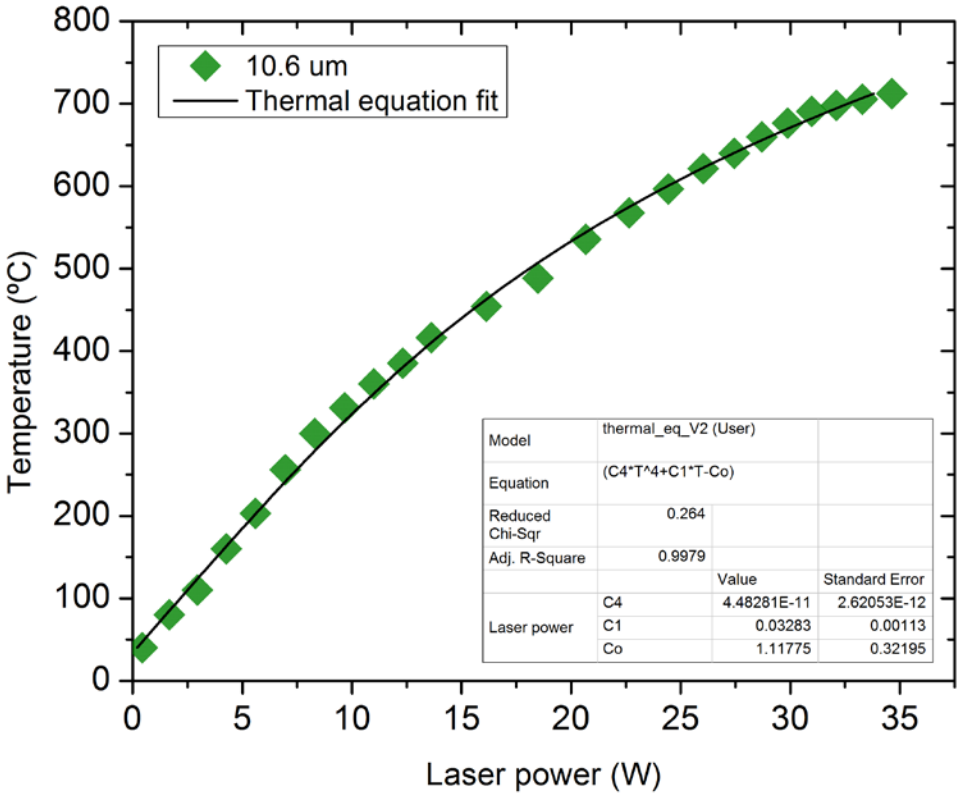

Figure 13: Temperature *vs* laser power plot of a Mo substrate for a grating with period of 10.6 µm and FF=80% (green diamonds). Fit of thermal balance equation (Eq.6) to the data (black solid line). The error in the temperature axis (Y axis) is 2°C for T < 527°C and 2.5 × 10^{-3} × T for T > 527°C. Which at the maximum temperature of this plot is 2.43°C.

The steady state temperature *vs* laser power for a Mo substrate with a grating period of 10.6 µm and FF=80% together with the fit of the thermal balance equation (Eq.3.6) to this data is plotted in Fig.13. As it can be seen in this figure, Eq.3.6 reproduces well the behaviour of the temperature with the variation of laser power.

The temperature set of data plotted in Fig.13 seems to have two regimes. The first regime occurs at low powers below $P_{\text{laser}} \approx 10$ - 12 W during which temperature follows a linear trend. However, temperature has an exponential decay trend when in the second regime, which ranges from $P_{\text{laser}} \approx$ 10 - 12 W up to $P_{\text{laser}} \approx 35$ W. These regimes are a consequence of the dominant heat transfer mechanism at different temperatures.

At low P_{laser} and temperature the main heat loss mechanism is conduction, that is governed by Eq.5. In this case, the relation between P_{laser} and T in Eq.3.6 is dominated by the second term C_1, which is linear. Furthermore, as the P_{laser} and temperature increase radiation becomes relevant as a heat loss mechanism and the first term of Eq.3.6, C_4 starts dominating. Causing a change on the temperature trend due to the radiation heat loss that tends to a saturation point.

The coefficients C_4 and C_1 of Eq.3.6 obtained from the fitting of the data represented in Fig.12 are plotted in Fig.14. The theoretical interval of values for the coefficients are $C_4 \approx [1.134 \times 10^{-12}, 1.134 \times 10^{-10}]$ and $C_1 \approx [0.0297, 2.976]$. These values are obtained under the assumption that $A_{\text{abs}} = [0.01, 1]$ while the other parameters remain constant as they are known. When comparing the theoretical intervals with the values obtained in the fittings; both C_4 and C_1 are in excellent agreement as all values are within the theoretical interval.

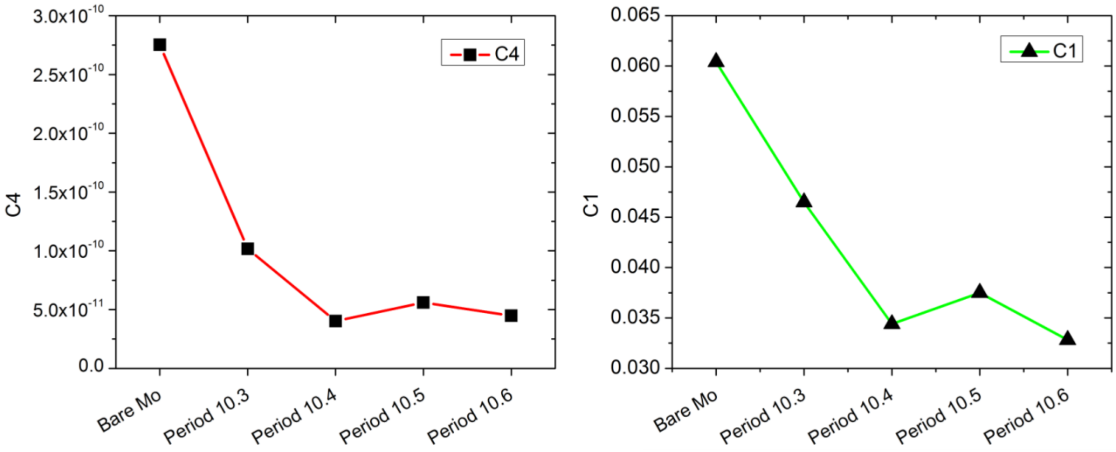

Figure 14: Values of the coefficients C_4 and C_1 of Eq.6 obtained from the fitting of the Eq.6 to the data shown in Fig.12. The error for C_4 in Bare Mo is 1.71×10^{-11} and decreases to 2.62×10^{-12} for the period 10.6 µm. The error for C_1 in Bare Mo is 1.43×10^{-3} and decreases to 1.13×10^{-3} for the period 10.6 µm.

Both coefficients plotted in Fig.14 show the same trend as their values decrease as the period of the gratings increases. This decrease is caused by the rise of the absorbance A_{abs} of the plasmonic grating. As shown on the equation bellow, an increase on A_{abs} will cause C_4 and C_1 to decrease.

$$C_4 = \frac{2\varepsilon\sigma A}{A_{abs}} \quad , \quad C_1 = \frac{\kappa_{Quartz}\, A_c}{A_{abs}\, t} \qquad (3.9)$$

3.4.3 Filling factor variation

The effect of the FF of the plasmonic grating on the maximum temperature achieved by the patterned Mo substrate is studied in this section. Gratings patterned with FF of 20%, 50% and 80% and a fixed period of 10.6 µm have been tested on the TECsim instrument (see Ch.2 sect 2.1)

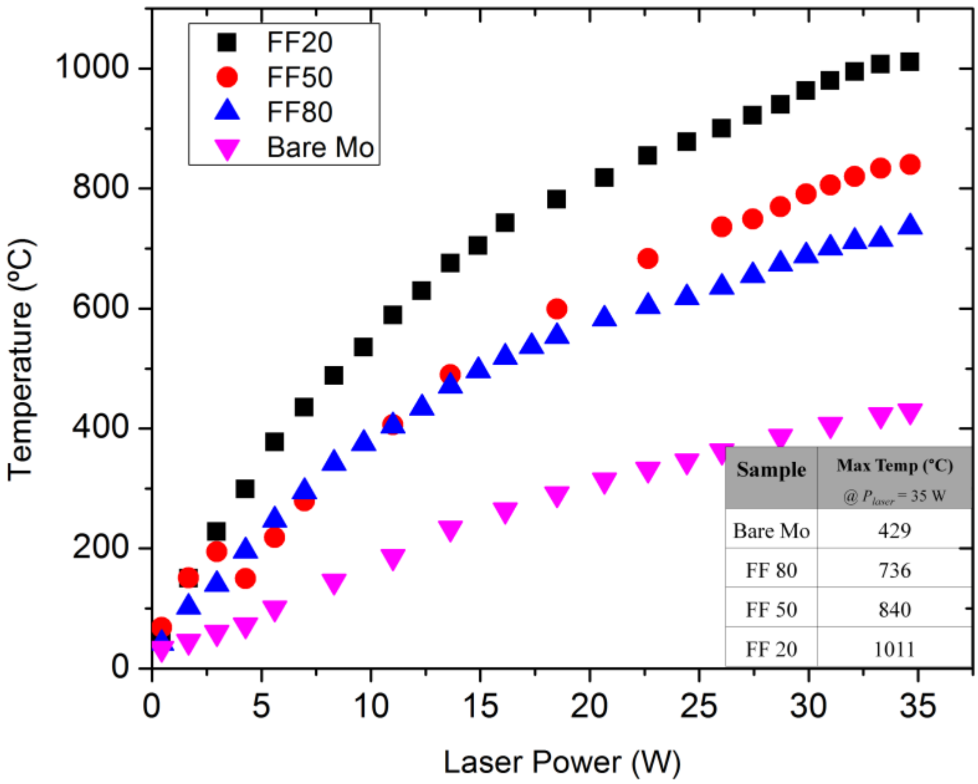

Sample	Max Temp (°C) @ P_{laser} = 35 W
Bare Mo	429
FF 80	736
FF 50	840
FF 20	1011

Figure 15: Steady state temperature *vs* laser power of Mo substrates with different FF and a period of 10.6 µm. (Insert): Maximum steady state temperature achieved at maximum laser power P_{laser}= 35W. The error in the temperature axis (Y axis) is 2°C for T < 527°C and 2.5 × 10^{-3} × T for T > 527°C. Which at the maximum temperature of this plot is 3.18°C.

Fig.15 shows the plot of the steady state temperatures of Mo substrates with different FF *vs* laser power. The first thing that stands out is the fact that decreasing the FF increases the maximum temperature at $P_{\text{laser}} = 35$ W. In principle this contradicts the results of the simulation shown in Fig.8 that predicts that decreasing the FF to low values would decrease the absorbance.

This discrepancy is explained by the different depths of the grooves of the gratings across samples consequence of the fabrication method, as already mentioned in sect.3.3.1. Because of this, the experimental results are not directly comparable with the simulation. Furthermore, the irregular or textured surface of the grooves (Fig.5) significantly increases the scattering inside the grooves, which in turn increases the effective absorbance of the grating as the grooves are made wider. But this is not taken into account in the simulation as it assumes a groove with an ideal smooth surface.

The temperature optimisation at 35 W was achieved when reducing the FF to 20% with a period of 10.6 µm, which seems to generate the best results. Moreover, qualitatively, the data on Fig.15 are analogous to those of Fig.12. Two different regimes can be identified in both sets of data. One at low temperatures at which conduction heat loss dominates and the second, that occurs at higher temperatures and is dominated by radiation heat loss.

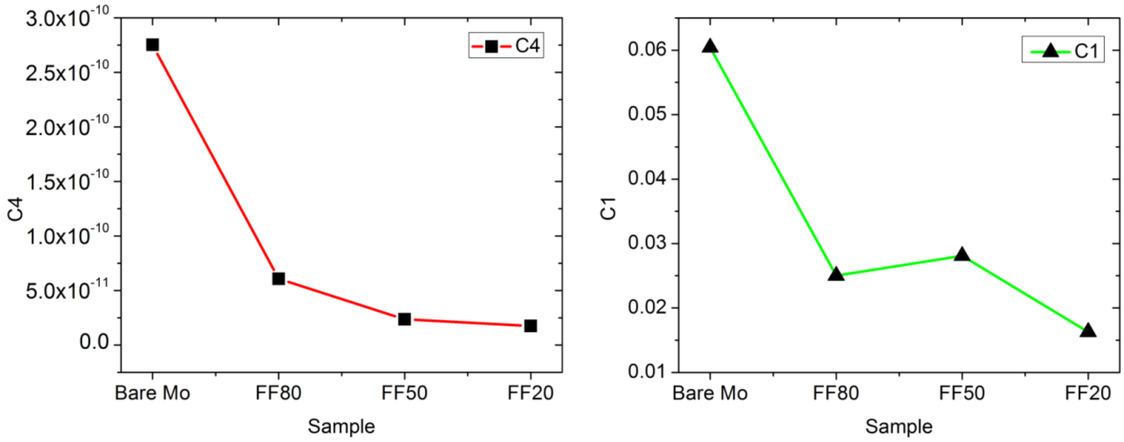

Figure 16: Values of the coefficients C_4 and C_1 of Eq.6 obtained from the fitting of the Eq.6 to the data shown in Fig.15. The error for C_4 in Bare Mo is 1.71×10^{-11} and decreases to 4.3×10^{-13} for the FF20. The error for C_1 in Bare Mo is 1.43×10^{-3} and decreases to 5.58×10^{-4} for the FF20.

The thermal balance equation (Eq.6) was fitted to the data in Fig.15, to extract the parameters C_4 and C_1 shown in Fig.16. As discussed in the previous section, the theoretical interval of values for the coefficients are $C_4 \approx [1.134 \times 10^{-12}, 1.134 \times 10^{-10}]$ and $C_1 \approx [0.0297, 2.976]$. So, when comparing the coefficients of Fig.16 with the theoretical interval values, C_4 is again in excellent agreement with the interval. Even though C_1 goes a bit lower than the lower theoretical range, it largely agrees with the values of the theoretical range.

The trend of both coefficients is similar to the one described in the previous section and it can also be explained by an increase in the absorbance of the grating. However, in this case the increase in absorbance is caused by the decline of FF.

3.5 Conclusions

In this chapter, plasmonic gratings on Mo substrates with different periods and FF have been tested by performing laser assisted plasmonic heating tests. According to the presented data, the maximum temperature is achieved on a configuration where the period of the grating is 10.6 µm and the FF = 20%. This will be the configuration selected to be used on future experiments for thermionic emission tests. The maximum recorded temperature was T = 1011 °C. Which was the target temperature that was sought for the thermionic experiments.

Plasmonic coupling is the main light absorption mechanism. But it was also found that scattering plays a significant role on the light absorption process, as it considerably contributes to the total absorption.

The plots of T *vs* laser power show two different regimes. One occurs at low temperatures where T follows a linear trend and the dominant heat loss mechanism is conduction. Conversely, at medium or high temperatures, radiation dominates as a mechanism of heat loss and the data follows an exponential decay trend.

This heating method can be used for applications that require a fine a quick control of temperatures over an extensive temperature range like thermal programmed desorption[21,22] or thermal assisted catalysis[1].

Acronyms

SPP: Surface Plasmon Polariton

FF: Filling Factor

FTIR: Fourier Transform Infrared Spectroscopy

List of figures

References

1. Adleman, J. R., Boyd, D. A., Goodwin, D. G. & Psaltis, D. Heterogenous catalysis mediated by plasmon heating. *Nano Letters* **9,** 4417–4423 (2009).

2. Link, S. & El-Sayed, M. A. Shape and size dependence of radiative, non-radiative and photothermal properties of gold nanocrystals. *International Reviews in Physical Chemistry* **19,** 409–453 (2000).

3. Brongersma, M. L., Halas, N. J. & Nordlander, P. Plasmon-induced hot carrier science and technology. *Nature Nanotechnology* **10,** 25–34 (2015).

4. Belton, D. N. & Schmieg, S. J. Effects of oxygen on diamond growth using platinum substrates. *Journal of Applied Physics* **69,** 3032–3036 (1991).

5. Saito, Y., Sato, K., Matuda, S. & Koinuma, H. Effects of substrate material on diamond growth from CO-H2 plasma. *Journal of Materials Science* **26,** 2441–2444 (1991).

6. West, P. R. *et al.* Searching for better plasmonic materials. *Laser & Photonics Reviews* **4,** 795–808 (2010).

7. Buijnsters, J. G., Shankar, P., van Enckevort, W. J. P., Schermer, J. J. & ter Meulen, J. J. Adhesion analysis of polycrystalline diamond films on molybdenum by means of scratch, indentation and sand abrasion testing. *Thin Solid Films* **474,** 186–196 (2005).

8. Ramesham, R., Rose, M. F. & Askew, R. F. Growth of chemical vapour deposition diamond on large molybdenum cylinders for crossed-field amplifier applications. *Journal of Materials Science Letters* **15,** 2173–2176 (1996).

9. Guler, U., Boltasseva, A. & Shalaev, V. M. Refractory Plasmonics. *Science* **344,** 263–264 (2014).

10. Naik, G. V., Shalaev, V. M. & Boltasseva, A. Alternative Plasmonic Materials: Beyond Gold and Silver. *Advanced Materials* **25,** 3264–3294 (2013).

11. Maier, S. A. *Plasmonics: Fundamentals and Applications*. **1,** (Springer US, 2007).

12. Barnes, W. L., Dereux, A. & Ebbesen, T. W. Surface plasmon subwavelength optics. *Nature* **424,** 824–830 (2003).

13. Ferry, V. E., Sweatlock, L. A., Pacifici, D. & Atwater, H. A. Plasmonic Nanostructure Design for Efficient Light Coupling into Solar Cells. *Nano Letters* **8,** 4391–4397 (2008).

14. Pala, R. A., White, J., Barnard, E., Liu, J. & Brongersma, M. L. Design of Plasmonic Thin-Film Solar Cells with Broadband Absorption Enhancements. *Advanced Materials* **21,** 3504–3509 (2009).

15. Kuzma, A. *et al.* Influence of surface oxidation on plasmon resonance in monolayer of gold and silver nanoparticles. *Journal of Applied Physics* **112,** (2012).

16. Wade, W. *Measurements of total hemispherical emissivity of various oxidized metals at high temperature*. (1958).

17. Matsumoto, T., Cezairliyan, A. & Basak, D. Hemispherical Total Emissivity of Niobium, Molybdenum, and Tungsten at High Temperatures Using a Combined Transient and Brief Steady-State Technique. *International Journal of Thermophysics* **20,** 943–952 (1999).

18. Paradis, P.-F. & Rhim, W.-K. Non-contact measurements of thermophysical properties of titanium at high temperature. *The Journal of Chemical Thermodynamics* **32,** 123–133 (2000).

19. Hugh D. Young, Freedman A., R. & Ford, A. L. *University physics with modern physics*. (Addison-Wesley, 2013).

20. Abdulagatov, I. . *et al.* Thermal conductivity of fused quartz and quartz ceramic at high temperatures and high pressures. *Journal of Physics and Chemistry of Solids* **61,** 779–787 (2000).

21. Bobrov, K., Fisgeer, B., Shechter, H., Folman, M. & Hoffman, A. Thermal-programmed desorption (TPD) of deuterium from Di (111) surface: presence of two adsorption states. *Diamond and Related Materials* **6,** 736–742 (1997).

22. Falconer, J. L. & Schwarz, J. a. Temperature-Programmed Desorption and Reaction: Applications to Supported Catalysts. *Catalysis Reviews* **25,** 141–227 (2007).

Essentially, all models are wrong, but some are useful.

-George .P. Box

An alternative thermionic emission model for hydrogen terminated diamond surfaces

4

This chapter begins with a brief introduction to the field of thermionic emission on diamond and the challenges and limitations of its current theoretical model. Then a new theoretical model for thermionic emission from unstable surfaces is presented in detail. After that, the model is validated and tested against thermionic emission data collected from <100> single crystal and polycrystalline diamond. Finally, in view of the experimental results and the information obtained with the new model a route to improve thermionic emission devices is proposed.

4.1 Introduction

Thermionic emission (TE) from diamond surfaces has been studied for more than a decade now[1] and the overall state of the field has been reviewed in Chapter 1 Sect.1.2.3. In that section, the effects of different dopants on TE were discussed as well as the crucial role of the surface of hydrogen terminated diamond on the capability of the diamond to emit. Furthermore, it was highlighted that the main drawback that kept TE from diamond to be applied on devices was the fact that the hydrogen termination would disappear at moderate and high temperatures. This would nullify the TE capabilities of the diamond surface due to the loss of the negative electron affinity (NEA) and the increase of the work function (WF) (see Ch.1 sect1.1.1 and sect 1.1.2).

This fact is clearly seen on a typical TE plot of current (*J*) *vs* temperature (*T*), where after the TE current initially increases exponentially with temperature, at some point at high temperatures the current starts to decrease. When it reaches zero, the diamond surface becomes unable to emit again until the surface is re-terminated with hydrogen.

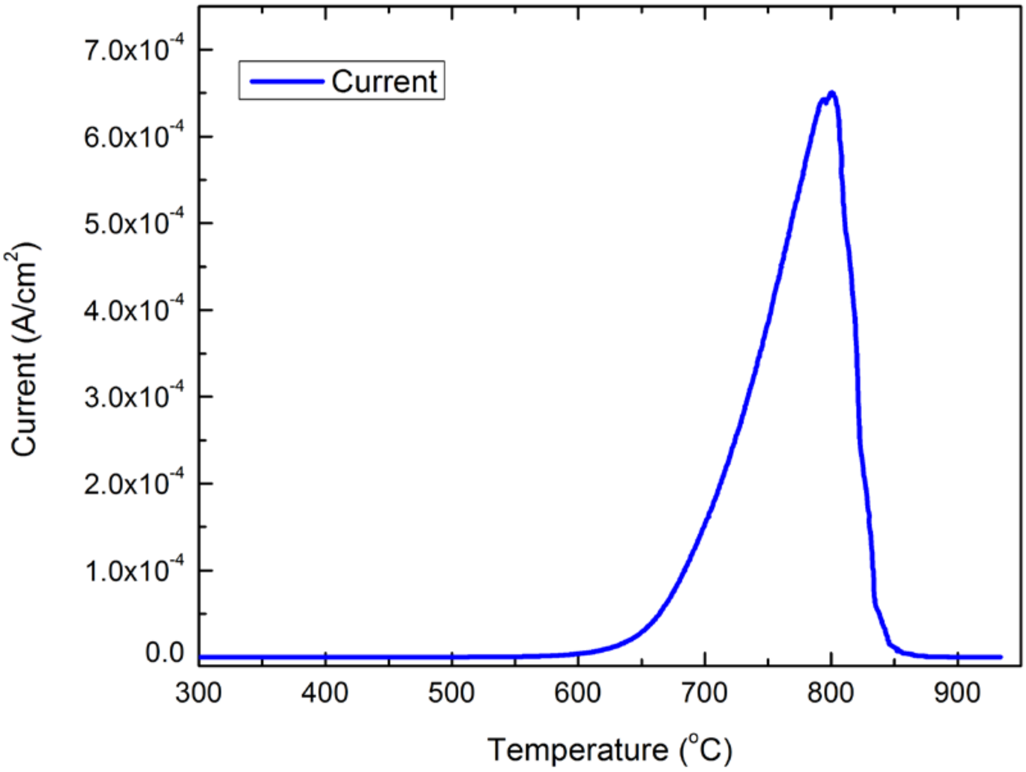

Figure 1: Current *vs* temperature plot of a typical thermionic emission experiment on diamond. Note the steep fall of thermionic current at ≈790°C due to hydrogen desorption.

The phenomenon of hydrogen desorption from diamond surfaces and its influence on TE current has, to the author's knowledge, only been studied by Paxton *et al*. Paxton studied the hydrogen desorption kinetics of hydrogen bonded to diamond while performing TE experiments. They were able to extract desorption energies for the hydrogen[2] and deuterium[3] bonded to polycrystalline diamond. However, their studies did not take into account the effect of the coverage on the emission nor the rate of desorption calculations. So, as they mention in their article, their results are to be taken with caution.

Although it is clear that hydrogen and its desorption kinetics have a critical role on the TE from diamond surfaces, the understanding of this convoluted phenomenon is still shallow. In addition, there are no theoretical models that can relate the TE current from hydrogen terminated diamond and the process of hydrogen desorption. Furthermore, the application of the traditional Richardson-Dushman equation (RDE) (see Ch.1 sect.1.2.1) to experimental data ignoring this convolution of phenomena might lead to an incorrect extraction of parameters like the WF and the Richardson constant *A*.

In this chapter, an alternative version of the Richardson-Dushman equation (RDE) is presented. This alternative version takes into consideration the effects of hydrogen desorption kinetics on the TE and reproduces the experimentally-observed behaviour of the current.

4.2 An alternative model for thermionic emission from unstable surfaces

The TE current from the surface of a solid is generally explained by the RDE[4]:

$$J = J(T) = AT^2 e^{-\frac{\phi}{kT}} \qquad (4.1)$$

where J is the TE current per square centimetre in Amperes, A is the Richardson constant, ϕ is the WF of the emitting surface, T is the temperature of the surface and k is the Boltzmann constant. However, the RDE assumes a stable surface, which means that the WF and the Richardson constant are constant for any temperature or don't change much. Also, it doesn't contain any terms related to the variation of the emitting area. Therefore, it is reasonable that the RDE cannot deal with unstable emitting surfaces as it is not really equipped for it.

In this section two different approaches to tackle this problem are presented, explaining their pros and cons and possible applicability to unstable surfaces.

4.2.1 1st approach: variation of the emitting surface area

The first approach to this problem was developed by the addition of a new term on the RDE that accounts for the variation in the emitting area as hydrogen desorbs. This was modelled as the variation of the hydrogen surface coverage θ with temperature following the Wigner-Polanyi equation[5]. The expression for the TE current from a monocrystalline uniform surface would be as follows:

$$J = J(T,\theta) = \left(AT^2 e^{-\frac{\phi}{kT}}\right)\cdot\, \theta \qquad (4.2)$$

where $\theta = \theta(T)$ is the surface coverage of hydrogen, which decreases according to certain desorption rate as temperature increases. If we take into consideration the fact that the surface is not uniform because of the presence of several crystallographic orientations, the equation can be expressed on a more general form:

$$J = \sum_i \left(AT^2 e^{-\frac{\phi_i}{kT}}\right)\theta_i \qquad (4.3)$$

where:

$$\sum_i \theta_i = 1 \qquad (4.4)$$

represents the coverage of the different emitting areas and ϕ_i is the work function associated to such areas.

This approach is based on equations developed by several authors[6–8] for the TE of patchy surfaces. It takes into consideration the presence of areas with different WF, coverages and desorption parameters and the fact that the total TE current is a convolution of the contributions of all these.

However, although the physics of the different processes seemed to be conceptually correct and is represented in the equation, the equation failed to reproduce the features observed in experimental data. This led to the development of a second approach described in the next section.

4.2.2 2nd approach: variation of the work function

The second approach modulates the TE current of the RDE by changing the value of the WF as function of hydrogen desorption. For a uniform monocrystalline surface, when an adatom bonds to the substrate there is a charge transfer between adatom and substrate. The direction of this transfer is determined by the electronegativity of the atoms involved. In our case, hydrogen is less electronegative than carbon so an electron is transferred to the substrate, leaving hydrogen with a positive charge and carbon with a negative charge. This creates a surface dipole that points towards the substrate and lowers the surface potential barrier and consequently the WF. As a result, the electron affinity of diamond becomes negative (see Ch1 sect.1.1.2).

This dipole theory of adsorbates has been explained by Gurney[9] using a quantum approach and by Langmuir[10] using a more classical approach. In addition, there is a significant amount of literature studying the effect of surface dipoles on the WF of alkali metal systems adsorbed on tungsten[11–13], molybdenum[14,15] and other metals[16–18]. These studies measured the dependence of the WF of a surface on the adsorbate coverage. Kröger *et al*, for example, studied the effect of adsorbed lithium on molybdenum <110> [19] and showed that as the surface coverage of lithium increases in the range of low coverages, the WF of the surface decreases rapidly at the beginning but the slope becomes smaller shortly after that. Then the WF reaches a minimum at $\theta \approx 0.4$ to then increase slightly, as can be seen in Fig.2.

The variation of the WF is generally described by[20]:

$$\phi = \phi_0 - e\frac{p_z}{\varepsilon_0}n_p \qquad (4.5)$$

where ϕ is the WF of the surface depending on the dipole density, ϕ_0 is the initial WF of the bare unterminated surface, e is the elementary electron charge, p_z is the dipole moment of the adsorbate-surface complex, ε_0 is the vacuum permeability and n_p is the area density of the dipole.

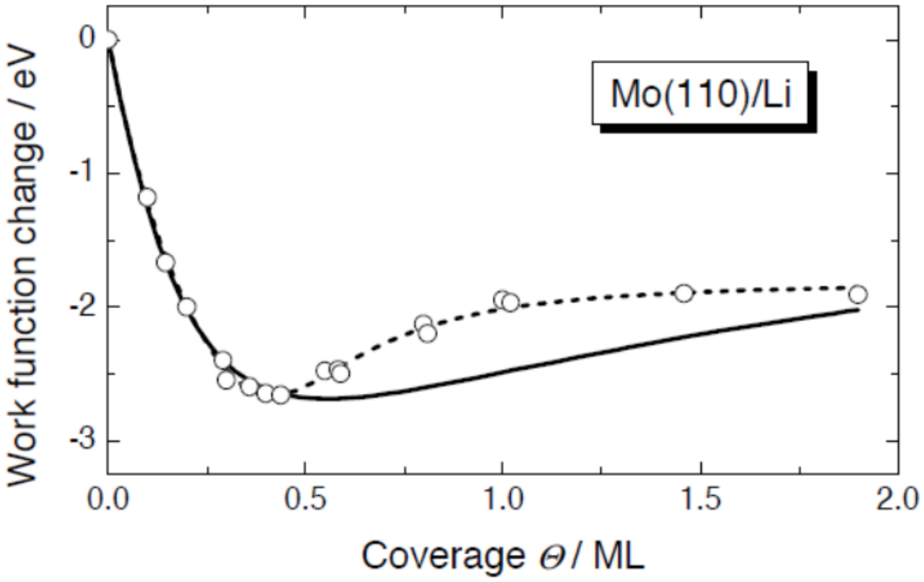

Figure 2: WF change of Mo <110> upon adsorption of lithium atoms. Circles: experimental data. Black solid line: Fit to the Topping model. Dashed line: guide to the eye. Taken from[20].

According to Eq.4.5 the WF decline should be linear but because the density of the surface dipoles increases, a depolarisation effect comes into play which causes a decrease of the magnitude of individual dipoles. This effect has been explained by Topping *et al*[21] and for a closed packed hexagonal lattice, it is summarised on the following equation[20]:

$$\phi(\theta) = \phi_0 - e\frac{p_z}{\varepsilon_0} n_s \frac{\theta}{\left(1 + 8.9\alpha_{el} n_s^{3/2} \theta^{3/2}\right)} \qquad (4.6)$$

where n_s is the density of surface atoms, θ is the fractional coverage and α_{el} is the electronic polarizability of the adsorbate-surface complex. This model agrees with experimental data at low coverages but deviates slightly for higher values (see Fig.2). Nevertheless, it is considered a valid model and it is widely used nowadays.

Hence, once it is established that the WF of a surface depends on the coverage of the adsorbate, it is possible to introduce a new term on the RDE for the WF based on Eq.4.6:

$$J = J(T, \phi) = AT^2 e^{-\frac{\phi(\theta)}{kT}} \qquad (4.7)$$

At this point it is worth briefly analysing the RDE from a mathematical point of view. The exponential term of the equation has a value close to zero at low temperatures. But this value quickly approaches 1 when the product kT is close or higher than the value of ϕ. The exponential term acts as a mathematical switch that activates the quadratic dependence of the current J with the temperature T; while the value of the WF sets the threshold for this activation. Therefore, by tuning this threshold it is possible to smoothly active or deactivate the TE current J.

It is now necessary to define how the coverage of the adsorbate will change depending on the temperature of the surface. The adatoms have a finite bond strength and an associated activation energy for desorption (ED), E_d. Therefore, if the temperature increases, the thermal energy might be sufficiently high to overcome the ED and consequently, break the chemical bonds that keep the adatom attached to the surface. The mathematical description of this process is shown below:

We can define the desorption rate r as the variation of surface coverage θ with time t:

$$r = -\frac{d\theta}{dt} \qquad (4.8)$$

and if we assume that the temperature of the surface T varies linearly with time we have:

$$T(t) = T_0 + \beta t \qquad (4.9)$$

where T_0 is the initial temperature and β is the heating rate of the surface in K/s. Differentiating Eq. 4.9 with respect to time we obtain:

$$dt = \frac{1}{\beta} dT \ , \ if\ \beta = 1 \ \Rightarrow \quad dt = dT \quad (4.10)$$

and therefore:

$$d\theta = -r dT \qquad (4.11)$$

If now we take into account the Wigner-Polanyi equation[22]:

$$r = \nu \theta^n e^{-\frac{E_d}{kT}} \qquad (4.12)$$

where υ is the rate constant or frequency factor in s^{-1}, n is the order of the reaction, T is the temperature of the substrate in Kelvin, k is the Boltzmann constant and E_d is the ED in eV/mol and combine it with Eq.4.11, we have:

$$d\theta = -\nu \theta^n e^{-\frac{E_d}{kT}} dT \qquad (4.13)$$

If we now apply integrals on both sides of Eq.4.13 we finally conclude that:

$$\theta(T) = \theta_0 - \int_{T1}^{T2} \nu \theta^n e^{-\frac{E_d}{kT}} dT \qquad (4.14)$$

where θ_0 is the initial coverage of the adsorbate.

Eq.4.14 represents the surface coverage of an adsorbate on a surface that is being heated at a rate of β = 1 K/s between the temperatures T_1 and T_2. If we now combine Eq.6, 7 and 14 we obtain:

$$J = J(T, \phi) = AT^2 e^{-\frac{\phi_0 - e\frac{p_z}{\varepsilon_0} n_s \left[\frac{\left(\theta_0 - \int_{T1}^{T2} \nu \theta^n e^{-\frac{E_d}{kT}} dT\right)}{\left(1 + 8.9 \alpha_{el} n_s^{3/2} \left(\theta_0 - \int_{T1}^{T2} \nu \theta^n e^{-\frac{E_d}{kT}} dT\right)^{3/2}\right)} \right]}{kT}} \qquad (4.15)$$

But Eq.4.15 can be simplified if we approximate Eq.4.6 with a linear piecewise function that approximates the shape of $\phi(\theta)$ (see Fig.2) so that:

$$\phi(\theta)=\begin{cases}\phi_0-A\theta\ ;\ 0\le\theta<\theta_m\\ \\ \phi_m+B\theta\ ;\ \theta_m\le\theta\le 1\end{cases}\qquad(4.16)$$

where:

$$A=\frac{\phi_0-\phi_m}{\theta_m}\ ;\ B=\frac{\phi_F-\phi_m}{1-\theta_m}\qquad(4.17)$$

and ϕ_0 is the WF of the unterminated surface, ϕ_{m} is the WF minimum at low coverages, θ_{m} is the coverage for the WF minimum and ϕ_{F} is the WF of the surface when θ=1.

Considering all of the above, we can write a generalised version of the modified RDE:

$$J=J(T,\phi)=\sum_i A_i T^2 e^{-\frac{\phi_i(\theta_i(T))}{kT}}\qquad(4.18)$$

where ϕ_{i} is given by Eq.16 and θ_{i} is given by Eq.4.14.

This mathematical description of the TE based on RDE should describe the TE current from a surface that relies on adsorbates to be able to thermionically emit electrons. This model is applicable to unstable surfaces with adsorbates that have patches with different WF and initial coverages. From now on we will refer to this model as the alternative Richardson model (ARM).

4.3 Thermionic emission from hydrogen terminated <100> single crystal diamond

In order to ascertain the validity of the ARM described in the previous section, it was applied to experimental TE data obtained from hydrogen terminated single crystal diamond (SCD). In our case, the substrate is a free standing nitrogen doped <100> SCD grown by the HPHT method[23,24], with an approximate doping concentration of 300 ppm of nitrogen. The substrate has a squared shape (≈ 9.8 × 9.8 mm) with trimmed corners and a thickness of ≈ 400 µm (see Ch2. sect.2.8.2).

SCD is an ideal substrate for this validation because its surface has a well-defined structure without grain boundaries or different crystallographic orientations. This restricts the possible number of components to be fitted by the ARM in the experimental data. These take the form of peaks on the TE plots with different WF or desorption characteristics. Furthermore, without grain boundaries and the presence of few defect states, the bulk properties of SCD are uniform. In the case of HPHT diamond, the amount of hydrogen trapped in the lattice is lower than that of CVD growth[24], which reduces the possibility of having unwanted hydrogen retermination from bulk hydrogen diffusing towards the surface.

4.3.1 Comparison between Richardson-Dushman Equation and the alternative Richardson model

Fig.3 shows the plot of TE current J *vs* temperature T for the hydrogen terminated SCD substrate previously described. The SCD was heated from 300°C (573 K) to 920°C (1193 K) at a rate of 1 K/s and cooled down to 300°C (573 K) at the same rate. The TE current from the single crystal starts around 450 °C (723 K) and peaks at 787°C (1060 K) with a maximum current of J_{max} = 1.53 mA/cm^2. All of the adsorbed hydrogen is desorbed in one heating run after which the diamond no longer emits unless it is reterminated with hydrogen.

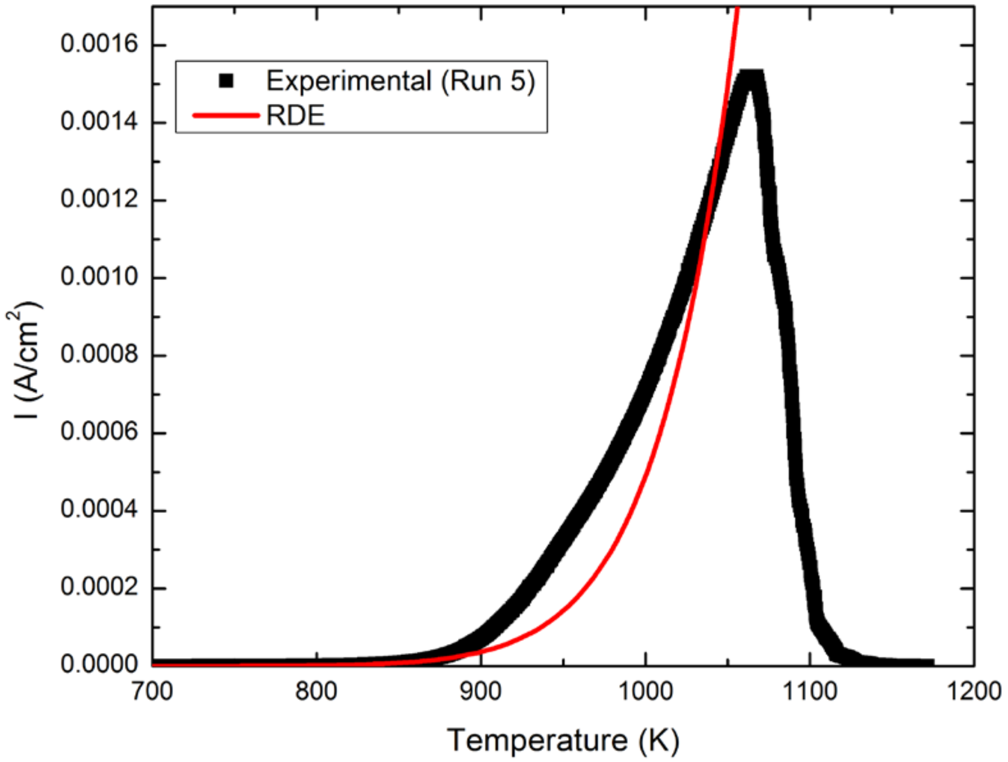

Figure 3: TE current from SCD. Black thick line: experimental data. Red line: RDE fit to experimental data. The RDE was fitted to data up to T = 1050 K as it cannot reproduce the steep current decrease after that temperature. The quality of the fit is $R^2 \approx 0.92$. The current uncertainty at the peak is 6.9×10^{-7} A.

The same figure shows the fit of the RDE to the experimental data. The free parameters on the fitting were the Richardson constant A and the WF ϕ. The former was left to range from 1 to 150 A/cm^2 K^2 while the latter could vary between 0.5 to 5 eV. The values obtained from the fitting were A = 1 A/cm^2 K^2 and ϕ = 1.751 eV with a fitting quality of R^2 = 0.92. The value of the WF seems reasonable. However, the value of A is two orders of magnitude lower that the theoretical value[25] A = 120 A/cm^2 K^2 and its value is limited by the lower bound of the allowed range. It was found that the value of the Richardson constant would always be fixed to the lower bound of the range; and changing this lower bound would cause the change on the WF. Furthermore, looking at the plot it is evident that the fit is not good as it greatly underestimates the emission at temperatures between 850K - 1020K and overestimates it above 1020K.

Also, the fitting of the RDE was constrained to temperatures below 1050K because after that temperature the emission decreases due to hydrogen desorption and the RDE cannot reproduce that effect. Because of the facts explained above, the parameters extracted from the experimental data with the RDE are not accurate and possibly erroneous in the case of A.

The same experimental data is plotted in Fig.4 but this time the ARM is used to fit the data. The data were fitted with the minimum number of peaks which in this case was two and the R^2 of the fit is R^2 > 0.999. The piecewise function approximating the variation of the WF with hydrogen coverage is (see Eq.4.19):

$$\phi(\theta) = \begin{cases} 7 - 11\theta \ ; \ \ 0 \leq \theta < 0.5 \\ \\ 1 + \theta \ ; \ \ 0.5 \leq \theta \leq 1 \end{cases} \qquad (4.19)$$

which means an initial WF of ϕ_0 = 7 eV, a WF minimum of ϕ_{m} = 1.5 eV at a hydrogen coverage of θ_{m} = 0.5 and a final WF of ϕ_{F} = 2 eV for θ = 1. The estimation of these parameters was carried out by a preliminary fitting of the RDE at temperatures below 900 K where the effects of hydrogen desorption are still negligible.

The hydrogen coverage of the surface was calculated with Eq.4.14 assuming an order of reaction[26–28] of n = 1. The free parameters for the fitting were: the Richardson constant A_i, the desorption energy $E_{\mathrm{d}i}$, the prefactor of the Wigner-Polanyi equation υ_i and the initial hydrogen coverage of each phase θ_{0i}.

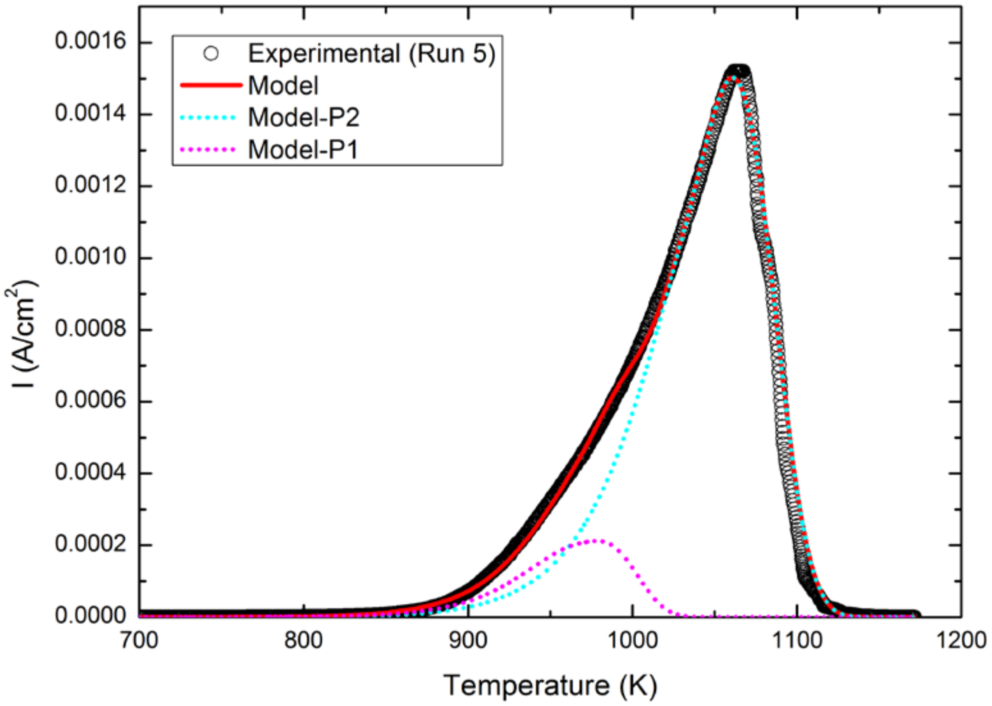

Figure 4: TE current from SCD. Black thick line: experimental data. Red line: ARM fit to experimental data. Pink dotted line: 1st component of the ARM. Cyan dotted line: 2nd component of the ARM fit. The quality of the fit is $R^2 > 0.999$. All the adsorbed hydrogen was desorbed on the first cycle. The current uncertainty at the peak is 6.9×10^{-7} A. The fit of the model has been performed by the collaborator Julian Anaya Calvo.

The ARM fits very well the experimental data, especially the final part of the curve, where the hydrogen desorbs quite fast. The approximation of the WF variation with coverage made with Eq.4.19 is also satisfactory. The parameters extracted from the fitting for the two peaks are summarised in Tab.1.

Table 1: Parameters obtained by the fitting of the ARM to the TE experimental data plotted in Fig.4.

Peak	A (A/cm^2 K^2)	E_d (eV/mol)	υ (1/s)	θ_0
1	79	3.245	3.42×10^{13}	0.4391
2	79	3.51	2.7×10^{13}	0.4358

The value of A is very close to the theoretical 120 A/cm^2 K^2 for both peaks. The prefactor υ is also very close to its theoretical value[22,29] $\upsilon = 1\times10^{13}$ s^{-1}. Even when assuming the two peaks have the same WF and similar initial coverage, the desorption energy is different. This reflects the fact that the hydrogen is bonded into the diamond surface in two different ways but this will be discussed in more detail in the next section.

Table 2: Parameters obtained by the fitting of the ARM to the TE experimental data of SCD on three heating runs. The SCD was reterminated with hydrogen before each new run. The data from Fig.4 and Tab.1 corresponds to the 5th run.

Run	4		5		6	
Peaks	1	2	1	2	1	2
A (A/cm^2 K^2)	79	79	79	79	79	79
E_d (eV)	3.245	3.520	3.245	3.510	3.245	3.530
υ (1/s)	3.42×10^{13}	2.75×10^{13}	3.52×10^{13}	2.7×10^{13}	3.3×10^{13}	2.7×10^{13}
θ_0	0.4310	0.4303	0.4391	0.4358	0.4391	0.4340

Regarding the stability of the values from Tab.1, the SCD was tested 6 times but the first three runs showed inconsistencies. Because of that, only the data from the last three experiments were fitted with the ARM. In the last three runs the free parameters were nearly identical, as can be seen in Tab.2. The small differences in emissions seem to be accounted for by very small variations of the initial coverage of the two surface phases associated to the peaks. Therefore, the ARM is not only consistent with the values but also successful in reproducing the experimental data.

4.3.2 Desorption kinetics and hydrogen species in <100> single crystal diamond

The surface of hydrogen terminated <100> SCD reconstructs as a C(100)-(2×1):H surface, where carbon atoms form dimer rows along the atomically flat terraces on the surface and are terminated by hydrogen atoms. This has been observed via scanning tunnelling microscopy by several groups[30,31] that inferred that for C(100)-(2×1):H, hydrogen is bonded to carbon atoms as a monohydride[32] (see Fig.5).

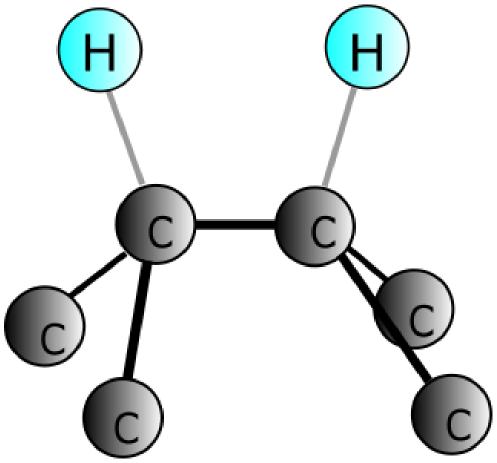

Figure 5: Representation of the C(100)-(2x1):H surface reconstruction for <100> SCD. Light blue spheres: hydrogen atoms. Grey spheres: carbon atoms.

In principle, it would be reasonable to expect that all of the hydrogen atoms on the surface have the same desorption energy as they all have the same C-H bond. However, if we use the values for the parameters E_d, υ, and θ extracted using the ARM from the experimental TE with Eq.4.12 and Eq.4.14, we can reconstruct the desorption plot for hydrogen on <100> SCD that would typically be obtained in a temperature programmed desorption (TPD) experiment[22,33] (see Fig.6).

The desorption rate for hydrogen in <100> SCD is plotted in Fig.6 (Top), where we can clearly see two desorption peaks associated with two ED (see Tab.1). The peak at lower temperatures is denoted P1 while the one at higher temperatures is denoted P2. This plot agrees with the findings of Bobrov *et al* that reported the absence of hydrogen on the surface of <100> SCD following an annealing at 950°C [31]. Studies by Thomas *et al*[28] on <100> SCD also report similar results , but their data shows only one wide peak, which might be the result of the convolution of the two peaks plotted in Fig.6 (Top). Conversely, on another study they report a TPD spectrum with a more complex structure[27] but they concluded that the cause for that was the progressive degradation of the surface due to rehydrogenation cycles. However, their rehydrogenation process was very aggressive and this degradation is not present in our case. In this thesis the rehydrogenation process is done at 450°C during 4 minutes (see Ch2 sect.2.8.2) while their reported method was performed at 900°C for 30 minutes. Su *et al*[34] also carried out TPD experiments on <100> SCD and described a wide peak composed by two convoluted peaks which agrees with the findings presented here.

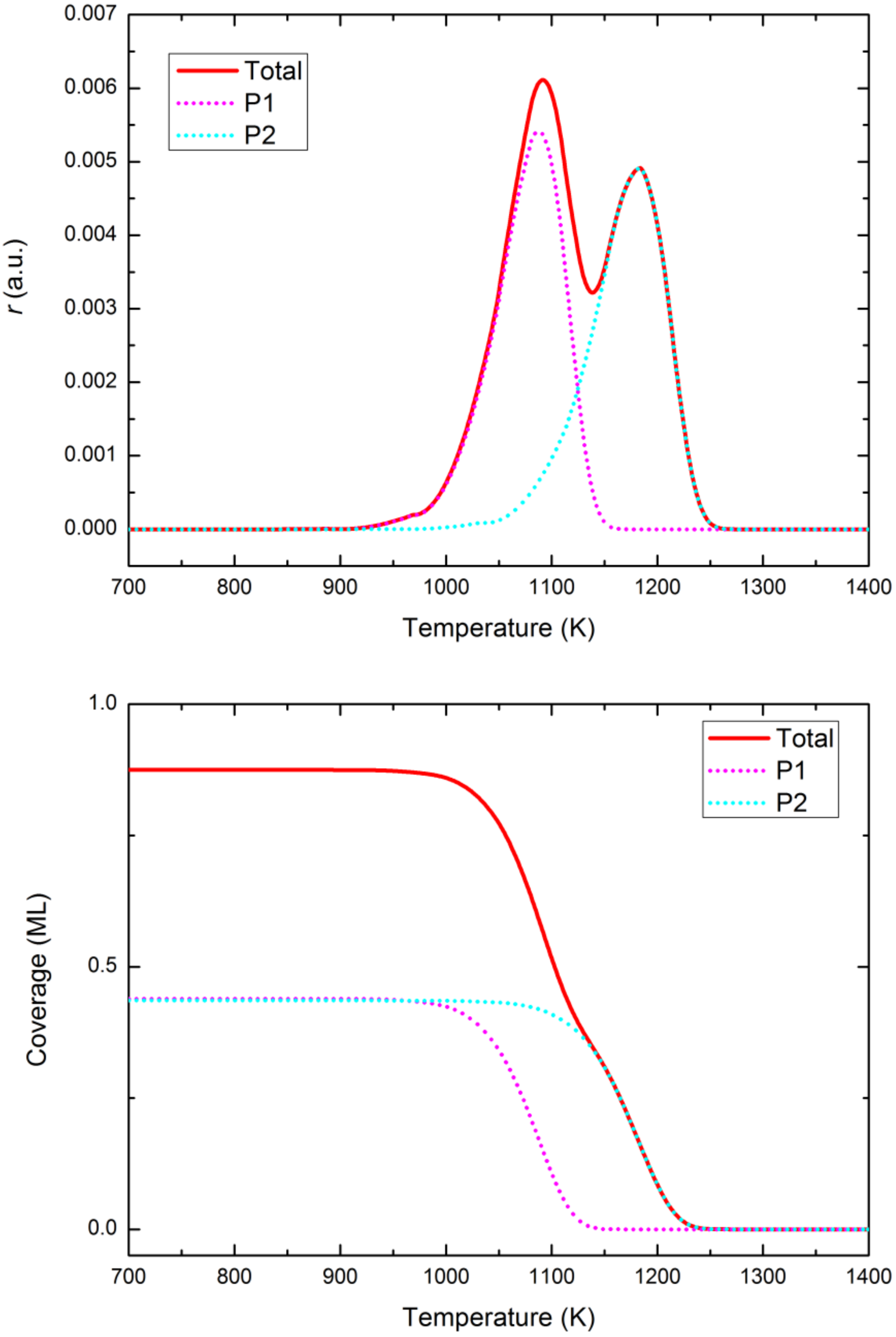

Figure 6: Top: Desorption rate plot for hydrogen on <100> SCD reconstructed from the parameters extracted using the ARM from the experimental data shown in Fig.4. Bottom: Coverage plot for hydrogen on <100> SCD reconstructed from the parameters extracted with the ARM from the experimental data shown in Fig.4. The two components in dotted colours (P1 and P2) correspond to the two peaks shown in Fig.4 and have the same colour codes to aid with comparisons between graphs.

Regarding the origin of the two desorption peaks there are two possible theories that are explained below.

If we examine the <100> SCD surface, we can have the following configurations: a carbon dimer with a double bond C=C without hydrogen, an incomplete carbon dimer with one hydrogen HC-C* and a fully terminated dimer with two hydrogen atoms HC-CH. But we are only interested in those containing hydrogen and hence, the last two. According to preliminary *ab initio* simulations of the C(100)-(2×1):H reconstruction of the <100> SCD surface carried out by our group, the desorption energy from the fully terminated dimer is higher than that of the incomplete dimer. This agrees with previous *ab initio* studies reporting dissimilar values for the two dimer configurations. While the incomplete dimer has a ED of 3.43 eV [35] and 3.868 eV [36], that for the fully terminated dimer is 4.28 eV [35] and 4.137 eV [36].

According to this theory and the results from the ARM, there should be two dimer phases on the <100> surface, either in the form of discrete patches or mixed across the surface with approximately equal initial coverage (see Tab2). But this prompts the question of why there are so many incomplete dimers on a hydrogen terminated surface. This has been discussed by Dawnkaski *et al*[37] and others[27] and apparently it is possible to have high concentrations of partially terminated dimers, at least at low coverages.

The second theory to explain the presence of two peaks on the desorption plot has been proposed by Su *et al*[33]. In their study, they performed TPD on <100> SCD and obtained one broad peak for the desorption diagram, which was found to be the convolution of two smaller peaks. They claim that the peak at higher temperatures is caused by the desorption of hydrogen on the flat terraces with a C(100)-(2×1):H reconstruction and fully terminated dimers. While the peak at lower temperatures is caused by hydrogen desorption from the domain boundaries of those terraces, meaning atomic steps and defect sites.

The reported ED for these two peaks is 3.25 eV for the low temperature peak and 3.46 eV for the peak at higher temperature. These values are practically the same as the ones reported on this thesis: 3.245 eV for the low temperature peak P1 and 3.5 eV for the high temperature peak P2. The density of atomic steps on the <100> SCD surface is sufficiently high, according to STM images of <100> SCD surfaces[31,38], to support the presence of a desorption peak associated with this type of defect.

In view of the two theories explained above, both seem reasonable and are supported by experimental and theoretical evidence. For the moment, it seems sensible to leave it as an open question as to which one is correct until further evidence is collected in the form of either experiments or *ab initio* simulations.

Table 3: Values of ED and frequency prefactor for hydrogen adsorbed on <100> SCD reported in the literature.

Source	E_d (eV)	υ (1/s)	Method
Bobrov *et al*[27]	3.816	1×10^{13}	TPD
Su *et al*[33]	3.25 - 3.46	1.4×10^{13}	TPD
Thomas *et al*[28]	3.154	1×10^{13}	TPD
Schulberg *et al*[39]	3.55	0.9×10^{13}	TPD
Yang *et al*[40]	3.46	1×10^{13}	TPD

The magnitude of the desorption energies extracted from the ARM are in agreement with the values reported in the literature for hydrogen adsorbed on the <100> SCD surface that has been hydrogen terminated with the microwave plasma method (see Ch2. Sect.2.8.2). Some of these values are summarised in Tab.3. However, the values reported by Paxton *et al*[2], who also used TE to measure the desorption energy, do not agree with the ones in this thesis. This might be caused by the fact that they assumed a constant desorption rate for all coverages when making the calculations.

4.4 Thermionic emission from hydrogen terminated polycrystalline diamond

The TE of hydrogen terminated nitrogen doped polycrystalline diamond (PCD) was also tested and the ARM was applied to the data obtained from the experiment. The nitrogen doped diamond film was grown with the hot filament method[41,42] on a free standing boron doped diamond substrate (see Ch2. Sect2.8.2). Hydrogen termination was carried out with microwave generated hydrogen plasma as in sect.4.3. TE tests were performed several times on each of the five different samples used with rehydrogenation of the surface before every experiment. Results were quite consistent so a representative set of data obtained in only one of the tests is presented here.

The methodology of the experiment is similar to the one followed in Sect.4.3 with a constant heating rate of 1K/s. However, the cooling rate is faster and therefore, some hydrogen remains on the surface after the first heating cycle and it takes a few more cycles to desorb it completely. See below the first two heating cycles for one of the samples.

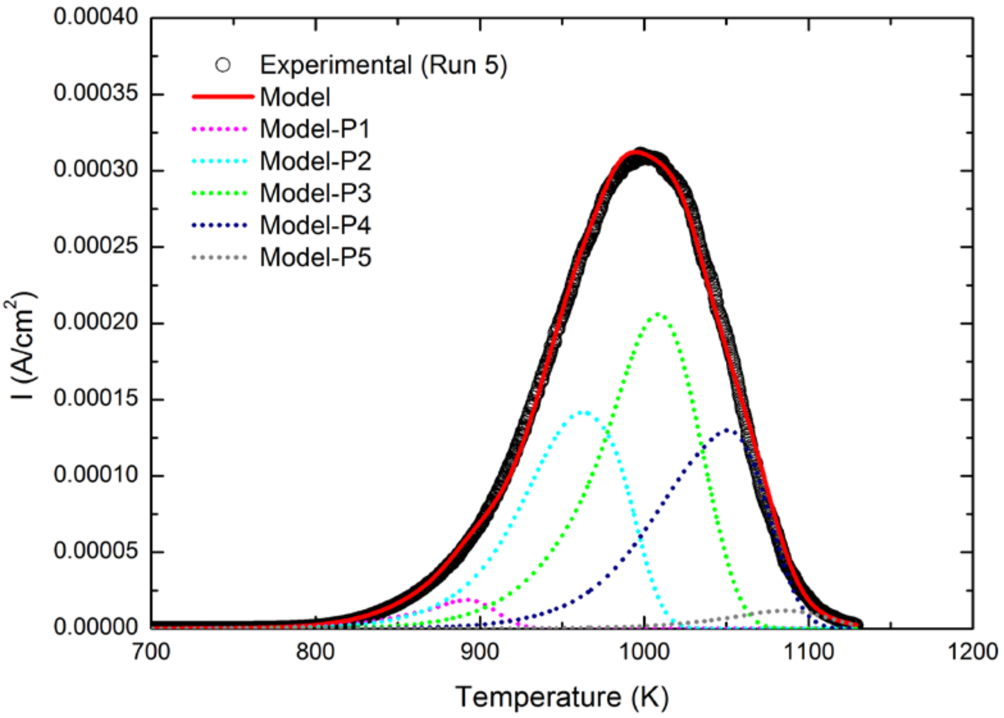

Figure 7: TE current from PCD. Black thick line: experimental data. Red line: ARM fit to experimental data. The dotted lines represent the different contributions to the TE current from different surface phases. This plot corresponds to the 1st heating cycle. The quality of the fit is $R^2 > 0.999$. The current uncertainty at the peak is 6.21×10^{-7} A. The fit of the model has been performed by the collaborator Julian Anaya Calvo.

For the sake of clarity, it is convenient to point out that in the case of SCD, experimental 'runs' consisted of only one 'heating cycle' while in this case one experimental 'run' consists of several 'heating cycles'.

Fig.7 plots the TE current of the first heating cycle for hydrogen terminated PCD. When comparing the maximum emission achieved by the PCD with that of the SCD, having been tested under the same conditions, it becomes clear that the SCD performs much better. The SCD achieves a maximum current of 1.5 mA/cm^2 while PCD only produces 0.3 mA/cm^2. Because of that, a potential diamond-based TE device would be more efficient and capable of producing higher current levels if made of SCD. On the subsequent heating cycles, without hydrogen retermination, the emission will substantially decrease with each cycle.

As is shown in Fig.7, when applying the ARM to the PCD data it is necessary to use five peaks to be able to reproduce the experimental data with an $R^2 > 0.999$. But this does not come as a surprise as the surface of a PCD is much more complex than of a SCD surface. In addition to the presence of different surface crystallographic orientations, there are also dislocations, grain boundaries and possibly graphitic areas where the hydrogen can bond and be desorbed upon heating. Therefore, the interpretation of the parameters extracted using the ARM must be undertaken with caution and being aware of the complexity of the PCD surface.

Table 4: Parameters obtained by the fitting of the ARM to the TE experimental data of PCD on the 1st heating cycle. The PCD was not reterminated with hydrogen before each new cycle. The data from Fig.4 and Tab.1 corresponds to the 2nd cycle.

Peak	1	2	3	4	5
A (A/cm^2 K^2)	79	79	79	79	79
E_d (eV/mol)	2.980	3.250	3.370	3.425	3.540
υ (1/s)	5.15×10^{13}	5.15×10^{13}	3.5×10^{13}	1.8×10^{13}	1.8×10^{13}
θ_0	0.440	0.438	0.430	0.419	0.390

The emission in PCD starts earlier that in SCD due to some peaks with low ED that completely disappear after the first heating cycle. The values for the Richardson constant and the frequency prefactor for the peaks are within the expected range and are similar to that of SCD. A summary of all the parameters can be found in table 4.

Regarding the values for the ED, the values for the 2nd and 5th peaks appear in the data from SCD with the same energies, so we could assign them to phases present on the <100> surface. Peaks 3 and 4 could be assigned to other orientations like <111> or <110> as their desorption energies lay in the same range[43,44]. In the case of the 1st peak, the one with the weakest desorption energy, we could venture to say that it might correspond to hydrogen weakly bonded to graphitic regions or sp2 carbon on the grain boundaries.

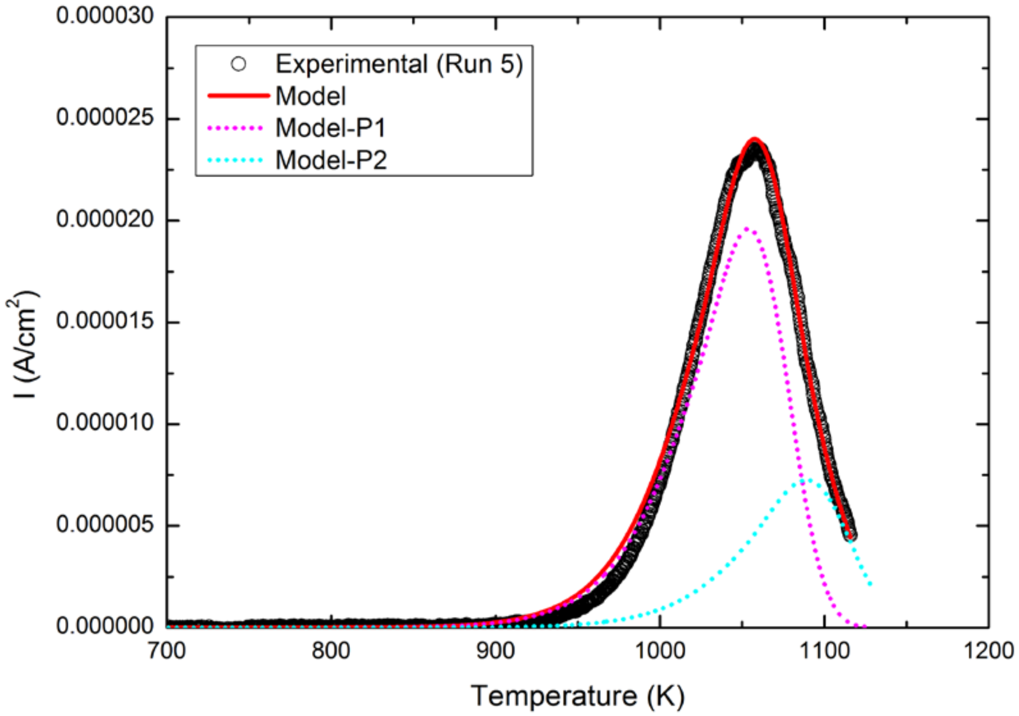

Figure 8: TE current from PCD. Black thick line: experimental data. Red line: ARM fit to experimental data. The dotted lines represent the different contributions to the TE current from different surface phases. This plot corresponds to the 2nd heating cycle. The quality of the fit is $R^2 > 0.999$. The fit of the model has been performed by the collaborator Julian Anaya Calvo.

It might seem surprising that the sum of the values for all the peaks is higher than 1 on the initial coverages of the different phases. However, this atypical value could have the following justifications. Firstly, the peak-to-valley roughness of the PCD is of the order of microns, which greatly increases the surface area in the diamond surface and with it, the apparent coverage. And secondly, it is possible that hydrogen migrates on the surface while the desorption is taking place[37]. This would mean that the coverage for one peak is transferred to the next instead of being desorbed; causing the coverage to appear higher than it actually is. This would not be unreasonable as the high number of defects on the surface would allow hydrogen atom to hop from site to site without the need for much energy.

On the 2nd heating cycle for the PCD shown in Fig.8 we can appreciate that out of 5 peaks, only two of them remain. These are peak 4 and peak 5, the ones with the highest desorption energy. Naturally, the initial coverage decreases with respect to the 1st cycle and with it, the maximum emission has decreased significantly. On the 3rd cycle, not shown for the sake of brevity, the peaks 4 and 5 are still present but with less coverage as more hydrogen desorbs. This shows the consistency of both the ARM and the TE data.

4.5 Possible surface optimisation routes for application in devices

In view of the information obtained by the application of the ARM to the SCD TE data, it is possible to assign TE current peaks to specific hydrogen chemical states on the diamond surface. This information might help to find ways to improve the TE performance of the surface and increase the chances of SCD to be used on a thermionic device.

In the case of SCD, we find that most of the emission comes from a peak with a desorption energy of $E_d \approx 3.5$ eV. In addition, this peak most probably corresponds to the hydrogen bonded on the fully terminated carbon dimer present on the flat terraces of the <100> SCD surface, which represents about half of the surface coverage. The other half is accounted for by either incomplete hydrogen dimers or dimers near the atomic steps and phase boundaries. Consequently, in order to increase the emission, a surface treatment could be tailored to favour the creation of more flat terraces. An example of the effect of increasing the coverage of the flat terraces is shown in Fig. 9. This figure plots the simulated TE current from a hydrogenated <100> SCD surface for different surface coverages of the flat terraces mentioned above. The plot was made assuming a constant heating rate of 1 K/s as in the experiments presented in the previous sections.

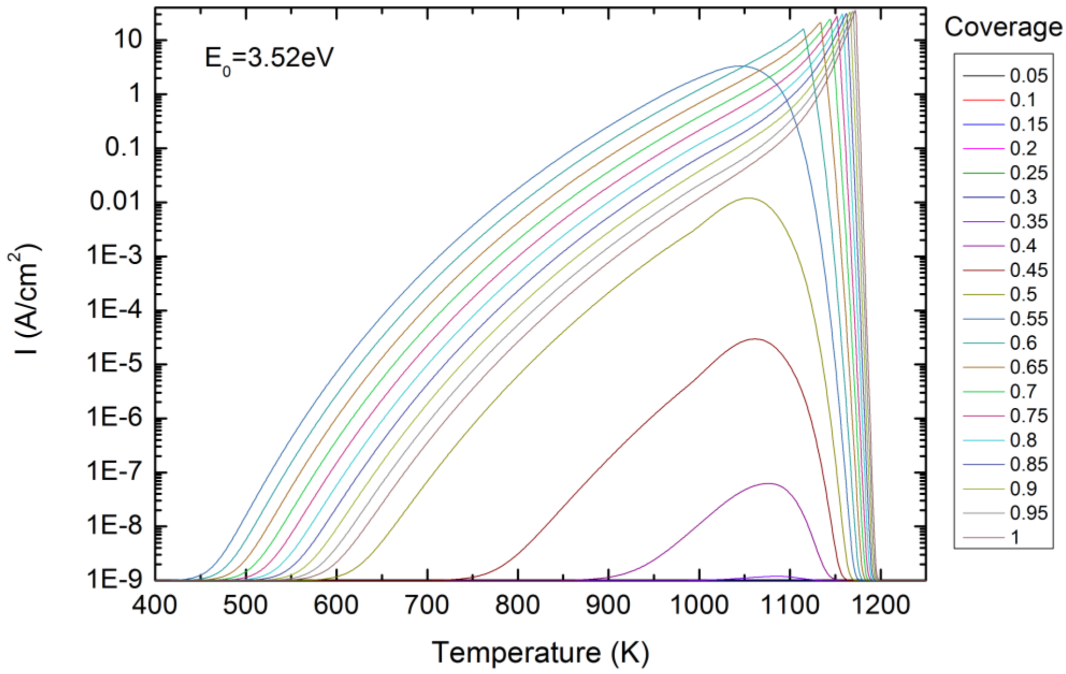

Figure 9: Simulated TE current plot from a hydrogenated <100> SCD surface assuming that only the flat terraces act as electron emitters. This corresponds to Peak 2 in Table.1 with an E_d = 3.52 eV. The different lines represent the TE current for different values of initial surface coverage of flat terraces. The simulation has been performed by the collaborator Julian Anaya Calvo.

From the plot, we can conclude that increasing the coverage of the flat terraces from the actual $\theta \approx 0.43$ up to $\theta \approx 0.55$ would increase the maximum emission three orders of magnitude. This could obviously have a tremendous impact on a potential diamond based thermionic device.

Additionally, if we examine Fig.6 (Top) that shows the desorption rates for the hydrogen in the flat terraces, we can see that at $T \approx 950$ K (677 °C) the desorption rate is still negligible. Hence, this would be the optimal working temperature for a potential device. If now we look back at Fig.9 and assume a surface coverage of 0.55 and a working temperature of 950 K, it would mean that the SCD could be constantly emitting a current of $J \approx 0.9$ A/cm^2 and this might open the door for SCD to be used on applications that were out of reach until now.

4.6 Conclusions

A modified Richardson-Dushman model has been applied to TE data from SCD and PCD proving that not only it can successfully reproduce the behaviour of the TE current but also extract significant amounts of information when compared to the regular RDE, especially in the case of SCD. However, the model still needs further improvements so that the WF can also be included as a free parameter when performing the fitting or to enable the use of Eq.6 to account for the WF variation with the coverage, instead of an approximation of Eq.16.

Overall, the ARM has proven to be a good tool for surface analysis capable of obtaining information typically restricted to TPD experiments. Moreover, it is possible that due to the high sensitivity of TE current to hydrogen coverage, a TE experiment coupled with the ARM might be even more sensitive than a regular TPD. On a typical TPD experiment the desorbed species must travel towards a quadrupole mass analyser of a specific detection efficiency, which might generate a delay that would shift the desorption peaks towards higher temperatures, leading to an overestimation of ED values. But in the case of TE this does not happen as the change TE current is detected instantly. Nevertheless, the use of the ARM is restricted to materials capable of producing a TE current, and this significantly limits its field of application.

Finally, a route for the improvement of the TE current from <100> SCD surfaces has been proposed, which could enable the use of this material in novel devices.

Acronyms

TE: Thermionic Emission

WF: Work Function

NEA: Negative Electron Affinity

RDE: Richardson-Dushman Equation

ED: Energy for Desorption

ARM: Alternative Richardson Model

SCD: Single Crystal Diamond

HPHT: High Pressure High Temperature

CVD: Chemical Vapour Deposition

TPD: Temperature Programmed Desorption

PCD: Polycrystalline Diamond

List of figures

List of tables

References

1. Köck, F. A. M., Garguilo, J. M., Brown, B. & Nemanich, R. J. Enhanced low-temperature thermionic field emission from surface-treated N-doped diamond films. *Diamond and Related Materials* **11,** 774–779 (2002).

2. Paxton, W. F. *et al.* The effect of hydrogen desorption kinetics on thermionic emission from polycrystalline chemical vapor deposited diamond. *Applied Physics Letters* **101,** 243509 (2012).

3. Paxton, W. F. *et al.* Role of deuterium desorption kinetics on the thermionic emission properties of polycrystalline diamond films with respect to kinetic isotope effects. *Journal of Applied Physics* **115,** 234904 (2014).

4. Richardson, O. W. Thermionic phenomena and the laws which govern them. *Nobel Lecture* (1929).

5. Luna, R., Millán, C., Domingo, M., Santonja, C. & Satorre, M. Á. Experimental study of the frequency factor in the Polanyi–Wigner equation: The case of C2H6. *Vacuum* **122,** 154–160 (2015).

6. Heinze, W. & Wagener, S. Die Anderung der Elektronenaustrittsarbeit bei der Aktivierung von Oxydkathoden. *Zeitschrift fur Physik* **110,** 164–188 (1938).

7. King, A. Photoelectric and Thermionic Investigations of Thoriated Tungsten Surfaces. *Physical Review* **53,** 570–577 (1938).

8. Herring, C. & Nichols, M. H. Thermionic emission. *Review of modern physics* **21,** (1949).

9. Gurney, R. W. Theory of Electrical Double Layers in Adsorbed Films. *Physical Review* **47,** 479–482 (1935).

10. Langmuir, I. Vapor pressures, evaporation, condensation and adsorption. *Journal of the American Chemical Society* **54,** 2798–2832 (1932).

11. Cousty, J., Riwan, R. & Soukiassian, P. Adsorption of alkali metals on W(100) : an EELS study. *Journal de Physique* **46,** 1693–1698 (1985).

12. Medvedev, V. K., Naumovets, A. G. & Smereka, T. P. Lithium adsorption on the (112) face of tungsten. *Surface Science* **34,** 368–384 (1973).

13. Loburets, A. T., Naumovets, A. G. & Vedula, Y. S. Surface diffusion of lithium on (011) face of tungsten. *Surface Science* **120,** 347–366 (1982).

14. Kanash, V., Fedorus, A. G. & Academy, U. Atomic-Structure and Work Function of the Metal-Film Lithium+(011) Face of Tungsten or Molybdenum. *Zhurnal Ehksperimental'noj i Teoreticheskoj Fiziki* **59,** 126–131 (1984).

15. Fedorus, A. G., Mitryaev, A. A. & Naumovets, A. G. Adsorption of oxygen on Mo (112) surface precovered with beryllium: formation of overlayer and electronic properties. *The European Physical Journal B* **86,** 477 (2013).

16. Politano, A., Formoso, V. & Chiarello, G. Alkali adsorption on Ni(111) and their coadsorption with CO and O. *Applied Surface Science* **254,** 6854–6859 (2008).

17. Tom, H. W. K. *et al.* Studies of alkali adsorption on Rh(111) using optical second-harmonic generation. *Surface Science* **172,** 466–476 (1986).

18. Yakovkin, I. N., Chernyi, V. I. & Naumovets, A. G. Effect of Li on the adsorption of CO and O on Pt. *Journal of Physics D: Applied Physics* **32,** 841–844 (1999).

19. Kröger, J., Bruchmann, D., Lehwald, S. & Ibach, H. Adsorption of lithium on Mo(110): an EELS study of the adsorbate vibrations and substrate phonons. *Surface Science* **449,** 227–235 (2000).

20. Ibach, H. *Physics of Surfaces and Interfaces*. (Springer Berlin Heidelberg, 2006). doi:10.1007/3-540-34710-0

21. Topping, J. On the Mutual Potential Energy of a Plane Network of Doublets. *Proceedings of the Royal Society A: Mathematical, Physical and Engineering Sciences* **114,** 67–72 (1927).

22. King, D. A. Thermal desorption from metal surfaces: A review. *Surface Science* **47,** 384–402 (1975).

23. Pal'yanov, Y. *et al.* Crystal growth and characterization of HPHT diamond from a

phosphorus-carbon system. *Diamond and Related Materials* **12,** 1510–1516 (2003).

24. Koizumi, S., Nebel, C. & Nesladek, M. *Physics and Applications of CVD Diamond*. (Wiley-VCH Verlag GmbH & Co. KGaA, 2008). doi:10.1002/9783527623174

25. Crowell, C. R. The Richardson constant for thermionic emission in Schottky barrier diodes. *Solid-State Electronics* **8,** 395–399 (1965).

26. Bobrov, K., Fisgeer, B., Shechter, H., Folman, M. & Hoffman, A. Thermal-programmed desorption (TPD) of deuterium from Di (111) surface: presence of two adsorption states. *Diamond and Related Materials* **6,** 736–742 (1997).

27. Bobrov, K., Shechter, H., Folman, M. & Hoffman, A. Deuterium adsorption-desorption from diamond (100) single crystal surfaces studied by TPD. *Diamond and Related Materials* **7,** 170–176 (1998).

28. Thomas, R. E., Rudder, R. A. & Markunas, R. J. Thermal desorption from hydrogenated and oxygenated diamond (100) surfaces. *Journal of Vacuum Science & Technology A: Vacuum, Surfaces, and Films* **10,** 2451–2457 (1992).

29. Falconer, J. L. & Schwarz, J. a. Temperature-Programmed Desorption and Reaction: Applications to Supported Catalysts. *Catalysis Reviews* **25,** 141–227 (2007).

30. Stallcup, R. E. & Perez, J. M. Scanning Tunneling Microscopy Studies of Temperature-Dependent Etching of Diamond (100) by Atomic Hydrogen. *Physical Review Letters* **86,** 3368–3371 (2001).

31. Bobrov, K. *et al.* Atomic-scale visualization and surface electronic structure of the hydrogenated diamond C(100)-(2x1):H surface. *Physical Review B* **68,** 195416 (2003).

32. Kawarada, H., Sasaki, H. & Sato, A. Scanning-tunneling-microscope observation of the homoepitaxial diamond (001) 2×1 reconstruction observed under atmospheric pressure. *Physical Review B* **52,** 11351–11358 (1995).

33. Su, C. & Lin, J.-C. Thermal desorption of hydrogen from the diamond C(100) surface. *Surface Science* **406,** 149–166 (1998).

34. Su, C. & Lin, J. Thermal desorption of hydrogen from the diamond C (100) surface.

406, 149–166 (1998).

35. Hukka, T. I., Pakkanen, T. A. & D'Evelyn, M. P. Chemisorption of Hydrogen on the Diamond (100)2 .times. 1 Surface: An ab Initio Study. *The Journal of Physical Chemistry* **98,** 12420–12430 (1994).

36. Jing, Z. & Whitten, J. L. Ab initio studies of H chemisorption on C(100) surface. *Surface Science* **314,** 300–306 (1994).

37. Dawnkaski, E. J., Srivastava, D. & Garrison, B. J. Time dependent Monte Carlo simulations of H reactions on the diamond {001}(2×1) surface under chemical vapor deposition conditions. *The Journal of Chemical Physics* **102,** 9401–9411 (1995).

38. Hellner, L., Mayne, a. J., Bernard, R. & Dujardin, G. Hydrogenated diamond crystal C(100) conductivity studied by STM. *Diamond and Related Materials* **14,** 1529–1534 (2005).

39. Schulberg, M. T., Fox, C. a., Kubiak, G. D. & Stulen, R. H. Hydrogen desorption from chemical vapor deposited diamond films. *Journal of Applied Physics* **77,** 3484 (1995).

40. Yang, Y. L., Struck, L. M., Sutcu, L. F. & D'Evelyn, M. P. Chemistry of hydrogen on diamond (100). *Thin Solid Films* **225,** 203–211 (1993).

41. May, P. W. Diamond deposition in a hot-filament reactor using different hydrocarbon precursor gases. **68,** 299–305 (1993).

42. Ali, M. & Ürgen, M. Diamond films grown without seeding treatment and bias by hot-filament CVD system. *Solid State Sciences* **14,** 540–544 (2012).

43. Su, C. *et al.* Hydrogen chemisorption and thermal desorption on the diamond C(111) surface. *The Journal of Chemical Physics* **107,** 7543–7558 (1997).

44. McGonigal, M., Kempel, M. L., Hammond, M. S. & Jamison, K. D. Isothermal hydrogen desorption from the diamond (100)2×1 surface. *Journal of Vacuum Science & Technology A: Vacuum, Surfaces, and Films* **14,** 2308–2314 (1996).

It is a capital mistake to theorize
before you have all the evidence.
It biases the judgment.

-Arthur Conan Doyle

5

Work function tuning *via* Plasmo-electric potentials

In this chapter, a new method to tune the work function of surfaces is studied. This involves the use of light-induced plasmo-electric potentials. As a first approach we focus on the study of plasmo-electric potentials on silver nanoplates and the effects over their work function. More specifically, we study the transient behaviour of plasmo-electric potentials on the nanoplates and analyse the causes for the observed behaviour.

The chapter starts with an introduction and review of the field of plasmo-electric potentials followed by the characterisation of the samples used in this chapter. Then experimental data on the transient behaviour of plasmo-electric potentials under different illumination and temperature conditions are presented. Subsequently, a mathematical model for the transient behaviour of the potentials is discussed along with the processes occurring on the silver nanoplate-substrate interface. Finally, the last section reports on the heterogeneous local behaviour of the plasmo-electric potentials for a single nanoplate.

5.1 Introduction

5.1.1 Plasmoelectric potentials: State of current research

Plasmo-electric potentials (PEP) were first reported by Sheldon *et al* in their seminal paper[1]. PEP manifests itself as an induced electric potential on a nanoparticle whose LSP modes are being excited *via* laser illumination. Sheldon *et al* studied a particle-on-film system of Au nanospheres deposited on an ITO/glass substrate, illuminated with a tuneable laser, with a Kelvin probe force microscope (KPFM). KPFM[2], as described in Ch.2, is a an atomic force microscopy variant used to measure both surface potentials and surface topography which is described in detail later on and in Ch.2.

Sheldon *et al* observed that upon illumination there is a shift in the surface potential (SP) of their nanoparticle array of a few tens of milivolts. According to their findings the SP shift shows a dependence on the laser power and on the excitation wavelength. Moreover, the induced SP shift appears to be negative -with respect to the SP in the dark- when the illumination wavelength sits below the plasmonic resonance frequency and positive when the illumination wavelength is above the latter. In addition, there was no SP shift when exciting the nanoparticles at their resonant wavelength. It is worth noting that all the results presented in their study are for a steady-state regime.

Sheldon *et al* presented a model for the PEP effect that was further elaborated by van de Groep *et al* in a later publication[3]. Their proposed model approaches the PEP effect from a thermodynamic point of view and concludes that PEPs are caused by a light driven change in the particle charge. From their findings it appears that this charge flow is thermodynamically favoured to occur under illumination. The model from van de Groep *et al* is fairly comprehensive and although it offers a reasonable explanation of PEP, it doesn't reproduce some of the trends observed on the experimental data shown by Sheldon *et al* such as the smooth decay of the magnitude of PEP when the excitation wavelength moves away from the resonance wavelength of the nanospheres.

The PEP field is still at an early development stage where detailed research on different particle-substrate systems is yet to be done. Moreover, the relation between PEP and other plasmonic driven processes has not been studied to this date. This means that further research is needed in order to fully comprehend this phenomenon and its interactions with other fields.

5.1.2 Methodology of the experiment

The PEP manifests itself as a change on the work function (WF) of the Ag nanoplate under illumination. KPFM was the technique of choice to monitor and map these changes. Apart from monitoring changes in the WF, KPFM can simultaneously map the topography of the sample (see Ch2, Sec. 2.2.2). It is worth pointing out that KPFM doesn't measure WF but the WF difference between sample and probe, which is called the contact potential difference (CPD). Therefore, in order to know the absolute WF value of the sample it is necessary to calibrate the probe against a reference sample of known WF. However, on this study, we focus on the shift of the WF ($\Delta\phi$)

which happens to be equal to the CPD shift. So no calibration is needed for our experiment as $\Delta\phi = \Delta CPD = PEP$.

In order to study the PEP, a particle-on-film system was used. This system is composed of Ag triangular nanoplates capped with a polyvinylchloride (PVP) layer deposited on an indium tin oxide (ITO) substrate. The nanoplates have an approximate diameter of ≈180 nm and a height of ≈20 nm (see Ch2, Sec. 2.8.3).

The samples were placed inside an ultra high vacuum chamber where they were scanned with the KPFM until a suitable Ag nanoplate could be selected for the experiment. Two main experiments were carried out: WF mapping of the Ag nanoplates with and without illumination and PEP transient measurements. For the latter, the tip of the KPFM probe was placed on a point of interest atop the plate. After that, the sample was exposed to cycles of darkness-illumination - darkness while the KPFM recorded the WF changes ($\Delta\phi$) on the selected point. The total cycle time was of 2400 s (40 min), starting with 300 s (5 min) of darkness to establish the CPD baseline, 1500 s (20 min) of illumination and 1000 s (15 min) of darkness. The sample would be left to settle down for a minimum of 20 min between experiments. The laser used for illumination was a circularly polarised continuous wave diode laser with a wavelength 980 nm and a maximum power density of ≈ 90 mW/cm^2 (see Ch2, Sec. 2.3.3).

As the WF is highly sensitive to surface contamination, the experiments were carried out under ultra high vacuum conditions (UHV) to minimise the influence of absorbed species present on the samples during experiments. Low temperature experiments were also carried out by cooling the sample with LHe down to 30K and following the same procedure described above to study the influence of temperature in PEP transients. The effect of the laser power density was also studied by performing illumination cycles at different powers.

5.2 Sample characterisation

5.2.1 Silver nanoplate distribution and morphology

Samples consisting of Ag nanoplates deposited on ITO were characterised to learn their distribution and morphology prior to the examination with KPFM. Fig.1 shows an SEM image of Ag nanoplates deposited on ITO. This image shows that the nanoplates are evenly distributed across the substrate apart from some localised aggregates. Some spherical particles present on the sample show a white colour on the image. We believe that these particles are a residue from the nanoplate synthesis process. Preliminary electron energy loss spectroscopy (EELS) measurements confirmed the presence of crystallised salt particles that could correspond to the spherical particle observed in Fig.1. Nevertheless, the topographical mapping capability of KPFM allowed us to select the correct nanoplates based on their morphology.

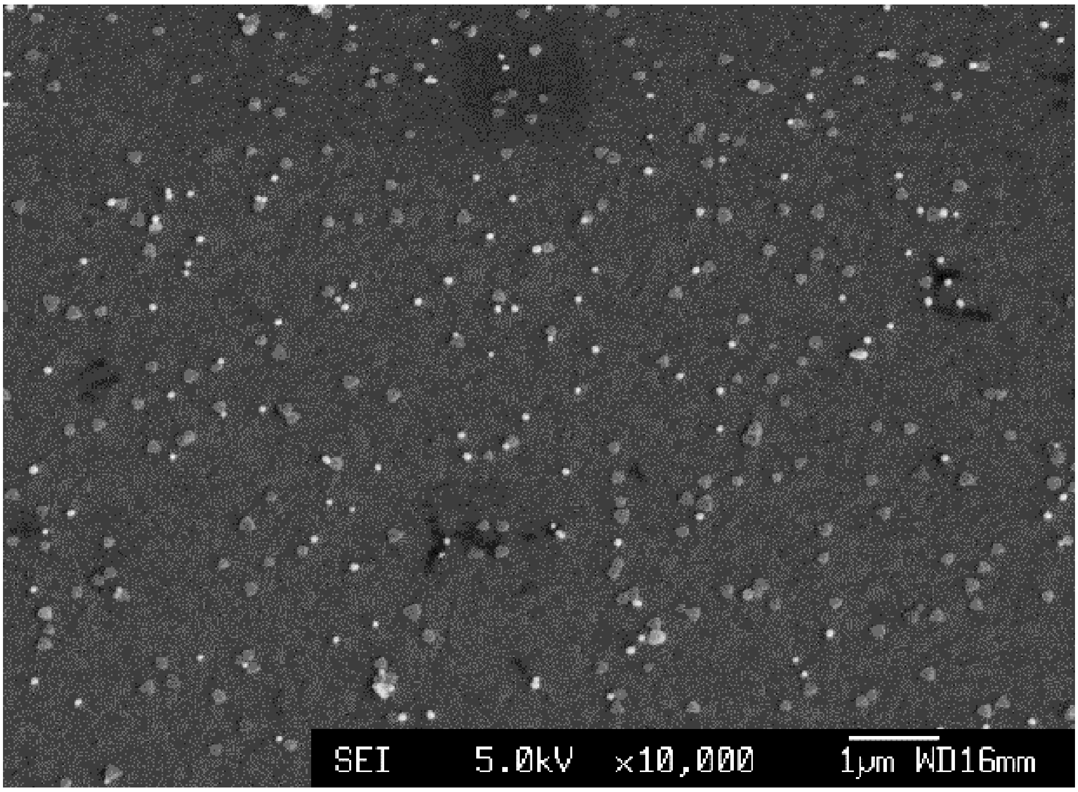

Figure 1: SEM image of Ag nanoplates deposited on ITO. The nanoplates show an homogeneous distribution apart from localised aggregates. Some white spherical particles are also present, which are believed to be crystallised salt residues from the nanoplate synthesis process.

The morphology of a typical Ag nanoplate used for this study is shown on Fig.2. This figure shows the 3D rendering of the Z channel of the KPFM which maps the topography of the sample. As it can be seen the Ag nanoplate has a truncated triangular shape with a length from base to apex of around ≈ 220 nm. This agrees with the specifications provided by the manufacturer[4]. The thickness of the nanoplate is ≈ 16 nm.

The surface of the nanoplate is smooth but it presents some flat wide bumps or protuberances that account for around 30% of the surface of the nanoplate. Fig.3 shows the height profile across a typical Ag nanoplate deposited on ITO. As can be seen from the height profile of the Fig.3, these protuberances have a height of ≈1.3 nm relative to the surface of the plate.

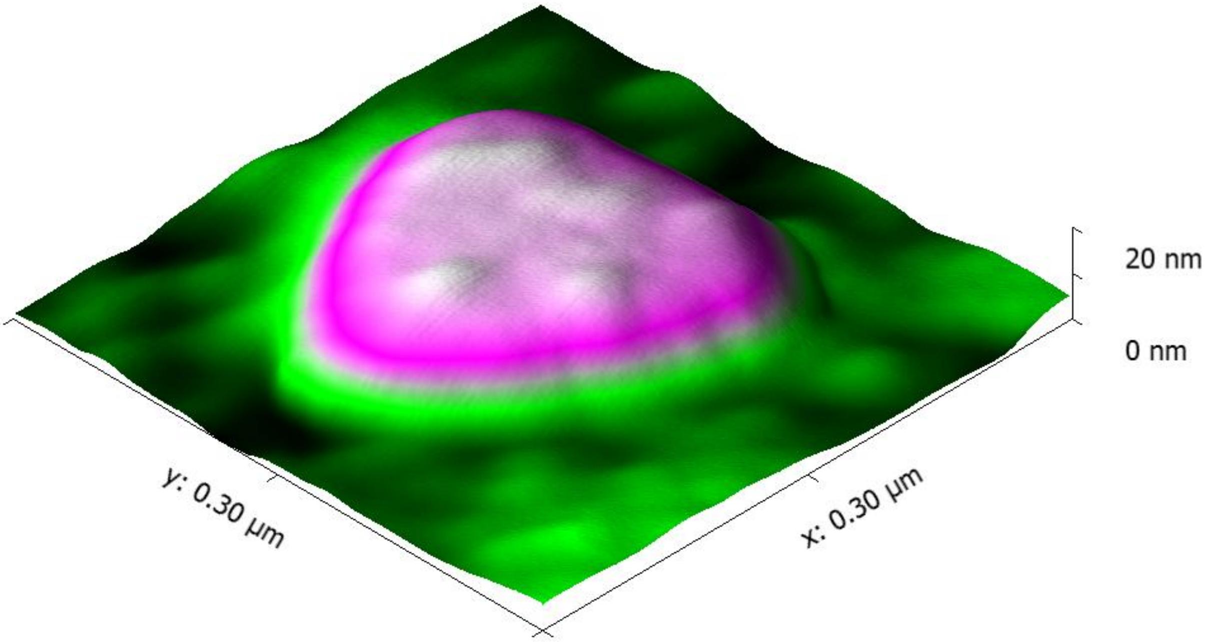

Figure 2: 3D rendering of the topographical image (Z channel) acquired with KPFM of a typical Ag nanoplate deposited on ITO.

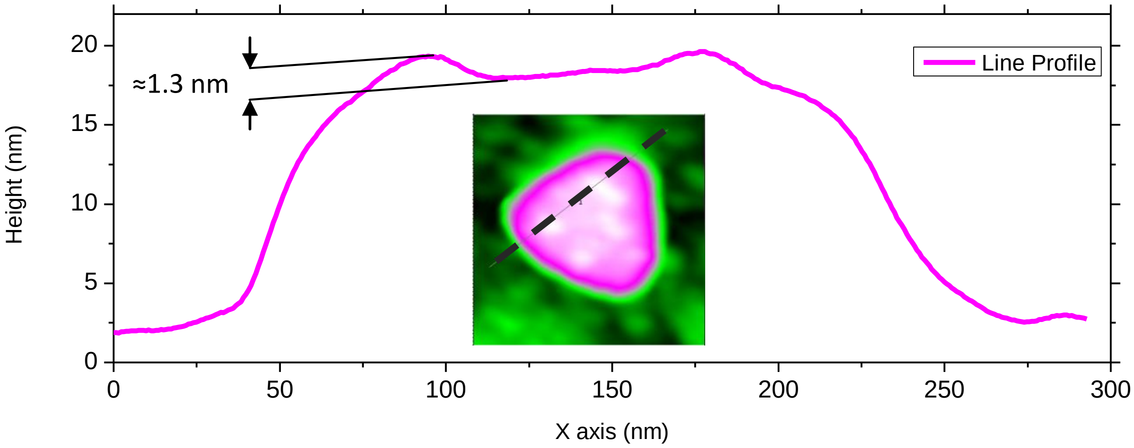

Figure 3: Height profile of a typical Ag nanoplate deposited on ITO. The profile was extracted from a KPFM topographical image. The excerpt shows the profile path over the nanoplate. The profile shows the position and height of protuberances on top of the nanoplate.

Ag nanoplates were also characterised with transmission electron microscopy (TEM) prior to deposition on the ITO substrate. Fig.4 shows a TEM image of a typical Ag nanoplate from the colloidal solution deposited on carbon film. The TEM image shows good agreement with the Fig.4 in terms of morphology and dimensions of the Ag nanoplate. The plate appears to be a single crystal with the <111> orientation with no visible twinning, dislocations or bending contours[5].

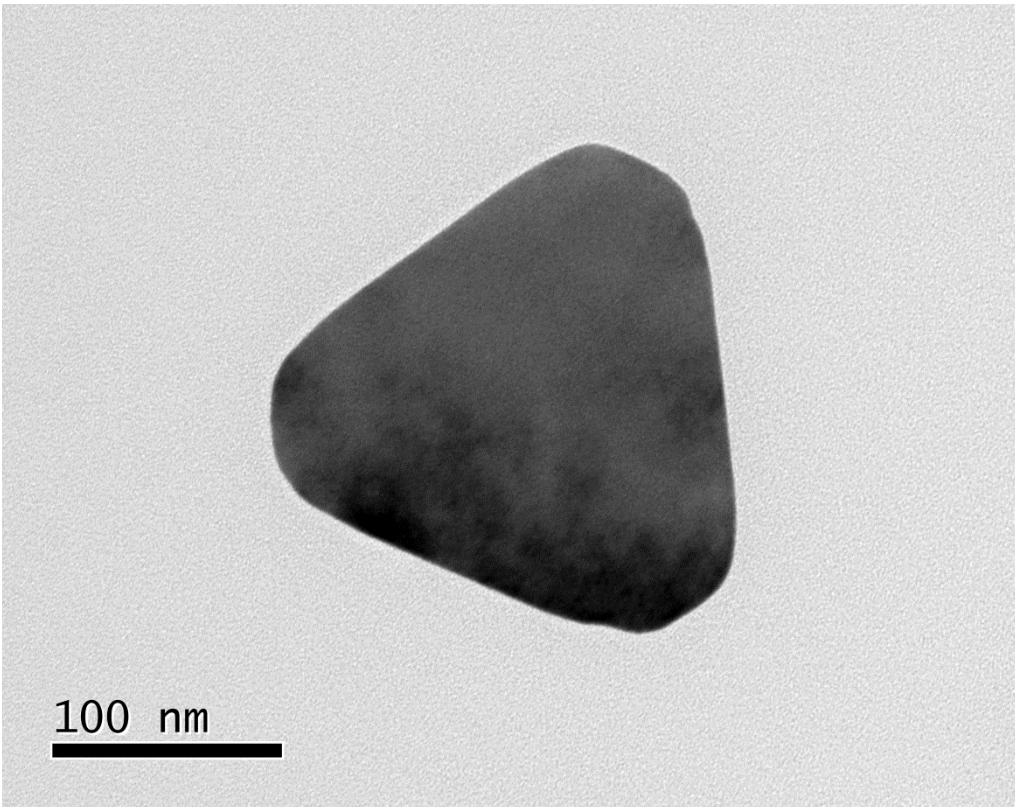

Figure 4: TEM image of a typical Ag nanoplate from the colloidal solution used for this study. The nanoplate appears to be a single crystal with the <111> orientation facing upwards. No twinning or dislocations are visible.

5.2.2 Optical properties of silver nanoplates

The optical response of the sample with Ag nanoplates deposited on ITO was measured at normal incidence by a Fourier image microscope[6] (see Ch2, Sec. 2.5).

In Fig.5 (right) we can see that the optical response for the Ag nanoplate colloidal solution, as supplied, shows a maximum extinction coefficient at ≈1050 nm [4]. Once the nanoplates have been deposited on ITO, the extinction peak is shifted towards lower wavelengths and situated around 810 nm (see Fig.5 (left)).

This difference is caused by the change in the medium surrounding the nanoplates[7–9]. It is important to note that once the nanoplates have been deposited, they form aggregates which have different resonant wavelengths than individual nanoplates. Which causes the optical response plot to be a convolution of the responses of individual nanoplates and the different aggregates. The red line in the same figure indicates the wavelength on the laser used for illumination. The fact the laser excitation is not on a resonant peak is advantageous as according to Sheldon *et al*[1], excitation on resonant wavelengths does not produce a PEP response.

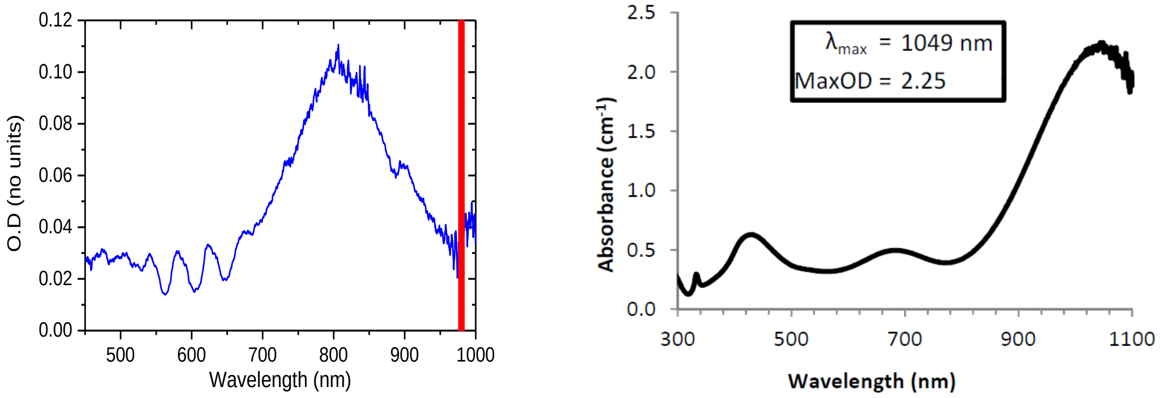

Figure 5: Optical response of Ag nanoplates. Left: Ag nanoplates deposited on ITO. Red line represents the excitation wavelength of the laser. This measurement has been carried out by the collaborator Sara Nuñez Sanchez. Right: Ag nanoplates in colloidal solution (according to the supplier)[4].

5.3 Mapping of plasmoelectric potentials on Ag nanoplates

In Fig.6 (left) is shown the WF map of a typical Ag nanoplate deposited on ITO. It is observed that there is a clear WF contrast between the WF of the Ag nanoplate and that of the ITO. The nanoplates have a triangular shape which indicates that the top of the nanoplate corresponds to the <111> crystallographic plane[10]. When compared to the <100> and <110> planes, the <111> has the higher WF for most of the metals[11]. However, the absolute WF value of the Ag <111> plane varies greatly depending on the purity of the metal and, of course the surface cleanliness. For a pure, clean <111> Ag single crystal, the WF is ≈4.46 eV after a number of cleaning cycles[12]. But if the Ag is untreated, the WF can range from 4.56 to 4.78 eV [12,13] in cases where there are contaminants like carbon or sulphur. Taking into account that there is a capping layer of PVP, the effect upon the WF of Ag would depend on its thickness. According to manufacturer estimates, this thickness is between 1-2 nm. For the case of PVP capped ITO for example, PVP causes a reduction in the WF[14,15]. So it could be expected that a similar effect happens for polymer capped metals as was reported by Zhou *et al*[16].

In our Ag nanoplates, according to the KPFM data, the WF of the Ag ranges between 4.35 to 4.60 eV. These values lie within the expected range for a Ag surface which may have a PVP capping layer as explained earlier. As a result, we consider that the flat areas of lower WF within the Ag nanoplates correspond to either Ag <111> or PVP capped PVP-Ag <111>. While the areas with higher WF matching with the surface protuberances correspond to PVP accumulation, contamination or dislocations as mentioned above. This matter will be discussed in more detail in

Sect.5.6. Conversely, the WF of the ITO substrate is $\phi_{\mathrm{ITO}} \approx 4.60$ eV, which seems to agree with the values reported in the literature for oxygen terminated ITO substrates[17–21].

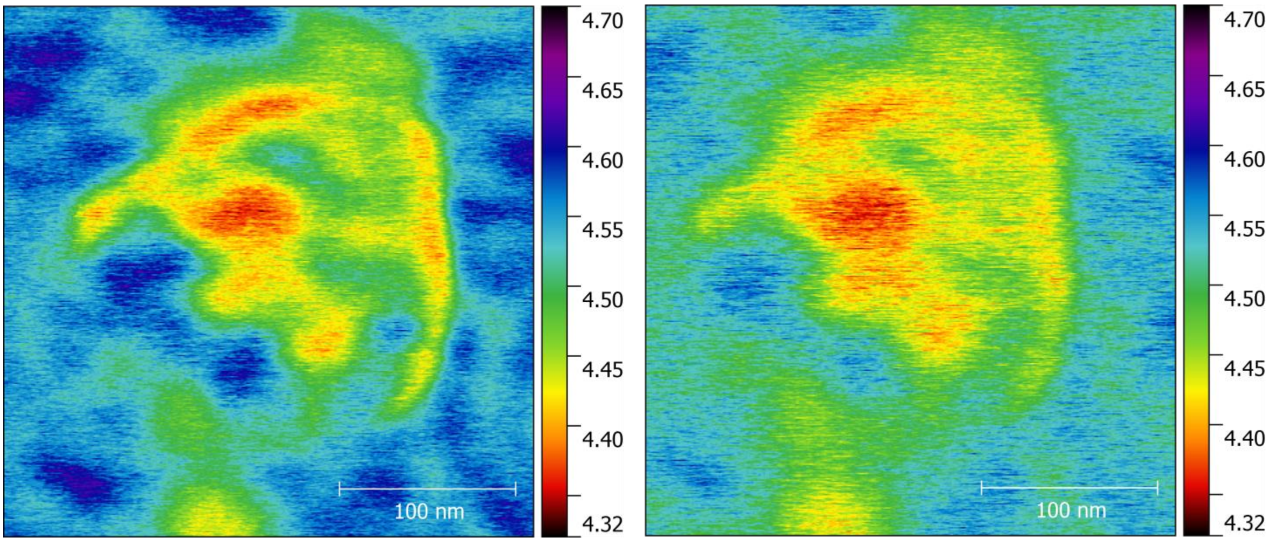

Figure 6: Work function map of a Ag nanoplate on ITO. (Left): without illumination. (Right): With illumination.

In order to crosscheck the WF values obtained *via* KPFM, the WF of the Ag nanoplates was measured with an energy filtered photoelectric electron microscope (EF-PEEM). Ag nanoplates were deposited on a highly oriented pyrolytic graphite (HOPG) substrate leading to a full coverage of the latter. The WF values obtained for the nanoplates (see Fig.8) range between 3.9 to 4.35 eV, which are lower that the values shown by the KPFM by around ≈ 0.3 eV. However, this disparity of values is expected when comparing the results from the two techniques[16,22]. For that reason, the WF values from both techniques are considered sufficiently close to be satisfactory.

When comparing the WF maps of the Ag nanoplate with and without illumination in Fig.6 (left) and (right), it can be seen that there is a slight difference between the two images. This difference can be better appreciated on the respective WF histogram plots in Fig.8. Fig.8 (Top left) plots the WF histograms for the same Ag nanoplate with and without illumination. Where the WF shows a clear shift towards lower WF values caused by the laser illumination. By fitting a series of Gaussian functions in both profiles it is possible to find the relative shift of each peak. Which is of the order of ≈20 meV. The illumination also causes a peak at 4.91 eV to vanish while a new peak at 4.36 eV appears.

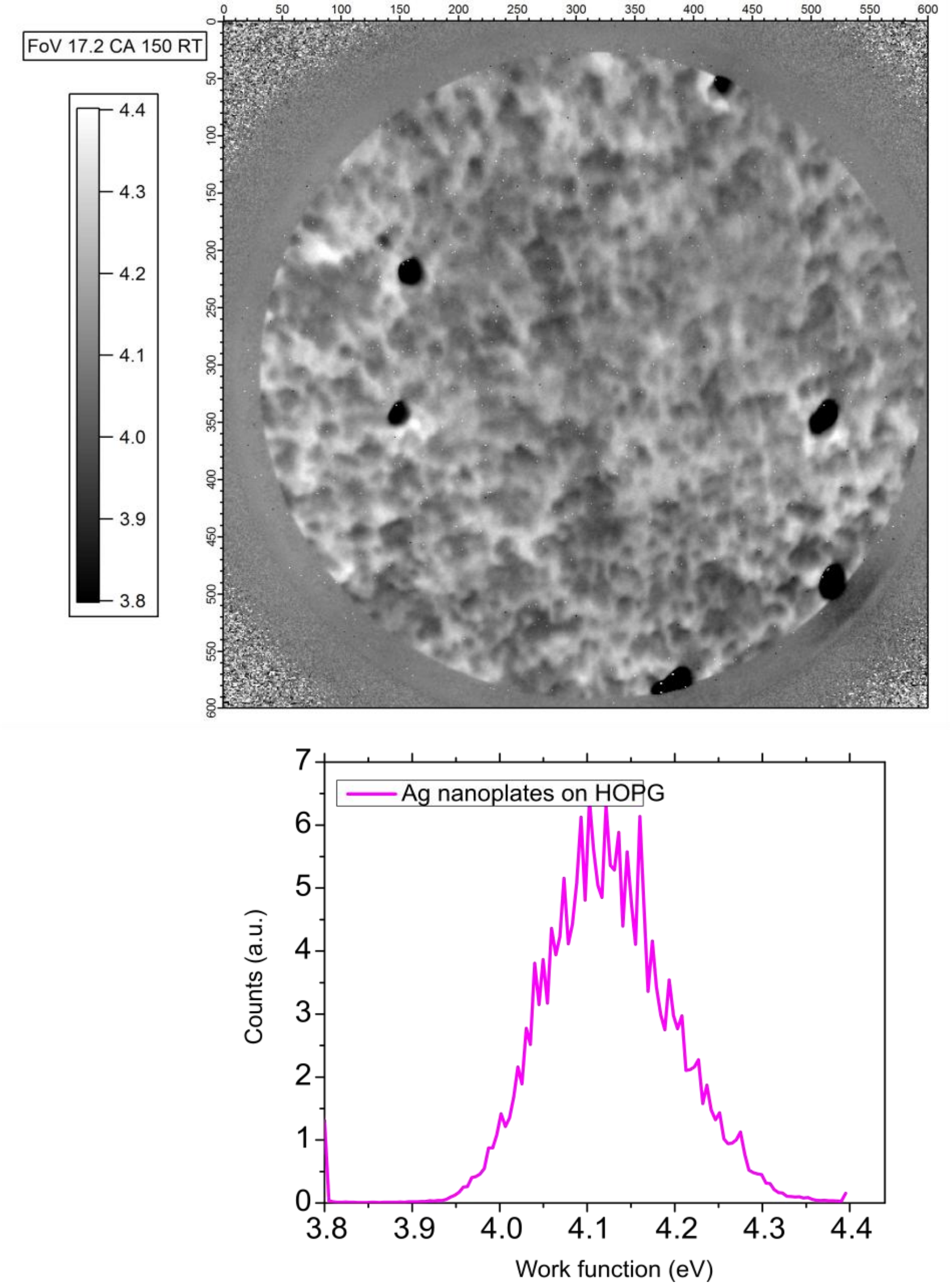

Figure 7: (Top): Work function maps of Ag nanoplates deposited on highly oriented pyrolytic graphite (HOPG) performed with an energy filtered photoelectric electron microscope (EF-PEEM). The field of view is 17 µm. The HOPG is completely covered with Ag nanoplates. This image has been taken and processed by collaborator Mattia Cattelan. (Bottom): WF histogram of the image on top.

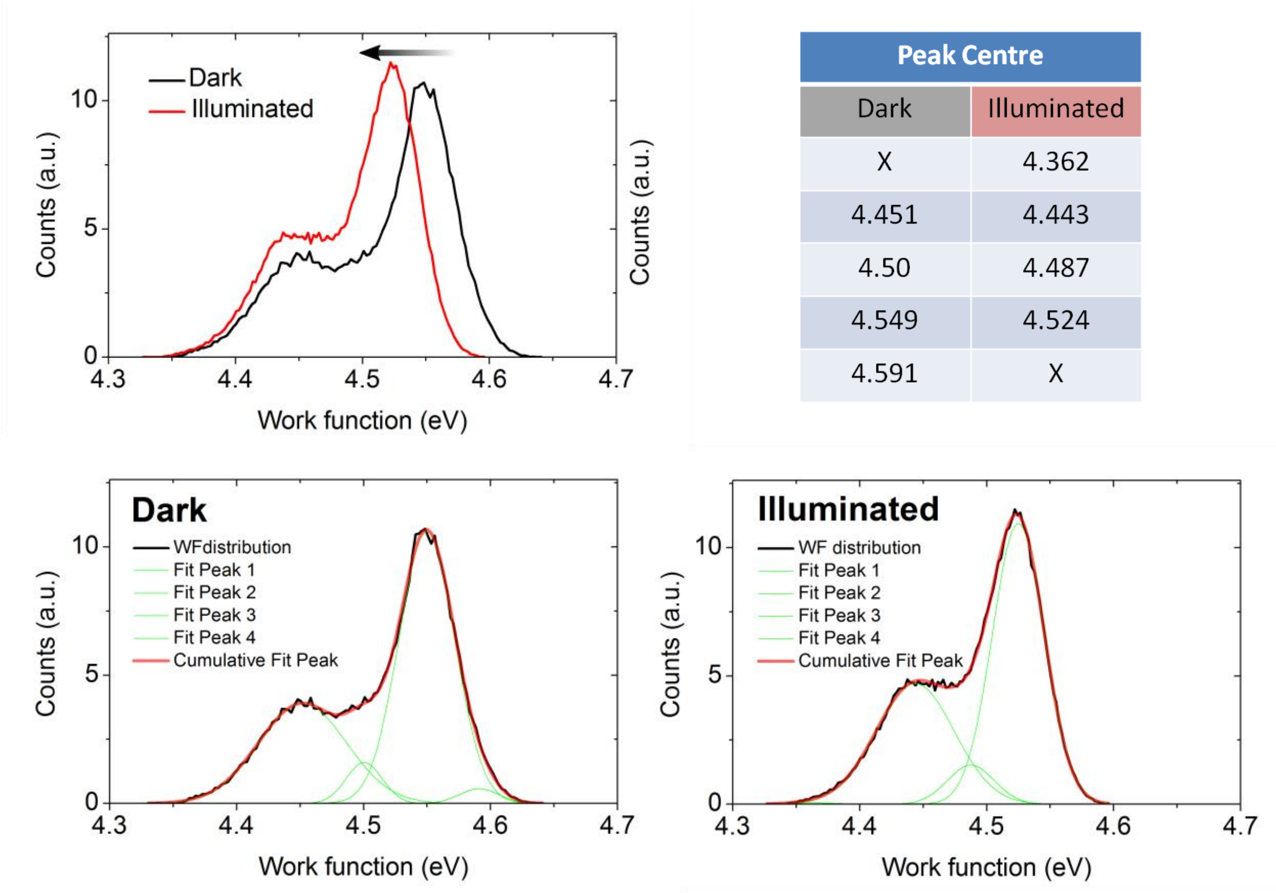

Peak Centre	
Dark	Illuminated
X	4.362
4.451	4.443
4.50	4.487
4.549	4.524
4.591	X

Figure 8: Histograms made from WF maps performed with KPFM shown in Fig.6. (Top left): Work function histogram of an Ag nanoplate on ITO with (red line) and without (black line) illumination. (Top right): Table containing fitted Gaussian peaks to the work function histograms of an Ag nanoplate on ITO with and without illumination. (Bottom left): Gaussian peaks (green lines) fitted to a work function histogram of an Ag nanoplate without illumination (black line). The red line is the cumulative fit peak. (Bottom right): Gaussian peaks (green lines) fitted to a work function histogram of an Ag nanoplate under illumination. The red line is the cumulative fit peak. The histograms are made with data from the top of the Ag nanoplate, so there is no convolution with the ITO substrate.

According to the data plotted in Fig.8 it could be concluded that illumination indeed causes a shift in the WF of the Ag nanoplate towards lower WF. Therefore, a PEP with a magnitude of 20 meV seems to be present. However, the WF peaks on the histograms are very convoluted and this could mean that subtle changes in WF might be overlooked. Therefore, in the next section (Sect 5.3), the WF shift of the Ag nanoplate due to illumination is examined on specific points to determine if the WF shift matches the one described above and its time dependent behaviour.

5.4 Time dependent single point studies of plasmo-electric potentials

5.4.1 Transient behaviour of plasmo-electric potentials

Fig. 9 shows the evolution of the WF shift ($\Delta\phi$) of a representative point on the surface of an Ag nanoplate for different illumination intensities when it is exposed to a cycle of darkness-illumination-darkness. The points chosen for these experiments are located in flat areas of the Ag nanoplate in order to avoid the protuberances likely caused by contamination. Consequently, the data presented in this section corresponds to either PVP-Ag <111> or Ag <111>. The data are normalised to the initial WF value and for the sake of clarity the plotted magnitude is the absolute value of WF change ($|\Delta\phi|$) but the WF shift is actually towards smaller WF values. $\Delta\phi$ is in fact the PEP as this WF or potential variation is plasmon/light driven as it only manifests itself under illumination conditions. As can be seen in Fig.9, once illumination is switched on, $|\Delta\phi|$ starts to increase following an exponential decay trend until it finally saturates reaching a saturation voltage V_{sat}. This saturation voltage is actually the magnitude of the PEP.

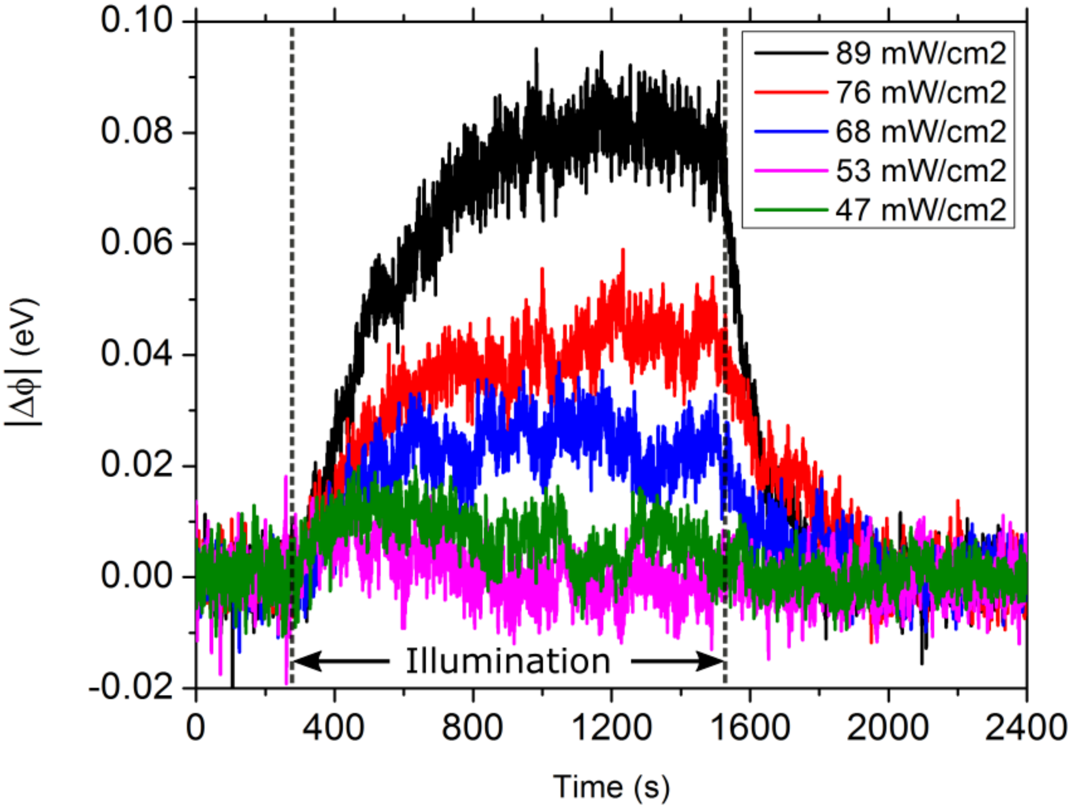

Figure 9: Work function shift transients on a single point on top of the Ag nanoplate for different illumination intensities.

When illumination is switched off, $|\Delta\phi|$ starts decreasing following again an exponential decay trend until it returns to its initial value. When the laser power is 53 mW·cm^{-2} or lower, the V_{sat} is smaller than 10 mV and shows little power dependence. Also the transient curves at such low powers show no clear shape and interpretation of the data becomes difficult. The power dependence and general shape of the transients described above is consistent for all the transient measurements carried out on different Ag nanoplates across the sample.

5.4.2 Power dependence of plasmo-electric potentials on silver nanoplates

Regarding the dependence of the magnitude of PEP with the illumination intensity (I_L), Fig.10 shows a plot of V_{sat} against I_L. The plot shows a strong dependence of PEP with I_L. This reinforces the idea of the light/plasmon driven nature of PEP.

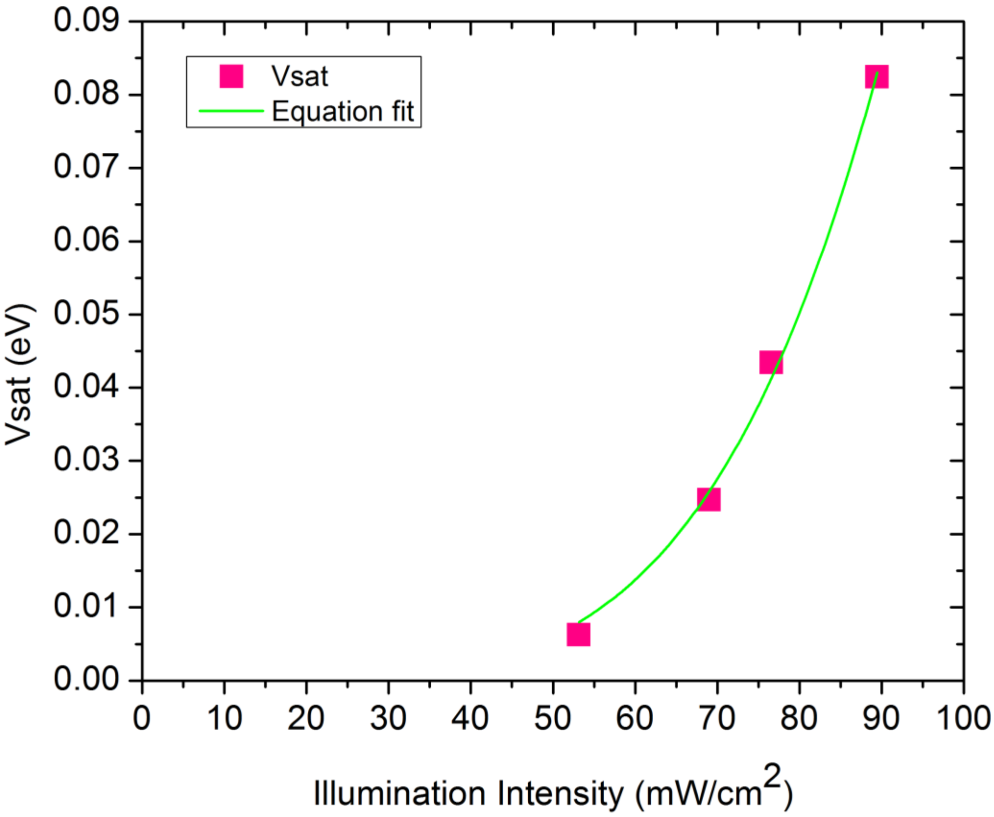

Figure 10: Saturation voltage (V_{sat}) *vs* Illumination intensity (I_L) plot. Green line shows the allometric function fitted to the data represented by pink squares.

An allometric function (Eq.1) was fitted to the V_{sat} data showing that there is a power law dependence with an exponent of B= 4.5.

$$PEP = V_{sat} = A \cdot I_L^B \qquad (5.1)$$

These results are along the lines of those described by Sheldon *et al*[23] who report a power dependence for the PEP. Moreover, the theory of PEP developed by van der Groep *et al*[3] links this dependence to the thermal equilibrium conditions - balance between heat input by the laser and the heat loss by radiation - that occur at different particle temperatures. According to his theory, the PEP for different powers increases rapidly at low powers to then reach a plateau. However, in our case, that behaviour was not seen. This could be because the investigated range of powers was not wide enough to reveal the plateau.

5.4.3 Time constants for the activation and relaxation of plasmo-electric potentials

Upon examination of the PEP transient plots in Fig.9, what immediately stands out is the fact that the time constants for the 'activation' (τ_{ON}) and 'relaxation' (τ_{OFF}) of PEP are surprisingly long for a plasmonic driven phenomenon. Plasmons activate and decay in femtoseconds[24], and the plasmon induced hot carrier generation is a process that operates on the same time scale[25]. Therefore, one would expect the PEP to behave similarly or at least with a delay in line with the timescales mentioned above. Nevertheless, the τ_{ON} for PEP is of the order of hundreds of seconds.

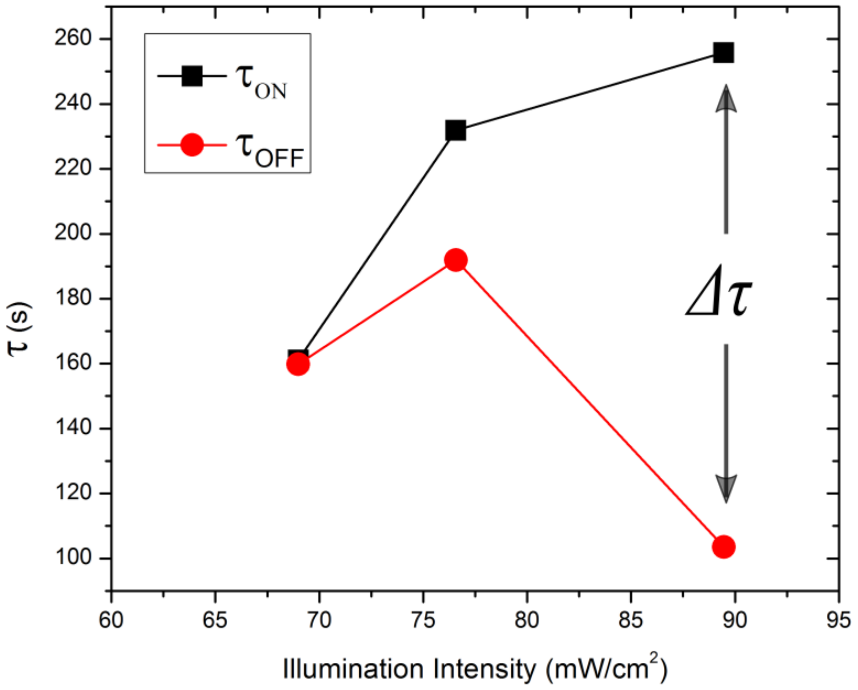

Figure 11: Time constant *vs* Illumination intensity plot. The black squares represent the activation time constants (τ_{ON}) and the red squares represent the relaxation time constants (τ_{OFF}).

In Fig.11 we can see the evolution of τ_{ON} with I_L where it shows a positive dependence. The PEP 'relaxation' time (τ_{OFF}), although it initially shows a positive dependence, it decreases in its values obtained for higher intensities. Nonetheless, its values are still over a 100 s. Far from the time regime expected for a plasmon driven effect. Values of τ_{ON} and τ_{OFF} for intensities below 65 mW/cm^2 could not be extracted from the transient data due to not being able to fit the capacitor model to the data.

It is also observed in Fig.11 that τ_{OFF} is consistently lower than τ_{ON} for all illumination intensity values, which can also be appreciated in Fig.9 where the transients have an asymmetric shape. Furthermore, the difference between activation and relaxation time constants $\Delta\tau$ increases with higher illumination intensities. This behaviour is consistent in all the measurements that were performed for this study. The behaviour of τ_{ON} and τ_{OFF}, could in some way indicate that the PEP, although an outcome of plasmonic excitation, is not a direct consequence of it.

5.4.4 Temperature dependence of plasmo-electric potentials on silver nanoplates

The examination of the shape and behaviour of the PEP transients presented until now, together with the well known heating effect of plasmonic excitation[26], lead us to consider that PEP might have been caused by a local temperature increment on the nanoplate. To support this theory, is worth mentioning that the shift of WF due to temperature changes has been widely reported in the past[27–30]. Moreover, the increase of V_{sat} with increasing laser powers agrees with this hypothesis; because higher laser power implies a higher temperature achieved on the nanoplate, and therefore a greater WF shift.

However, the fact that the τ_{OFF} decreases when laser power is increased, seems to contradict the temperature hypothesis. A higher laser power would produce a higher temperature which means a larger amount of thermal energy stored on the nanoplate. In addition, if the dissipation of thermal energy is done through the same Ag nanoplate-PVP-ITO interface and assuming a constant contact thermal resistance, the heat dissipation rate should be constant. Therefore, the larger the amount of stored energy the more time it will take to dissipate. Yet the data in Fig.11 shows the opposite behaviour.

As a consequence of this conundrum, the PEP transient was measured at different initial temperatures; ranging from room temperature to 80K. The experiment followed the same methodology described previously in sect.5.1.2. The sampling point was kept constant on the same nanoplate during this experiment for all the temperature range. Starting at room temperature and after an initial transient measurement for the reference, the sample was cooled down and stabilised in darkness conditions. Then another transient measurement would follow and so on, for all the range of temperatures tested. All measurements were performed at an I_L= 89 mW/cm^2. The execution of this experiment proved to be quite challenging due to the continuous thermal drift of the sample. It was required to scan the sample continuously at high speed in order to follow an specific Ag nanoplate. In addition, as the sample cools down it was necessary to periodically retune the cantilever as its resonant frequency changed with the decreasing temperatures.

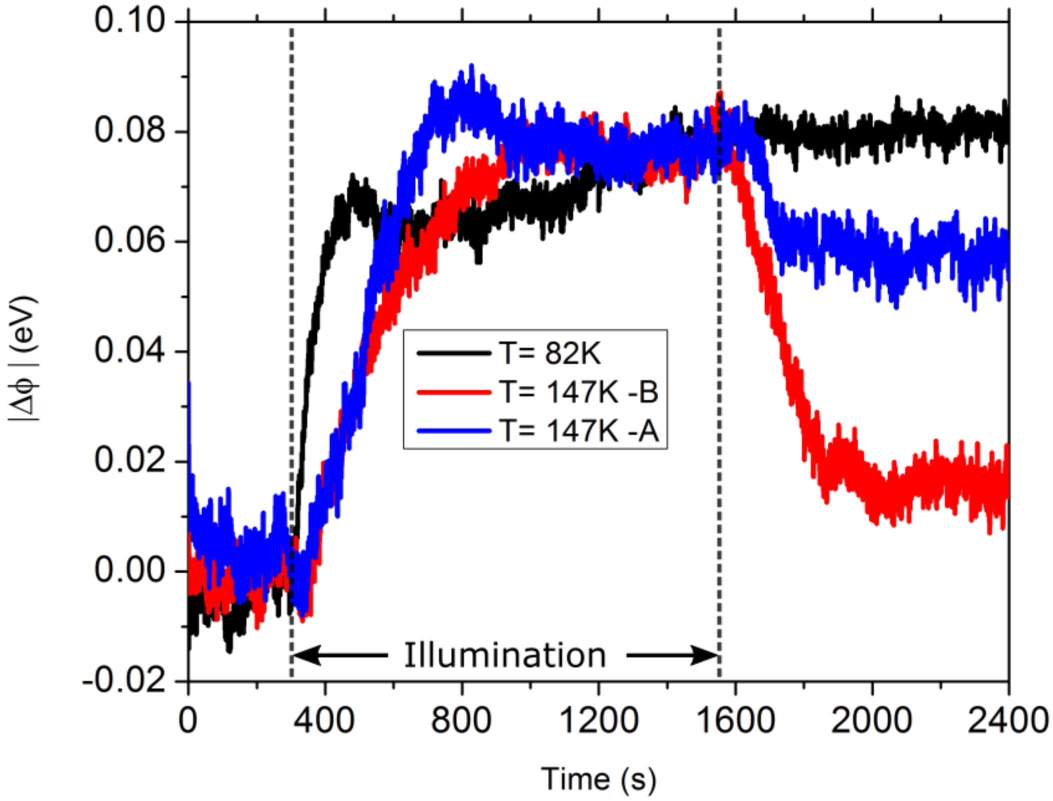

Figure 12: Work function shift transients on a single point on top of a Ag nanoplate at different temperatures for a constant illumination intensity of I_L = 89 mW/cm^2.

The results from the transient experiments at low temperatures are plotted in Fig.12. The first conclusion that can be extracted from the data is that, even at low temperatures, PEP are still present. However, due to the thermal drift problem mentioned earlier, the amount of information that can be extracted from the low temperature data is limited. Nevertheless, from Fig.12

(T=147K -B) it can be calculated that $V_{\text{sat LT}}$ = 0.0785 eV for low temperatures. This is very close to the value for room temperature $V_{\text{sat RT}}$ = 0.0824 eV. With a variation of just ΔV_{sat} = 4 meV, that could be considered negligible. Moreover, the transient for T = 147 K, (147k -B) plotted in solid red line, shows that the activation time constant $\tau_{\text{ON LT}}$ = 223 s is also similar to that of room temperature $\tau_{\text{ON RT}}$ = 255 s. Also, τ_{OFF} is as well smaller than τ_{ON} causing an asymmetry on the transient just like the room temperature case.

The thermal equilibrium of the system at low temperatures is different than that at room temperature. So if the PEP are caused by a temperature increase and the initial temperature of the Ag nanoplate is ≈200 K lower, it should cause an appreciable increase of the activation time constant τ_{ON}. But that effect appears to be absent. Furthermore, the low temperature of the substrate increases the amount of heat lost through the Ag nanoplate-PVP-ITO due to heat conduction. And if we take into account that the energy input to the nanoplate is the same as at room temperature, the temperature achieved by Ag nanoplate should be lower than at room temperature. This would cause the PEP at low temperatures to be of lower magnitude that that at room temperature if the temperature hypothesis was to be correct. But again, this effect wasn't observed.

Therefore, if PEP was a pure temperature driven phenomenon, its magnitude at low temperatures should be lower and its activation time constants higher. Consequently, according to the data collected at low temperatures, the temperature does not appear to influence or be the ultimate cause of the PEP.

5.4.5 Thermal simulations of silver nanoplates on ITO

Despite the conclusions of the previous section, the laser heating of a system of Ag nanoplates on ITO was simulated by finite element analysis to find out if the thermal transient of the nanoplates was similar to the PEP transient. Such an analysis could indicate a possible relationship. The simulation included an Ag nanoplate capped by PVP over an ITO substrate heated by a laser beam with the same characteristics and incident angle as the one used on the transient experiments.

The initial thermal simulations of an Ag nanoparticle in contact with an ITO substrate showed that both heating and cooling transients would take place in less than a second. That is, the heating and cooling were nearly instantaneous. This would mean that, according to the simulation, the thermal barrier between nanoplate and substrate has to be very high in order to cause a transient as slow as seen experimentally considering conduction as the most relevant heat loss mechanism for this system.

In view of the results of the first simulation, a second simulation was done but this time the nanoplate was separated from the substrate and was isolated in free space without any physical contact with any object. The intention of the second simulation was to mimic the worst possible scenario with an infinite thermal barrier between nanoplate and substrate and check if the transients could be reproduced. The only mechanism of heat loss for the nanoplate in this situation is radiation, and its magnitude depends directly on the value of the emissivity ε. Hence, under these assumptions a number of simulations were carried out varying the emissivity of the Ag in order to reproduce the experimental data. The results are shown in Fig.13 where the temperature of the Ag nanoplate is plotted for different cases.

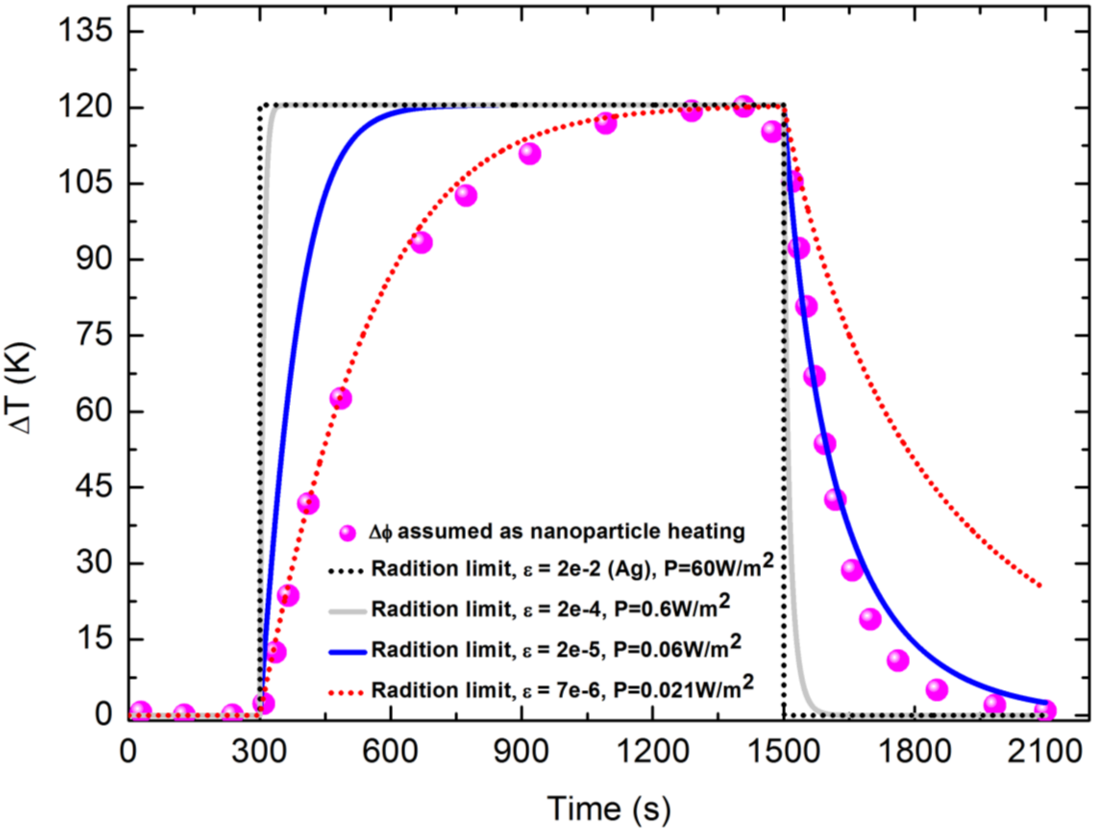

Figure 13: Finite element analysis simulation of the thermal transient for a laser heated Ag nanoplate suspended on free space for different emissivity (ε) values. The temperature refers to the temperature of the Ag nanoplate. (Pink spheres): assumed thermal transient normalised and calibrated from experimental PEP transient data for I_L = 89 mW/cm^2. (Black dotted line): simulated transient for ε = 0.02. (Grey solid line): simulated transient for ε = 2×10^{-4}. (Blue solid line): simulated transient for ε = 2×10^{-5}. (Red dotted line): simulated transient for ε = 2×10^{-6}. This simulation has been carried out by collaborator Julian Anaya Calvo.

The pink spheres on the plot of Fig.13 represent the hypothetical temperature transient for the Ag nanoplate. This transient assumes the same shape than that for the PEP at I_L= 89 mW/cm^2. The maximum temperature achieved by the transient has been calibrated with WF measurements at elevated temperatures carried out in the nanoESCA intrument (see Ch2 sect.2.4.1). According to which a temperature of $T \approx 120°\text{C}$ would cause a $\Delta\phi \approx 0.9$ eV (data not shown).

The black dotted line represents the thermal transient for the Ag nanoplate with the typical Ag emissivity[31] $\varepsilon = 0.02$. As the plot shows the transient is extremely fast and very different from the experimental transient. This is reasonable because the mass of the nanoplate is very small and has almost no thermal inertia so it can be heated really fast. Furthermore, the surface/volume ratio is very high for the nanoplate which favours the radiation heat loss.

If we try to find the emissivity that would reproduce the cooling transient time constant (blue line), the emissivity has to be as low as $\varepsilon = 2\times10^{-5}$. And if we wanted to reproduce the heating transient (red dotted line) it would be necessary to use an emissivity of $\varepsilon = 7 \times 10^{-6}$. Therefore, it is not possible to reproduce the heating and cooling transients with the same emissivity. Furthermore, the values needed to reproduce either of the transients are so low that they are not physically possible. Consequently, we can conclude that according to the thermal simulations explained above, the PEP transients cannot be caused by a temperature transient due to the laser heating of the Ag nanoplate.

5.4.6 Work function shift transients on ITO

In order to assess how the ITO substrate can be affected by PEP generated in the Ag nanoplates, single point WF shift transient measurements were performed on ITO. It should be noted that ITO is a semiconductor that does not support plasmons in the wavelength range of the laser used for the experiments presented here. Therefore, it is not possible to generate PEP on ITO with our current setup. This is the reason why in this section the $|\Delta\phi|$ represents just WF shift on ITO and not a PEP.

Two samples were used for this experiment: one sample of ITO substrate with Ag nanoplates deposited on it and another sample of bare ITO with no nanoplates. On the former sample, the sampling point was chosen so that it was equidistant from all the surrounding Ag nanoplates by at least 300 nm. On the latter sample, the sampling point was chosen at random.

Fig.14 shows the WF shift transients measured on top of ITO for different laser powers on the two samples described above. We only plot the curves for illumination intensities of 89 mW/cm^2 and 76 mW/cm^2 as they are the most representative. The Fig.14 (Top) plots the $|\Delta\phi|$ for ITO on a bare ITO sample whereas Fig.14 (Bottom) plots the same but for a sample that has Ag nanoplates on ITO. The WF variations seen on Fig.14 (Top) can be attributed to the random drift of the

KPFM probe or to random electrical noise. However, in Fig.13 (Bottom) we can see two distinctive sets of peaks right after activation and deactivation of the illumination over the sample.

Immediately after the activation of the laser, the WF changes quickly to then return to its initial value despite the illumination being still active. The same effect is observed upon deactivation of the illumination. These peaks are present for the 100% and 75% power curves and appear to have a shorter activation time when compared with the Ag nanoplate transients. The fact that the WF shift on ITO only occurs when Ag nanoplates are present and when there is a change in illumination suggest that this WF shift is caused by one of the effects associated with plasmonic excitation on nanoparticles. Namely, intense localised electric fields, hot carrier generation, localised heating or PEP.

Regarding the localised heating hypothesis, if this was the case, it could be assumed that the first peak is caused by a sudden change of temperature which in turn changes the WF. However, it doesn't explain why the WF decreases after the initial rise. If it was purely a thermal effect, the WF shift should be maintained during the illumination period.

Concerning hot carrier generation, it is possible to make the same reasoning as for the localised heating. The hot carrier generation is constant with illumination. So its effects over the ITO should be constant as well, as long as illumination is active.

If localised electric fields are examined as the possible explanation, it is possible to argue that the intense fields created on the nanoplates attract charge carriers from the ITO bulk towards the surface producing a band bending that shifts the WF. This mechanism would act as sort of a "surface bias". However, the electric fields on the nanoplates are constant while the illumination is present. So, the effects of the "surface bias" - the WF shift- should be constant as well. But this is not the case. Thus, it is probable that localised electric fields alone are not the cause for observed shift.

Connecting the behaviour of the ITO to PEP seems a bit premature at this point, as the nature of the PEP transient is still not clear. But this matter will be discussed again later in the chapter once the causes of the PEP transients have been elucidated.

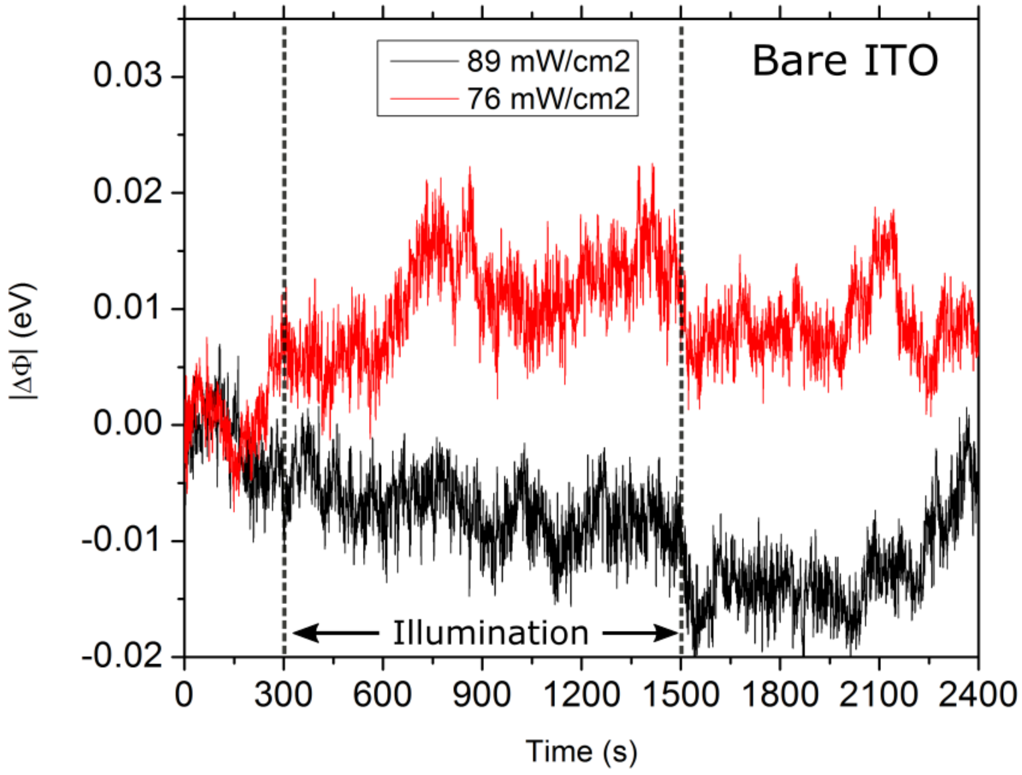

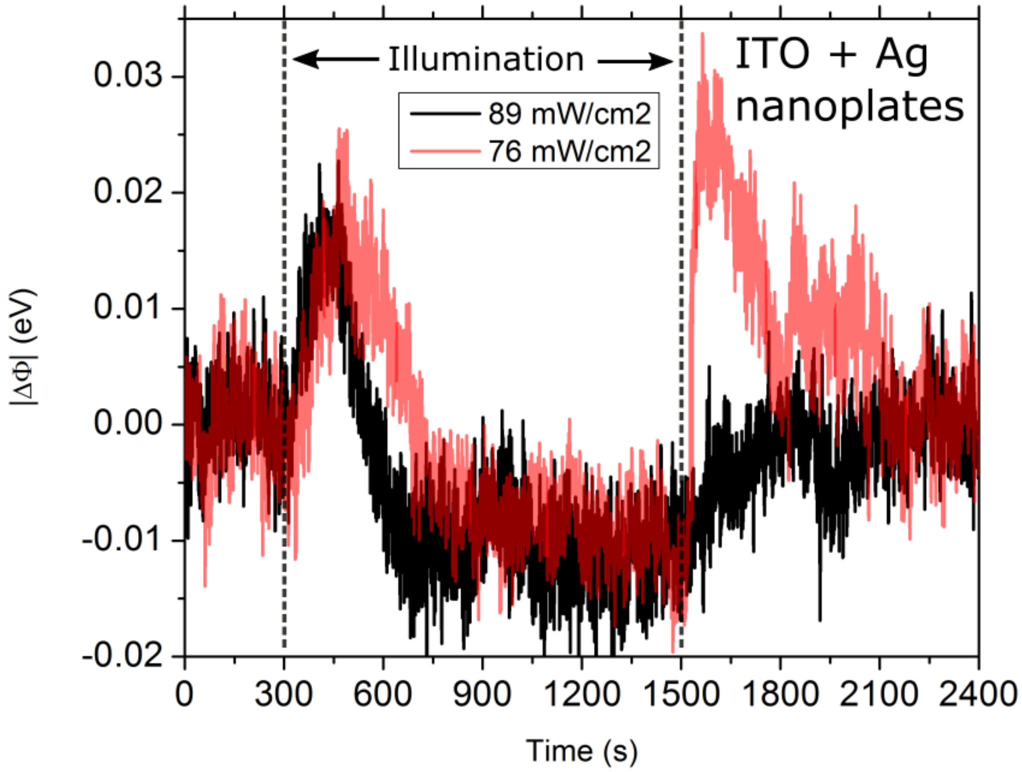

Figure 14: Work function shift transients on a single point of ITO carried out with KPFM. (Top): On a sample of bare ITO. (Bottom): On a sample of ITO with deposited Ag nanoplates surrounding the sampling point.

5.4.7 Tip repulsion effects during plasmo-electric potentials measurements

During the PEP transient measurements performed with KPFM, it was observed that the height of the tip of the cantilever would increase during the illumination period to return to its original height once the laser had been switched off. This height shift would be slow, taking several minutes. The height shift turned out to be a function of the laser power density. So that increasing power densities produce an increase in the height shift.

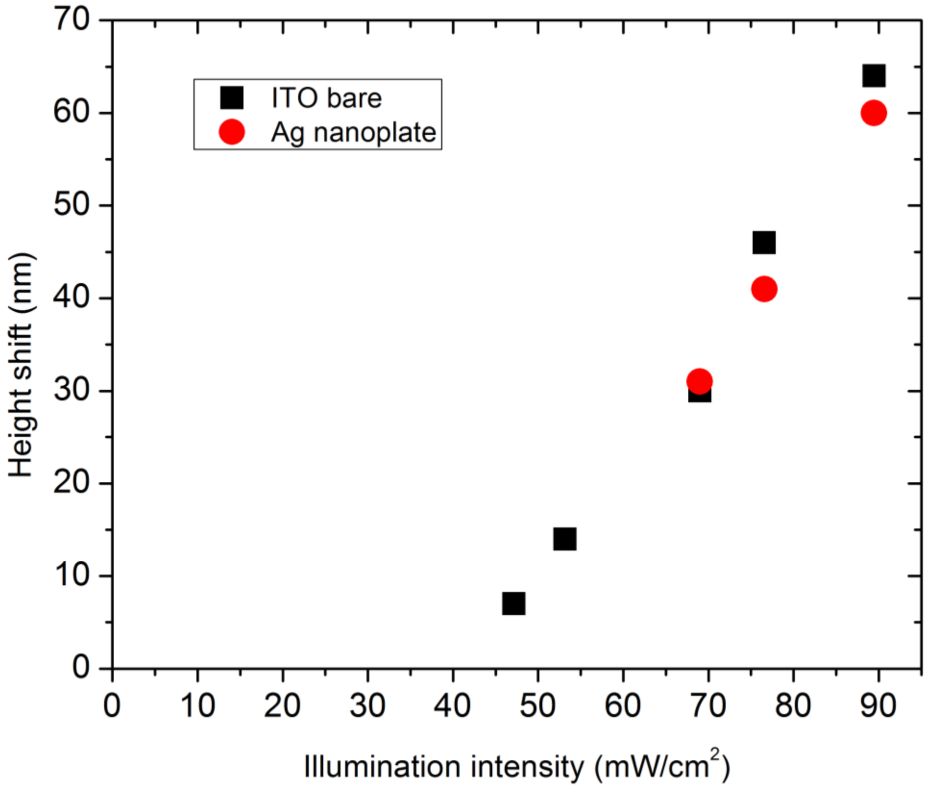

Figure 15: KPFM tip height shift against illumination intensity plot. (Black squares): Height shift on top of bare ITO. (Red circles): Height shift on top of an Ag nanoplate.

In Fig.15 are plotted the height shifts for different illumination intensities for two cases: tip above ITO on a bare ITO substrate (not plasmonic) and tip above a Ag nanoplate (plasmonic) on an ITO substrate. As it can be seen on the plot, the height shift follows the same trend and has approximately the same magnitude in both cases, on top of a plasmonic particle and on top of a non plasmonic substrate. Consequently, the height shift experienced by the tip of the cantilever cannot be attributed to a plasmonic effect or be related to PEP. The causes of this behaviour to remain unknown and are out of the scope of this study once it was confirmed that there is no relation with the PEP.

5.5 Plasmo-electric potential transient model

5.5.1 Discussion about the nature of plasmo-electric potentials: Factors influencing the work function

In view of the data presented up until now, it seems that the WF shift of Ag nanoplates under illumination or PEP is indeed a light/plasmon driven phenomenon. Now we present a critical discussion of the factors that influence WF that could be responsible for observed experimental results. The expression for the WF can be written in the following form according to Lang & Kohn[32]:

$$\phi = \phi(\infty) - \mu \qquad (5.2)$$

or

$$\phi = \Delta\phi - \bar{\mu} \qquad (5.3)$$

where ϕ is the WF, $\Delta\phi$ is the change in electrostatic potential across the surface dipole layer created by the spillage of electrons at the surface, $\phi(\infty)$ is the potential of an electron in vacuum, μ is the electrochemical potential and $\bar{\mu}$ is the chemical potential. From these relations the chemical potential may be expressed as:

$$\bar{\mu} = \mu - \phi(-\infty) \qquad (5.4)$$

where $\phi(-\infty)$ is the potential of an electron deep in the bulk or the mean interior potential. See Fig.16 below, for a diagram of all these magnitudes.

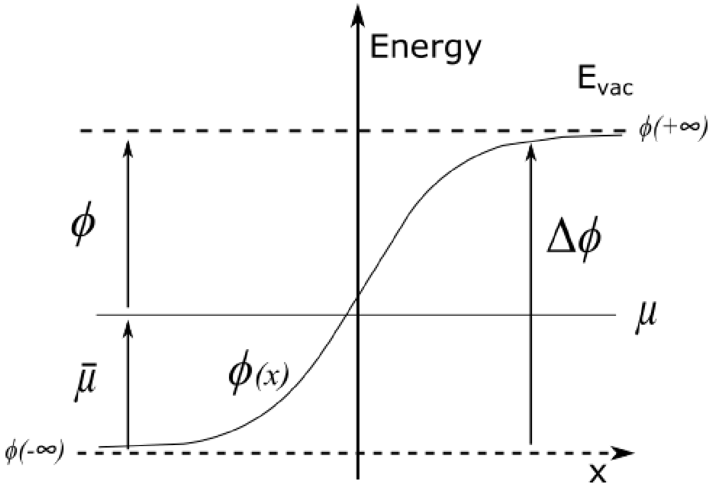

Figure 16: Plot of the electron potential on the interface between a metal and vacuum. The left side of the plot represents the potential of an electron in the bulk ø(-∞) while the right side represents the potential of an electron in vacuum ø(+∞). μ is the electrochemical potential, $\bar{\mu}$ is the chemical potential and ϕ is the WF.

According to the formulae above, the WF has two main components: a surface component $\Delta\phi$ and a "bulk" component also called chemical potential $\bar{\mu}$ which depends on μ. Therefore, any changes in the WF must have its origin in one or both of these factors.

i) The surface component $\Delta\phi$ relates to an electrostatic surface dipole that modifies the WF depending on its magnitude and direction. It is therefore very sensitive to adsorbed atoms or molecules on the surface[33], their surface coverage[34,35] and surface chemical reactions[36].

In our case this surface component could be influenced by a photon stimulated desorption process[37–39] or a thermally stimulated desorption[40,41] that would cause surface atoms or molecules to leave the surface and result in its surface dipole changing. However, this is unlikely to be the reason because even if we assume that the photon stimulated desorption or thermally stimulated desorption does happen; this hypothesis does not explain how the WF is restored to its initial value in such a short time (low value of τ_{OFF}).

If molecules or atoms are desorbed from a surface under UHV conditions, they will most likely adsorb onto the walls of the chamber and not return in the short term. Due to the low pressures it is not possible for them to re-adsorb onto the surface in a matter of minutes. This is related to the molecular flow regime present at UHV pressures and to a concept termed "average time for a monolayer"[42]. This is defined as the average time that would take for atoms/molecules present in a vacuum chamber to form a monolayer on a surface. Under our experimental conditions the average time for a monolayer is longer than 15 h. This makes it unlikely that the recovery of a surface can occur in a matter of a few minutes.

In our case, the Ag nanoplates have a layer of PVP encasing them. So an additional mechanism that could cause a surface dipole change is an interaction of one the PVP bonds with the incoming light that somehow changes its molecular dipole. But, PVP light absorption spectra from FTIR[43,44] does not show absorption at the wavelength used for this study, which supports the idea that there should be no interaction of light with the PVP. Also the time scale of this type of process should be shorter than those we observed.

Light driven stereoisomerisation[45,46] is a process that entails the change of the three dimensional arrangement of a molecule that could lead to a change in the molecular dipole and consequently in the surface dipole. Regarding the formation of an isomer due to light excitation, the author is not aware of any reports on this matter regarding PVP. Moreover, PVP does not have any double bonds that could allow the formation of an isomer. On top of that, Sheldon *et al*[1] reported PEP on Au nanoparticles that are free of a PVP capping layer. In addition, preliminary measurements of

PEP carried out on Au nanorods free of PVP (data not shown) display roughly the same behaviour as the Ag nanoplates. So light driven isomerisation of PVP is not the cause of PEP.

Another possible cause for the change of the surface component could be the intense localised electric field generated by the plasmons. These fields would cause either a localised surface band bending or a rearrangement of the charge density on the surface leading to a change on the surface component. However, if this was the cause the change would be instantaneous due to the high electron mobility of metals . Which does not match with the experimental results.

Therefore, we can conclude that the surface component of the WF is not responsible for the observed transient response.

ii) The chemical potential, $\bar{\mu}$, depends on the electrochemical potential μ according to Eq.4. And the electro chemical potential is the partial derivative of the Helmholtz free energy[27]:

$$\mu = \left.\frac{\partial F}{\partial N}\right|_{T,V} = F(N+1) - F(N) \qquad (5.5)$$

where F is the Helmholtz free energy, N is the number of electrons in the system, T is temperature and V is the volume of the solid. Therefore, μ is a function of temperature (T) and electron number (N). Consequently a change in T or N could contribute to a WF variation.

One of the damping mechanisms for plasmonic processes is the creation of hot carriers[25] that in turn decay by electron-electron and electron-phonon interactions[25,47]. This decay ultimately leads to an energy transfer from the hot carriers to the nanoparticle crystal lattice causing a local increase in the temperature of a nanoparticle[26,48]. It is also well known in the field of surface science that the WF of metals changes with temperature as it has been reported since the 70's [27–30]. Consequently, it is a fair hypothesis that plasmon decaying processes could increase the temperature of the nanoparticle and as a result change its μ and therefore the WF. However, the experiments and simulations shown previously (sect 5.4.4 & 5.4.5) seem to reject this supposition.

Concerning the change of the electrochemical potential due to a variation in the number of electrons of the system N; there could be a sort of electrochemical reduction of the ITO by the Ag which would modify the charge of the Ag nanoplate. But there is a PVP capping layer that should prevent this from happening by avoiding direct contact between nanoplate and substrate. Additionally, this type of reaction should not take place at low temperatures or be extremely slow. As usually chemical reaction kinetics have a strong dependence on the temperature of the environment[49,50], but this contradicts the results of our experiments at low temperature (see sect 5.4.4).

Examining the PEP transient data in Fig.9, it is possible to infer that the time scales of the PEP are relatively long because they could be related to a transport process of some sort with a limited transport rate. The two main transport processes that can be occurring on the Ag nanoplate-PVP-ITO system are either heat transport or charge transport. Heat transport is indeed occurring but temperature has already been discarded above as the cause for PEP. Therefore, it seems the PEP transients are possibly caused by a charge transport phenomena.

Consequently, for the reasons presented above, the following can be concluded:

The WF variation of Ag nanoplates under laser illumination detected on the transient experiments; must be caused by a temperature independent, plasmon driven charge transfer from the substrate to the nanoplate or *vice versa*. This causes a charge accumulation or depletion that modifies the electrochemical potential on the Ag nanoplate and in turn its WF.

This conclusion chimes with the explanation proposed by van der Groep *et al*[3] regarding charge being the cause of the μ shift.

NOTE: As an aside, it is worth mentioning that the electrochemical potential μ is often assigned the same value as the Fermi energy level E_F. But, they are in fact of different magnitudes. A brief explanation of these two quantities will follow in order to clarify the matter and avoid any confusion. The subsequent analysis is for metals as semiconductors require a different approach.

The electrochemical potential has already been defined and the E_F is equal to[51]:

$$E_F = \frac{50.1\ eV}{\left({}^{r_s}/_{a_o}\right)^2} \qquad (5.6)$$

where r_s is a measure of electronic density, and a_0 is the Bohr radius. E_F and μ have the same value at $T = 0$ K, so that:

$$\lim_{T \to 0} \mu = E_F \qquad (5.7)$$

However, they diverge at higher temperatures, $T > 0$ following the expression:

$$\mu = E_F \left[1 - \frac{1}{3}\left(\frac{\pi k_B T}{2E_F}\right)^2\right] \qquad (5.8)$$

Fortunately, this divergence is only relevant at very high temperatures $T > 10^4$ K. And at room temperature the difference between these two magnitudes is around 0.01%[51]. Therefore, although in the range of temperatures of this study it is possible to use E_F and μ indistinguishably, it is sensible to know their differences.

5.5.2 Capacitor model

In order to clarify the PEP transients and taking into account the conclusions of the previous sections, the following model is proposed:

When a LSP is excited on a metallic nanoparticle deposited on a semiconductor substrate *via* light excitation, it causes charge to be transported through the nanoparticle-semiconductor interface following an exponential decay trend. This process continues until a saturation point is reached where the charge of the nanoparticle Q_n is no longer neutral.

$$Q_n = Q_{sat} = N_{sat} - N_o \neq 0 \Rightarrow N_{sat} \neq N_o \qquad (5.9)$$

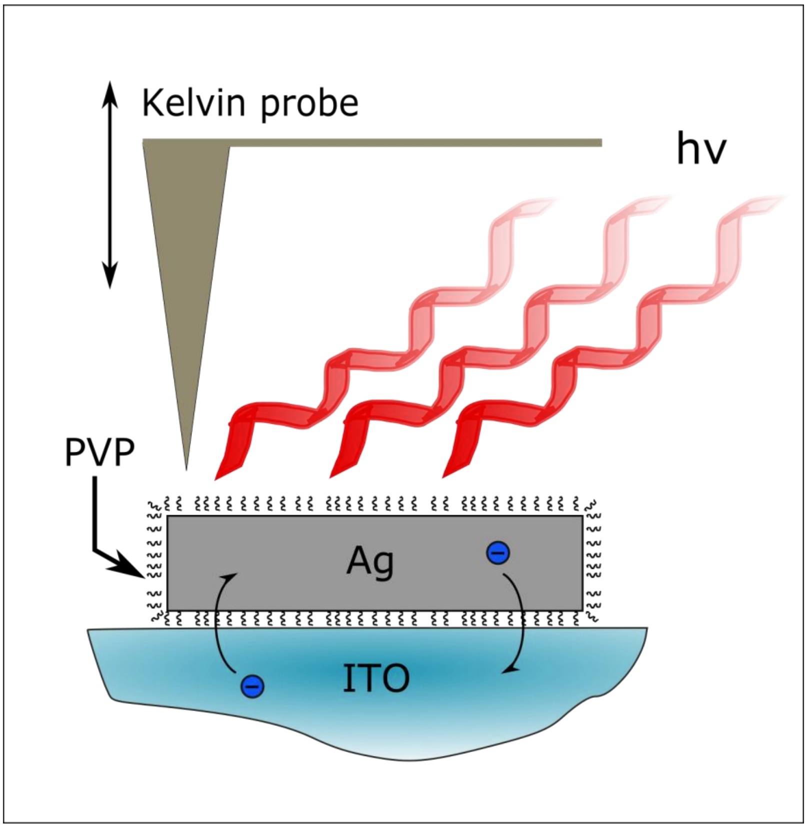

Figure 17: Diagram of the light driven charge transfer process on the Ag nanoplate-PVP-ITO system.

This additional charge Q_{sat} shifts the electrochemical potential μ of the nanoparticle and in consequence its WF. When the light excitation is deactivated, the LSP disappears and the nanoparticle-substrate system, now in an out-of-equilibrium state due to an excess of charge on the nanoparticle ($Q_n \neq 0$), returns to the initial uncharged state by expelling the redundant charge back to the substrate by Coulomb repulsion. As a result, the nanoparticle-semiconductor system behaves effectively like a nanocapacitor (NC).

In this process, the substrate operates as an electron reservoir for the nanoparticle. In the particular case that is being studied here, the dimensions of the substrate are much larger in comparison with the nanoparticle. Thus the substrate is not affected by the electron transfer with the same intensity as the nanoparticle. For this study the substrate was always connected to ground so any substantial charge imbalance on the substrate would quickly be eliminated by expelling or drawing charge to ground.

By assuming that the system behaves like a NC, it is possible to perform a more in depth analysis of PEP transients and the factors that might influence them. Our system consists on an Ag nanoplate separated from the ITO substrate by a thin layer of PVP. Hence, we can consider the nanoplate to be one of the plates of the NC, the ITO substrate to be the counter plate while the PVP would be the dielectric between the plates. The Ag nanoplate would charge through the PVP layer so we can approximate our case to that of a typical RC circuit where there is a capacitor in series with a resistor. Then we can use the formula for the time dependent voltage of a charging (Eq.5.10) and discharging (Eq.5.11) RC circuit[52]:

$$V_{ON}(t) = V_{sat}\left(1 - e^{-\frac{t}{\tau_{ON}}}\right) \qquad (5.10)$$

$$V_{OFF}(t) = V_{sat}\, e^{-\frac{t}{\tau_{OFF}}} \qquad (5.11)$$

$$\tau = RC \qquad (5.12)$$

where $V(t)$ is the time dependent voltage between the plates, V_{sat} is the voltage across the resistor or saturation voltage, R the resistance of the Ag nanoplate-PVP-ITO junction, C the capacitance of the system and $\tau = RC$ is the time constant that indicates the time required to charge/discharge a capacitor up to 63.2% of its initial value. The subscripts 'ON' and 'OFF' represent the "activation" (laser ON, $300 < t < 1500$s) and the "relaxation" (laser OFF, $1500 < t < 2400$s) parts of the transient curve. When these equations are applied to the system, $V(t)$ represents the time dependent PEP $V_{PEP}(t)$ and V_{sat} the final magnitude of the PEP.

Fig.18 shows the PEP transient of an Ag nanoplate under an illumination intensity of 89 mW/cm^2 fitted with Eq.5.10 and 5.11. The equations fit closely the transient data and allows the extraction of the parameters V_{sat}, τ_{ON} and τ_{OFF} used for the elaboration of Fig.10 and Fig.11. The same procedure was used with transients at different illumination intensities with equally successful results. Therefore, it is possible to confirm the validity of the model.

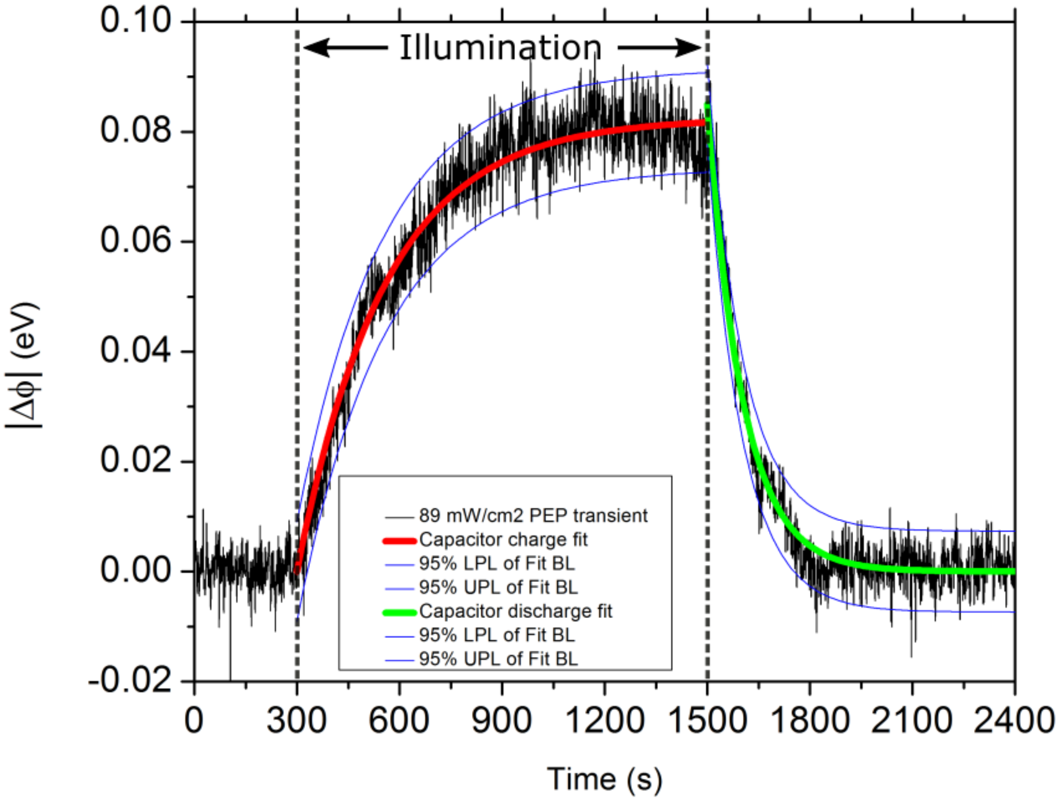

Figure 18: PEP transient plot of an Ag nanoplate on ITO. (Black): Transient data. (Red line): Fit of Eq.10 to the activation part of the transient. (Green line): Fit of Eq.11 to the relaxation part of the transient. (Blue thin lines): Confidence intervals of the fittings.

5.5.3 Capacitance of the silver nanoplate-PVP-ITO system

We can determine the theoretical value for the capacitance of our NC by applying:

$$C = \varepsilon_r \varepsilon_o \frac{A_{plate}}{d_{gap}} \qquad (5.13)$$

$$C = \frac{Q}{V} \qquad (5.14)$$

where C is the capacitance of the NC in Farads, $\varepsilon_r(\mathrm{f}=0)$ is the relative permittivity of PVP for a frequency of 0 Hz, $\varepsilon_o = 8.854187817 \times 10^{-12}$ F/m is the vacuum permittivity, A_{plate} is the area of the plate in m^2 and d_{gap} the distance in meters between the Ag nanoplate and the ITO substrate. For PVP $\varepsilon_r(f=0)$ has reported values of[53] $\varepsilon_r = 2.37$ and[54] $\varepsilon_r = 3$. So an intermediate value of $\varepsilon_r(f=0) \approx 2.7$ was chosen to perform the calculations.

In Fig.19 are plotted the capacitance values of the Ag nanoplate-PVP-ITO system for a range of different gaps calculated using Eq.5.13. If we assume a gap of $d_{\mathrm{gap}} \approx 1.5$ nm, the values of the capacitance for our system are around $C \approx 3.5 \times 10^{-16}$ F.

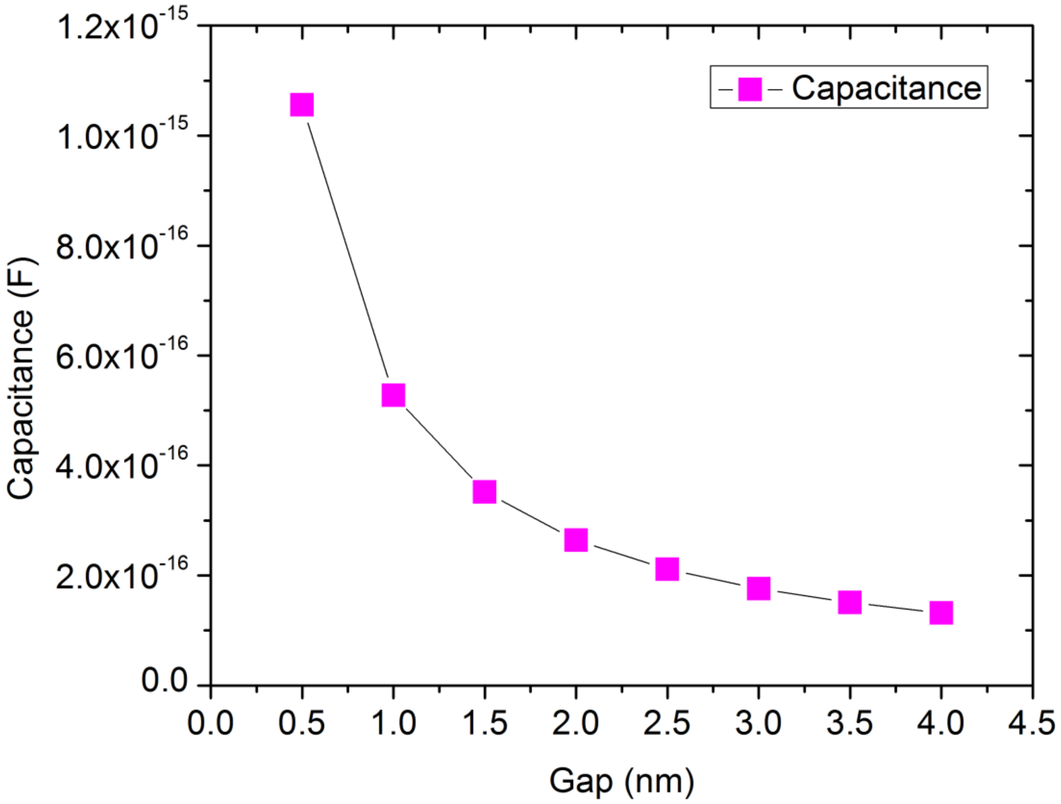

Figure 19: Capacitance values for the Ag nanoplate-PVP-ITO system for various gap distances calculated using Eq.13.

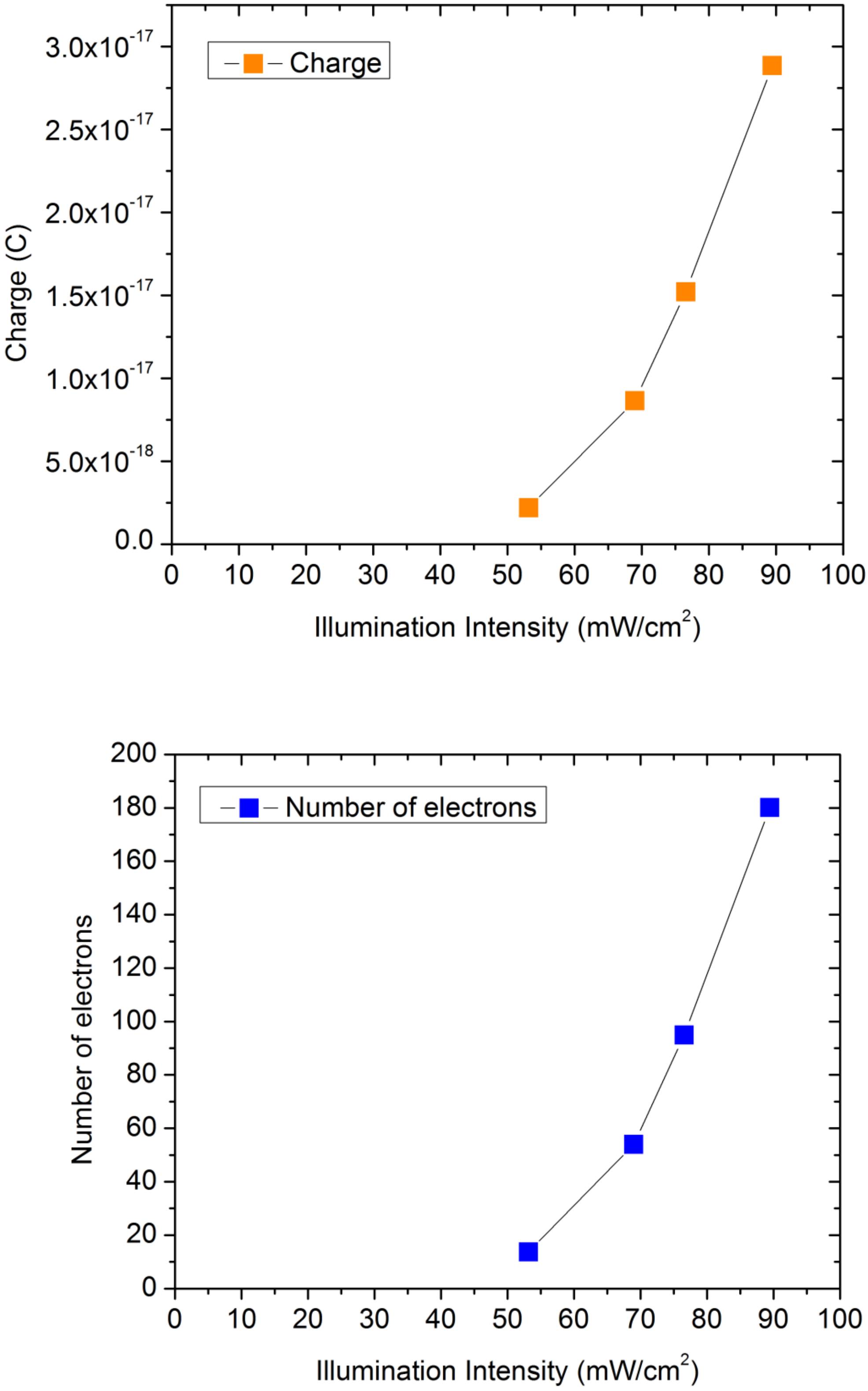

Figure 20: (Top): Charge transferred to/from the Ag nanoplate depending on illumination intensity. (Bottom): Number of electrons transferred to/from the Ag nanoplate depending on illumination intensity.

A consequence of a very small capacitance is that only a small amount of charge is needed to charge the capacitor (Eq.5.14). In our case, if we take into account the experimental value of the saturating voltage of the NC (V_{sat}) and the capacitance C, it is possible to estimate the accumulated/depleted charge or the number of electrons transferred to/from the nanoplate. Fig.20 (Top) shows the number of electrons transferred to/from the nanoplate for different illumination conditions. If the accumulated/depleted charge on the nanoplate is divided by the electron charge we find the number of electrons transferred to the nanoplate. Fig.20 (Bottom) plots the number of electrons transferred to the nanoplate that cause the PEP.

In this case, the number of electrons transferred to/from the Ag nanoplate sits below 200. This contrasts with the numbers reported by van der Groep *et al*[3] on their calculations, where they predicted the transfer of approximately eight electrons for particles with a diameter of around 200 nm. However, the systems and conditions in both studies are different which might be the cause for the discrepancy. For example, their system has a spherical nanoparticle which means that the contact area between nanoparticle and substrate is orders of magnitude smaller that in our case.

5.5.4 Electric field and energy storage on the Ag nanoplate-PVP-ITO junction

The charge transport process through the Ag nanoplate-PVP-ITO interface triggered by laser illumination causes, once equilibrium has been reached, an accumulation of charges with opposite sign at both sides of the interface. If we assume that this charge is positive in the metal and negative on the semiconductor. For the metal, this charge is concentrated on the superficial layers but for the semiconductor the size of the electron enriched zone depends on the doping level. However, for the sake of simplicity in the following analysis, it is assumed that the charge of the semiconductor is also concentrated on the surface.

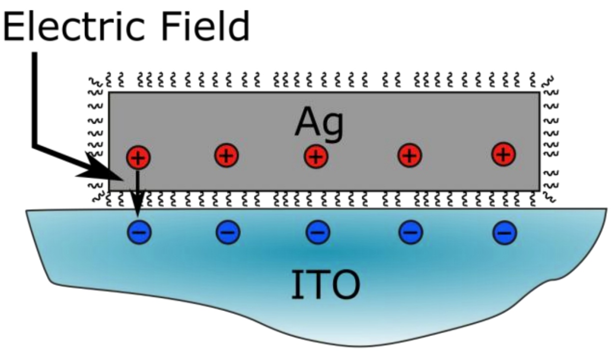

Figure 21: Charge diagram on the Ag nanoplate-PVP-ITO system.

These two charge densities of opposite sign create a strong, constant and highly localised electric field at the interface of the system and more specifically on the PVP region. If we assume that the charge is concentrated in a thin sheet on the surface of the metal and on the interfacial region of the semiconductor, the charge density per unit area ρ in C/m^2 is:

$$\rho = \frac{Q}{A} \qquad (5.15)$$

And the magnitude of the electric field E in V/m for a gap d is:

$$E = \frac{V}{d} \qquad (5.16)$$

For the case of I_L = 89 mW/cm^2 the charge density is $\rho = 1.31 \times 10^{-3}$ C/m^2. Which leads to an electric field of $|E| = 5.5 \times 10^7$ V/m.

Furthermore, one of the applications of capacitors is the storage of energy. In our case, the energy stored on the nanocapacitor is:

$$W = \int_0^Q V(Q)dQ = \frac{1}{2}VC^2 \qquad (5.17)$$

where W in Joules is the energy stored on the capacitor, V is the voltage across the plates and Q is the stored charge in Coulombs. For I_L = 89 mW/cm^2 we obtain a value of $W = 1.44 \times 10^{-17}$ J of stored energy.

5.5.5 Electron transport on the Ag nanoplate-PVP-ITO junction

Knowing the capacitance C of the system it is possible to determine the value of the resistance experienced by the electrons being transferred to the nanoplate as $R = \tau/C$. For an illumination intensity of I_L = 89 mW/cm^2, this renders $R_{ON} \approx \tau_{ON}/C \approx 7.3 \times 10^{17}$ Ω and $R_{OFF} \approx \tau_{OFF}/C \approx 2.96 \times 10^{17}$ Ω for the activation and relaxation transients respectively. In view of these values, two main facts stand out: First, the value of both resistances is significantly higher that the bulk resistivity of PVP ($R_{PVP} \approx 1 \times 10^7$ Ω) and second, they are unequal. The matter of the high resistance will be discussed in the this section while the disparity between their values is addressed in sect.5.5.6 and sect.5.5.7.

The Ag nanoplate-PVP-ITO junction is a case of a thin insulator film between two conductive materials. And provided the film is thin enough and the potential barrier low enough it is possible for electrons to move through the junction *via* quantum tunnelling[55]. If this was the case, it would explain why the resistance values of the junction are significantly higher than the ones expected from bulk PVP.

In order to establish what type of electron transfer mechanism is taking place on the junction, one can examine the conductance of the junction and compare it with the conductance quantum (G_o) [56,57], which is the quantised unit of electrical conductance corresponding to a quantum point contact. If the conductance of a quantum point contact G is equal or less than G_o means that the tunnelling probability is equal or less than 1 and therefore that the electron transport method is indeed quantum tunnelling. If the conductance G is higher that G_o means that the electron transport method is not tunnelling but ballistic conduction or possibly other mechanisms.

The total conductance of a system is the summation of the conductances of all the parallel quantum channels, which in our case would be the PVP molecules: $G=N\,G_{\mathrm{PVP}}$. The problem with this approach is that it assumes that all PVP molecules are perpendicular to the nanoplate and have a connection with nanoplate and substrate. But, in the case of PVP, the capping layer is arranged in a disordered manner[5,58]. This makes the assumption mentioned above incompatible with the observed arrangement. For this reason, the whole Ag nanoplate-PVP-ITO junction was considered as an individual quantum channel in order to facilitate its analysis.

$$G_{gap} = \frac{1}{R_{gap}} = AG_0 \qquad (5.18)$$

$$G_0 = \frac{2e^2}{h} = 7.748 \cdot 10^{-5}\, S \qquad (5.19)$$

The conductance of the junction is expressed in Eq.5.18 as the inverse of the resistance of the gap calculated previously. With G_{gap} being the conductance across the junction, A is a prefactor, G_0 is the conductance quantum, e is the charge of the electron and h is the Plank's constant. The prefactor A is used here as a comparative term between G_{gap} and G_o. When the value of the prefactor is $A > 1$ it means that the conduction across the junction is not tunnelling. Whereas if $A \leq 1$, the probability of an electron crossing the junction is less than 1, meaning that the charge transport is done by quantum tunnelling. In our case, the prefactor has a value of $A \approx 1 \times 10^{-14}$, confirming the tunnelling hypothesis.

Furthermore, tunnelling charge transfer has been reported to result in high apparent resistivity on a number of conductor-insulator-conductor systems with values of the same order of magnitude as the ones reported here[59–63].

Normally, for gap distances over ≈ 0.7 nm, tunnelling should be negligible. But in this case there is a quantum molecular junction so that electrons can travel between particle and substrate through the molecular orbitals of the PVP. The PVP molecules lower the potential barrier for the electrons making possible the electron transport[64].

Quantum tunnelling on plasmonic structures has been widely reported for plasmonic structures such as metal particle dimers[56] and bow tie structures[65]. However, these publications work in the AC regime with charge transfer at high frequencies. In contrast, this study is a case of DC charge transfer as the value of the time constant τ shows. Moreover, some works report charge transfer from substrate to particle on a particle-on-mirror system similar to ours[66,67]. But in their case, the substrate material is a metal that supports plasmon excitation and can be coupled to the nanoparticle on top, which is fundamentally different from our case as the ITO substrate is a semiconductor and does not support plasmons.

5.5.6 Rectification at the Ag nanoplate-PVP-ITO junction

Using the time constant values of the activation and relaxation transients, it is possible to calculate the resistance experienced by the electrons travelling through the Ag-PVP-ITO interface by applying $R_i = \tau_i/C$. Then, by applying Eq.5.22 for $t=0$, it is possible to determine the maximum current during the transient which happens right at the beginning of the curve. Pairing the values of maximum current I_i with their associated saturation voltages $V_{\mathrm{sat}\ i}$ it is possible to build an I/V plot with the current-voltage characteristics of the interface.

$$I_i(t) = \frac{V_{sat\ i}}{R_i} e^{-\frac{t}{\tau_i}} \qquad (5.22)$$

Fig.22 represents the I/V characteristic of the Ag nanoplate-PVP-ITO interface. The points on the negative side of the voltage axis correspond to the activation time constants for different power densities, while the points on the positive side of the voltage axis correspond to the time constants of the relaxation transients at different power densities. The points closer to the vertical zero axis correspond to lower power densities and *vice versa*. Although, for low powers the plot seems fairly symmetric, for high powers there is a discrepancy with the current on the positive side of the voltages being double that on the negative side. This behaviour resembles in some ways that of a rectifying junction. This, ideally, allows current to flow in one direction but not in the opposite one.

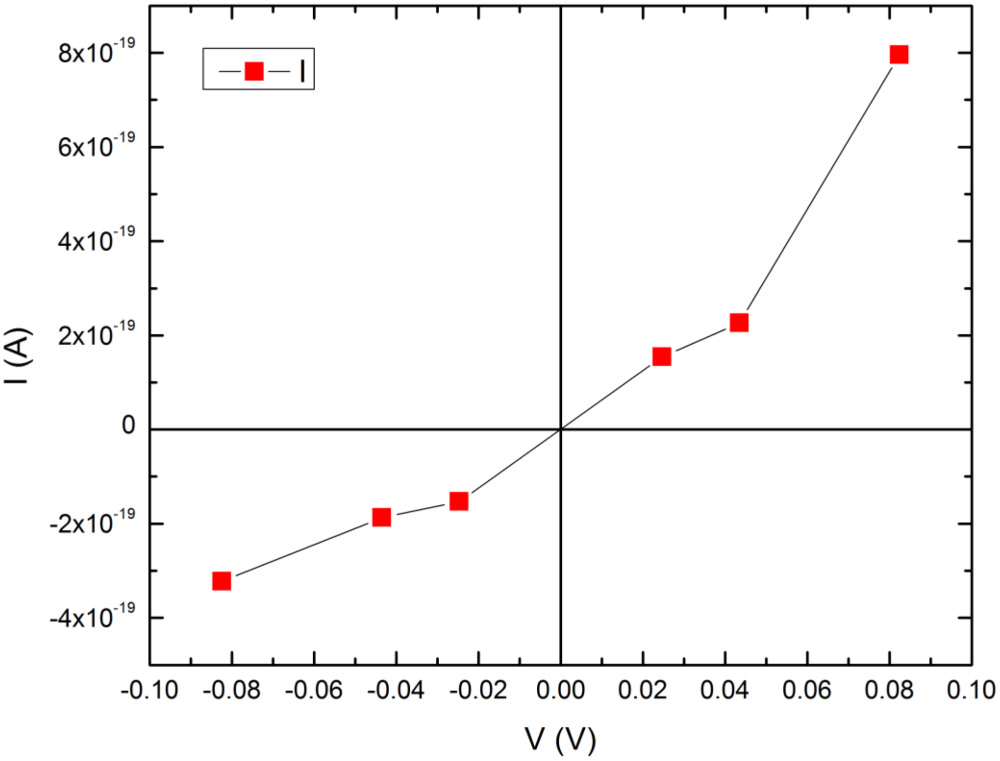

Figure 22: I/V characteristic of the Ag nanoplate-PVP-ITO interface. The values on the left of the vertical central axis correspond to the values of activation time constants while the values on the right correspond to relaxation time constants. All the data points are associated with different power densities. The points closer to the central vertical axis correspond to lower power densities and *vice versa*.

When a metal is deposited on the surface of an n-type semiconductor, there is a charge transfer of electrons from the particle to the semiconductor or *vice versa* until an equilibrium is reached by creating charged areas of opposite sign in both sides of the interface. The amount and direction of charge moved through the interface depends on the relative position of the Fermi Levels of metal and semiconductor. This is called metal-semiconductor junction or Schottky Junction (SJ)[51] and has been reported by Kittel & Roduner[68] and others[69] for a number of combinations of different metallic nanoparticles and semiconductors. SJ can present both ohmic or rectifying behaviour depending on the doping level of the semiconductor, the type of metal and the surface states of the metal-semiconductor interface[70]. So if the SJ is rectifying, electrons trying to cross the SJ will experience a different resistance depending on which way they are crossing due to an asymmetric potential barrier, in which case, the SJ forms a Schottky diode.

The fact that the Ag nanoplate-PVP-ITO system fulfils the conditions for the formation of a SJ and that it shows a rectifying behaviour, $R_{\mathrm{ON}} \neq R_{\mathrm{OFF}}$, leads to the idea that a rectifying SJ might be present. In our case, the SJ appears to create an asymmetric potential barrier on the Ag-PVP-ITO junction (Sect.5.5.7) so that electrons tunnel more easily from the Ag to the ITO than *vice versa* causing a rectifying behaviour that explains the asymmetric shape of the activation and relaxation transients.

Schottky diodes operate basically in two modes: Reverse mode and Forward mode. In reverse mode, electrons travel from the metal to the semiconductor through a potential barrier φ_{b} of fixed magnitude called Schottky barrier. In Forward mode, electrons travel from the semiconductor to the metal by overcoming a barrier φ_{i} that is smaller than that for Reverse mode. This causes the current to be higher in Forward mode than in Reverse mode. Taking this into account, it is possible to infer that the 'activation' transient is operating in Reverse mode while the 'relaxation' transient operates in Forward mode.

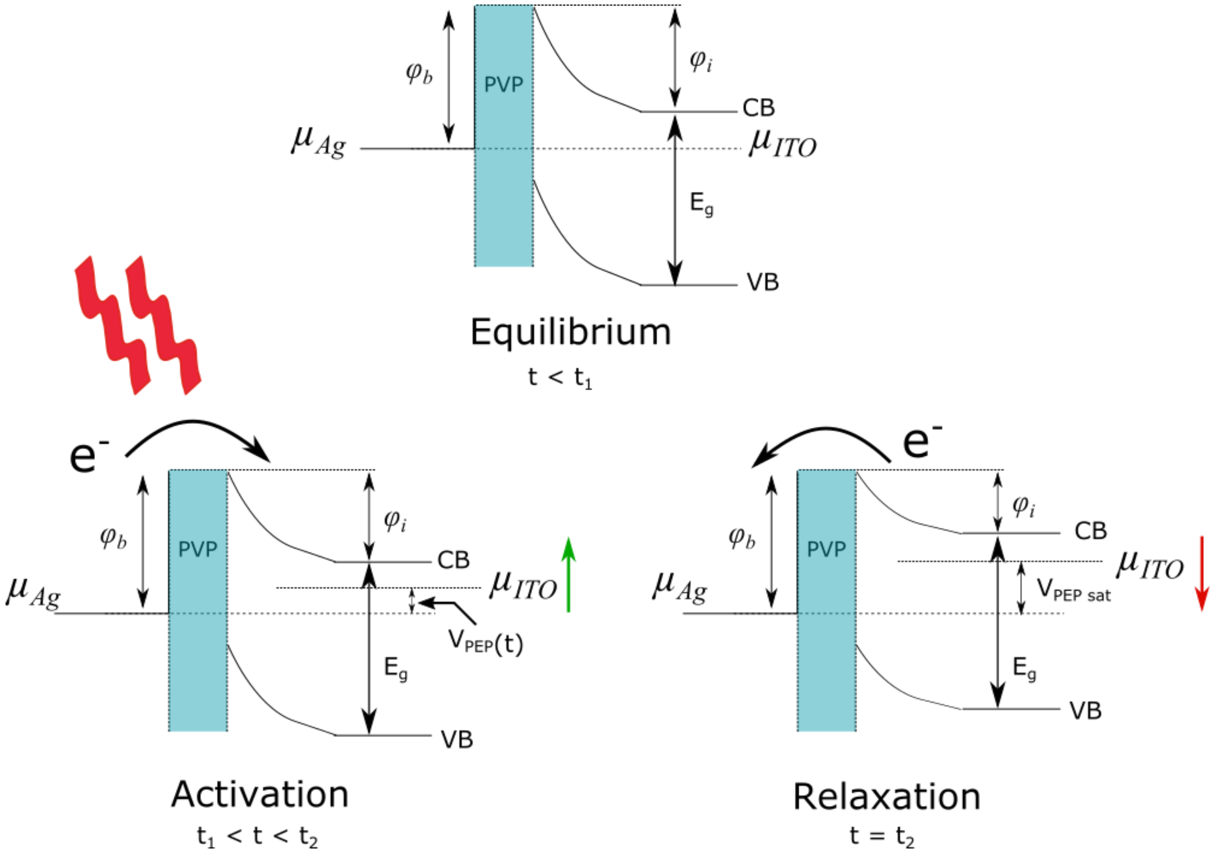

Figure 23: Band diagram of the Ag-PVO-ITO junction showing the potential barriers for the electrons under different conditions. μ_{Ag} is the electrochemical potential for Ag, μ_{ITO} is the electrochemical potential for ITO, CB is the conduction band, VB is the valence band, E_g is the band gap, φ_b is the potential barrier for an electron that wants to move from the Ag to the ITO also known as Schottky barrier and φ_i is the potential barrier for an electron that wants to move from the ITO to the Ag. t_1 represents the time when the illumination is activated while t_2 represents the time when illumination is deactivated. For a clearer picture of t_1 and t_2 see Fig.26.

During the activation transient, electrons flow from the Ag nanoplate towards the ITO (see Fig.23) and accumulate on its surface. This shortage of charge lowers the Fermi level of the Ag nanoplate (...or increases the Fermi level of ITO, depending on the reference point) and on the other side of the interface the excess charge reduces the surface band bending of the ITO until an equilibrium is reached. This causes that the interface potential barrier for electrons on the semiconductor φ_{i} to be lowered. As the laser is switched off, the excess electrons on the ITO start returning to the Ag nanoplate. However, as the potential barrier for the electrons has been lowered, they can flow more easily towards the metal. Consequently, if the laser power density is increased, more electrons travel to the semiconductor which lowers the potential barrier for the semiconductor even further. This causes the relaxation time to decrease with increasing illumination power density. It is also worth mentioning that the difference between the Fermi levels of the metal and semiconductor when the illumination is active corresponds to the value of the PEP. Which, under under illumination attains the value of V_{sat}.

The shape of the I/V curve in Fig.22 exhibits a behaviour that deviates from that of the ideal rectifying Schottky diode since the reverse current is not much lower than the forward current. However, this can be explained by the fact that for small sized SJ, its properties change with respect to macroscopic junctions[69,71]. For nanoscale SJ, quantum tunnelling is the relevant charge transport mechanism which causes the reverse current to be proportionally higher than on their macroscopic counterparts as it has been shown by Smit *et al*[72].

Although a feasible reason for this disparity of resistance and potential barrier values has been explained above, the author would like to note that ours is not a classical electronic system but a plasmo-electronic system. Where a number of diverse effects are simultaneously taking place in different realms. Namely: LSP generation, charge transfer via quantum tunnelling and possibly band bending shifts due to charge accumulation/depletion. For this reason, the understanding of the phenomena on the junction calls for a more comprehensive analysis that is outside of the scope of this thesis and is material for further research.

5.5.7 Energy barriers at the Ag nanoplate-PVP-ITO junction

The physics of charge transfer between two conductors separated by a thin insulating film have been studied in depth by Sommerfeld & Bethe[73], Holm[74] and later expanded by Simmons[75]. Who found that the current that flows through a junction is dependent on the relative permittivity of the insulator, the gap distance and the voltage bias between electrodes.

Here we used Simmons's formula modified by Peng[76] for the tunnelling between conductors (on its low voltage variant) to obtain a rough estimate of the height of the potential barrier (φ) of the Ag-PVP-ITO junction in both directions:

$$J = J_0\left[\bar{\varphi}_1 e^{-A\sqrt{\bar{\varphi}_1}} - (\bar{\varphi}_1 + V)e^{-A\sqrt{(\bar{\varphi}_1+V)}}\right] \qquad (5.20)$$

$$J_0 = \frac{e}{2\pi h\Delta s} \quad , \qquad A = \frac{4\pi\Delta s\sqrt{2m}}{h} \qquad (5.21)$$

Where J is the current, φ is the height of the potential barrier and Δs is the gap distance. Fig.24 plots the potential barrier for the activation and relaxation transients against gap distance. We can see that the barrier height is highly dependent on the thickness, specially for small gaps. If we assume a gap of ≈ 2 nm, the barrier heights for the activation and relaxation transients are respectively: $\varphi_{\mathrm{ON}} = 4.192$ eV and $\varphi_{\mathrm{OFF}} = 4.029$ eV. Which means a $\Delta\varphi = 0.163$ eV.

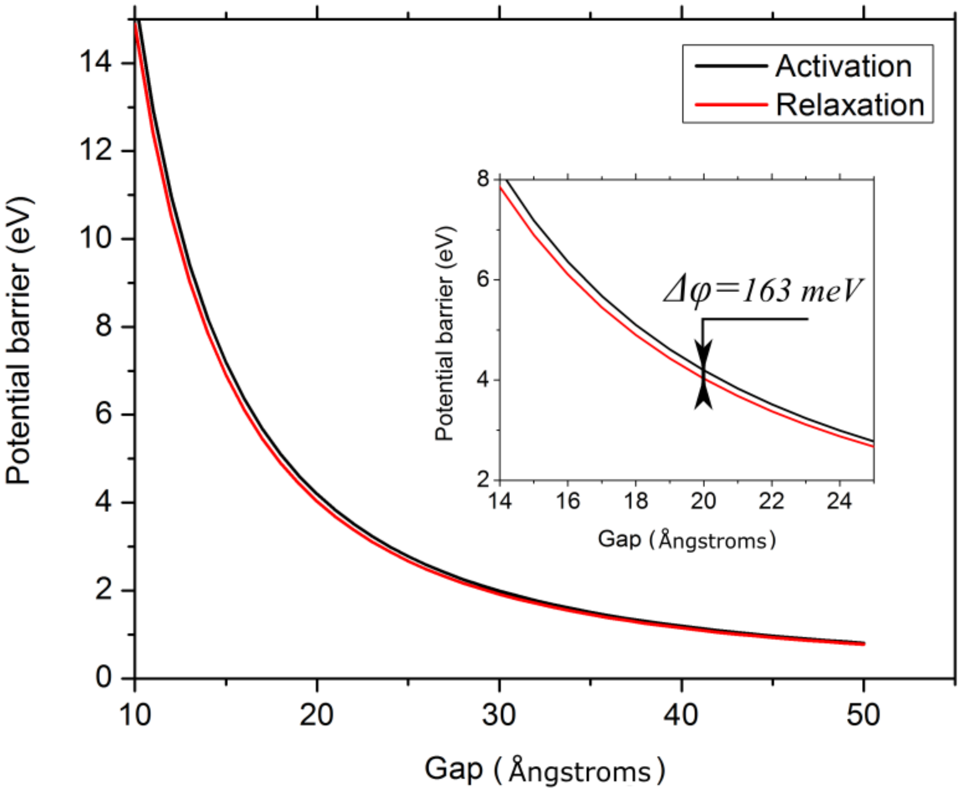

Figure 24: Ag-PVP-ITO barrier height against gap distance plot. Insert: Magnification of the plot on the 14-25 Å range. (Black line): Barrier height of the activation transient. (Red line): Barrier height for the relaxation transient.

These values show that there is a slightly asymmetric potential barrier on the junction which accounts for the different behaviour of activation and relaxation transients. Furthermore, these values show that electrons at room temperature (or at a few hundred °C) cannot overcome the potential barrier. Therefore, tunnelling seems like the only method of charge transport through the interface.

Conversely, it is worth considering that hot electrons with high energy produced on the Ag nanoplate might be able to overcome the potential barrier. The energies of the hot electrons produced on Au and Ag depend greatly on the size and the shape of the nanostructure. And they range from 1 eV to 4 eV [77]. So, as the potential barrier on our system is above the higher range for the hot electron energy, the contribution of hot electrons to the charge transport will be in principle considered negligible

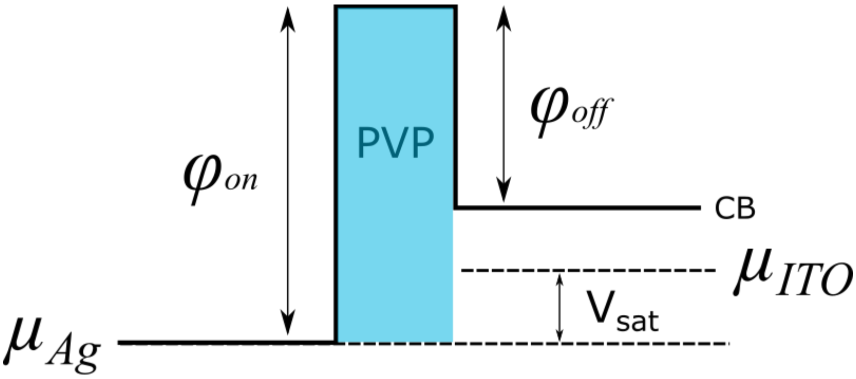

Figure 25: Representation of potential barriers between nanoplate and ITO.

5.5.8 Equivalent circuit of the system

Taking into consideration the conclusions from previous sections, the behaviour of the Ag nanoplate-PVP-ITO system regarding the PEP transients is technically a rectifying SJ or Schottky diode that is switched from reverse to forward and *vice versa* by plasmonic effects. However, this basic representation is not very useful when trying to model the data acquired from the system. Therefore, in this section it is proposed an equivalent electrical circuit describing the system with regards to PEP with its associated equations. The equations and the equivalent circuit are based on the theories and data presented on this study. So extending their use to other systems must be done with care until further experimental data can provide a more solid foundation.

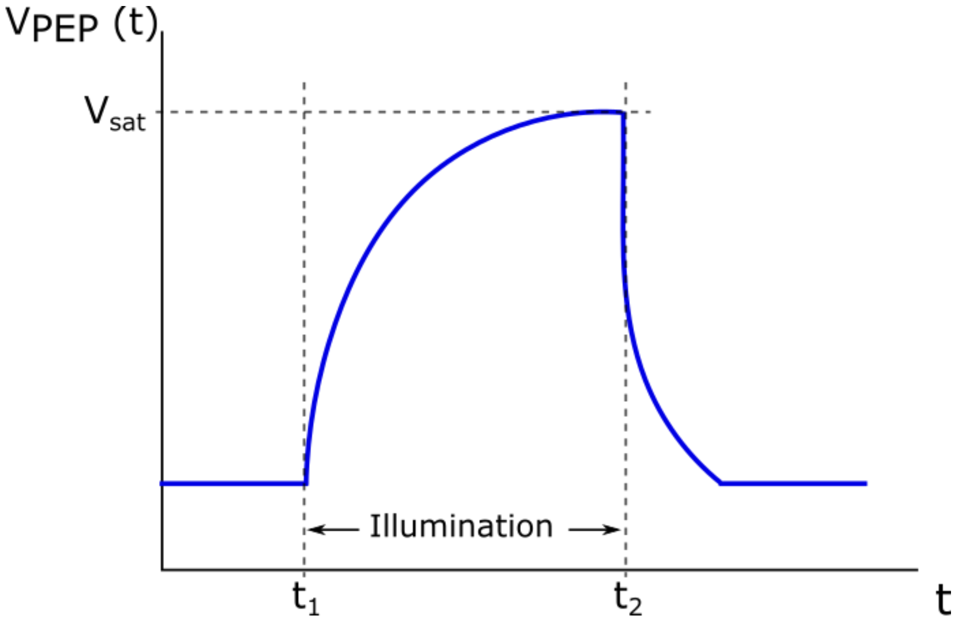

Figure 26: Diagram for a generic PEP transient.

If we consider a generic PEP transient curve like the one depicted in Fig.26, the activation transient ($t_1 \leq t < t_2$) can be described by the following equation:

$$V_{PEP_{ON}}(t) = V_{PEP_{sat}}\left(1 - e^{-\frac{t}{\tau_{ON}}}\right) \qquad (5.23)$$

If we take into account that $V_{\mathrm{PEP\ sat}}$ is a function of the illumination intensity (I_{L}) as shown previously (sect 5.4.2) and that τ_{ON} and τ_{OFF} are also dependent on I_{L}:

$$V_{PEP\ sat} = V_{PEP\ sat}(I_L) = a \cdot I_L^b \qquad (5.24)$$

$$\tau_{ON} = \tau_{ON}(I_L) = R_{ON}(I_L) \cdot C \qquad (25)$$

where *a* and *b* are coefficients. Then we obtain:

$$V_{PEP_{ON}}(t) = V_{PEP_{sat}}(I_L) \cdot \left(1 - e^{-\frac{t}{R_{ON}(I_L) \cdot C}}\right) \qquad (5.26)$$

Equally, the relaxation transient is described by:

$$V_{PEP_{OFF}}(t) = V_{PEP_{sat}}(I_L) \cdot e^{-\frac{t}{R_{OFF}(I_L) \cdot C}} \qquad (5.27)$$

Summarising:

$$V_{PEP}(t) \equiv \begin{cases} V_{PEP_{ON}}(t) = V_{PEP_{sat}}(I_L) \cdot \left(1 - e^{-\frac{t}{R_{ON}(I_L)\cdot C}}\right), & t_1 \leq t < t_2 \\ \\ V_{PEP_{OFF}}(t) = V_{PEP_{sat}}(I_L) \cdot e^{-\frac{t}{R_{OFF}(I_L)\cdot C}}, & t_2 \leq t \end{cases} \tag{5.28}$$

This set of equations (Eq.28) describe the behaviour of the Ag nanoplate-PVP-ITO system and can be translated into the circuit diagram depicted in Fig.27.

On the diagram, the PEP on the Ag nanoplate is modelled as a capacitor that charges through a resistor and discharges through a difference resistor. This scheme is achieved by placing two ideal diodes (with a zero forward threshold voltage) on each of the resistors' path with opposite direction.

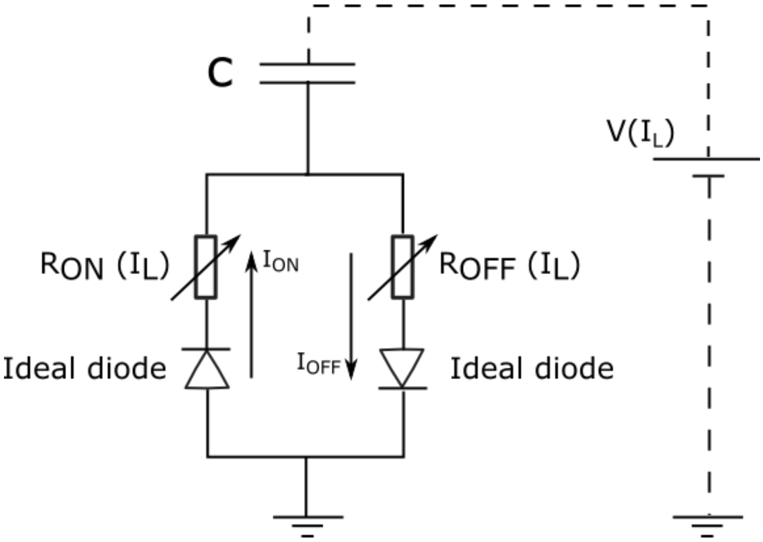

Figure 27: Equivalent circuit for the Ag nanoplate-PVP-ITO system regarding the PEP. The capacitor voltage represents the PEP.

Before proceeding any further, it is worth mentioning that at first glance the NC model proposed here might look similar to the model proposed by Benz *et al*[78] for coupled plasmonic systems, where they modelled plasmonic nanojunctions using capacitors and resistors[67]. However, the two models are intended to explain different phenomena despite being applied to similar but not comparable systems. Thus the two models don't enter in any contradiction. Benz *et al* elaborated a model to explain coupled plasmonic structures such as particle dimers or particle-on-mirror(metallic) systems; where dipoles induced by the excited nanoparticle can couple to the image charges on the substrate. But in our case, PEP is the phenomenon to be explained, the substrate is a semiconductor which is not a plasmonic material and it cannot couple to the plasmon. Also, their model works on the AC high frequency regime whereas the NC model works on the DC regime with electrostatic conditions.

5.6 Heterogeneous behaviour of plasmoelectric potentials on a single nanoplate

Illuminating the Ag nanoplate-PVP-ITO system causes a shift on the WF of the nanoplate that was identified as a PEP and explained on the previous sections. However, during this study it was found that upon illumination, in some spots on the nanoplate the WF would decrease while in others it would increase. Which is equivalent to having positive and negative PEP on the same nanoplate. This section examines this phenomenon and puts forward a hypothesis to explain this surprising behaviour.

5.6.1 Local dependence of the plasmoelectric potential sign

During this study, it was found that the sign of the PEP is different depending on the sampling point within the same Ag nanoplate. In Fig.28 is plotted the WF map of a single Ag nanoplate (without illumination) and the sampling points were the PEP transients were measured along with an indication of the PEP sign on each point. The PEP sign direction and magnitude are consistent and repeatable on each point. This behaviour is also present at low temperatures.

One of the first observation that can be made in Fig.28 is the fact that there seems to be a correlation between the initial WF of the area (without illumination) and the sign of the PEP. For example, red arrows in Fig.28 indicate sampling points where the WF increases during illumination. And all the red arrows are on areas where the initial WF is 4.5 eV or higher. Conversely, blue arrows are located in areas where the WF decreases under illumination. And the initial WF of those areas is 4.3 eV or lower.

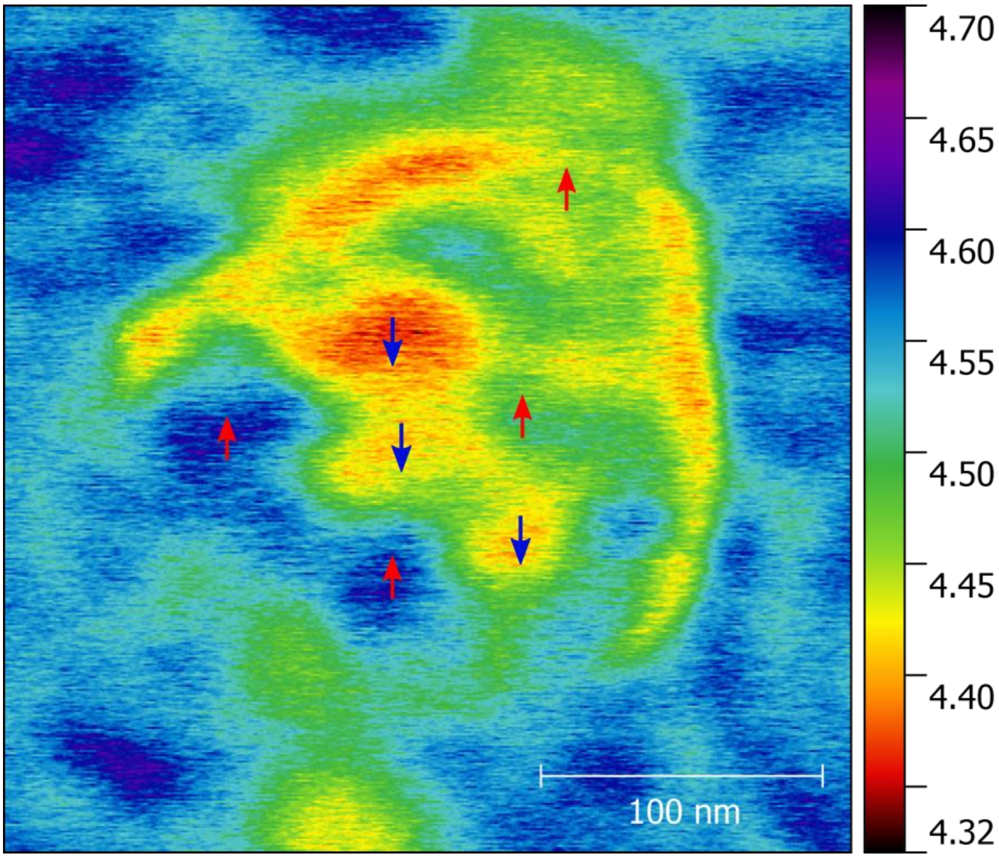

Figure 28: WF maps of an Ag nanoplate without illumination. Blue downward arrows indicate sampling points where the WF decreased under illumination. Red upward arrows indicate sampling points where the WF increased under illumination. The centre on the arrows is the actual sampling point.

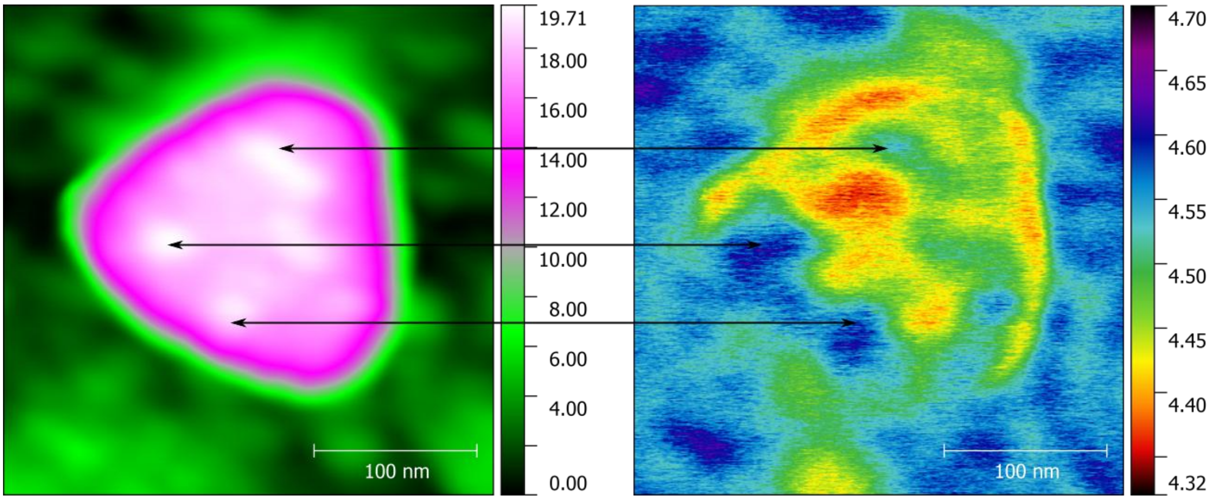

Figure 29: Comparison between topographic (left) and WF maps (right) of a Ag nanoplate. The black lines with double arrows point areas with protuberances on the Z image and their corresponding WF values on the WF map. The units of height on the z image are nm and the units of WF on the right image are eV.

Furthermore, we can examine the topographical map for the Ag nanoplate acquired simultaneously with WF maps and compare it with the latter. In Fig.29, the image comparison shows that areas with high WF painted in blue on the WF maps match in the topography maps with areas corresponding to small protuberances on top of the plate. These protuberances have a height of ≈2 nm (see sect 5.2.1) with respect to the top of the plate and are quasi-circular with diameters between 20 to 40 nm.

Another visualisation of this correlation is presented in Fig.30, where a WF map has been overlaid on top a topographical image rendered in 3D. Here it is possible to see the areas with high WF (blue and green colour) match the protuberances of the surface. While the rest of the plate is flat and has a lower WF.

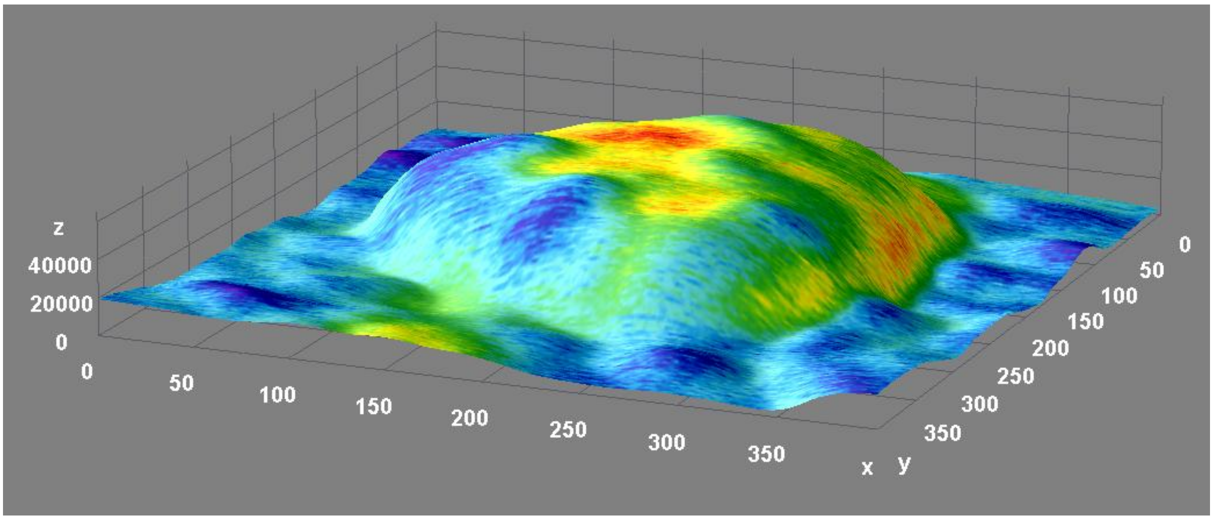

Figure 30: WF map overlaid on top a 3D rendering of a topography map of an Ag nanoplate. The image was elaborated with KPFM data.

Consequently, according to the data shown above, the local polarity of the PEP sign seems to be linked with areas that have a specific WF value which in turn match topographical features on top of the nanoplate.

An important aspect of the finding of PEP transients with opposite sign is the fact that they were not detected in the initial WF maps with and without illumination presented in sect.5.3 and especially in Fig.8. On the WF histograms of Fig.8 the WF peaks are so convoluted that it is not possible to detect the small peaks shifting to higher WF. This indicates that when studying PEP on nanoparticles with KPFM one has to proceed with caution.

5.6.2 Power dependence of plasmonic potentials on the protuberances of silver nanoplates

The PEP on the protuberances of the Ag nanoplate (see Fig.31) show a dependence with power, as the PEP studied on the Ag nanoplate plateaus. Although these transients seem to lose their shape at lower illumination intensities earlier than those in the plateaus. Their saturation voltages V_{sat} are plotted in Fig.32 along with those for the plateaus for comparison. Even though the saturation voltage for the plateaus seems to be higher at low illumination intensities. At higher illumination intensities it falls behind those of the plateaus. Furthermore, saturation voltages for the plateaus had a power dependence with an exponent of 4.5. Whereas the protuberances, still have a power dependence but with a lower exponent with a value of ≈2.5.

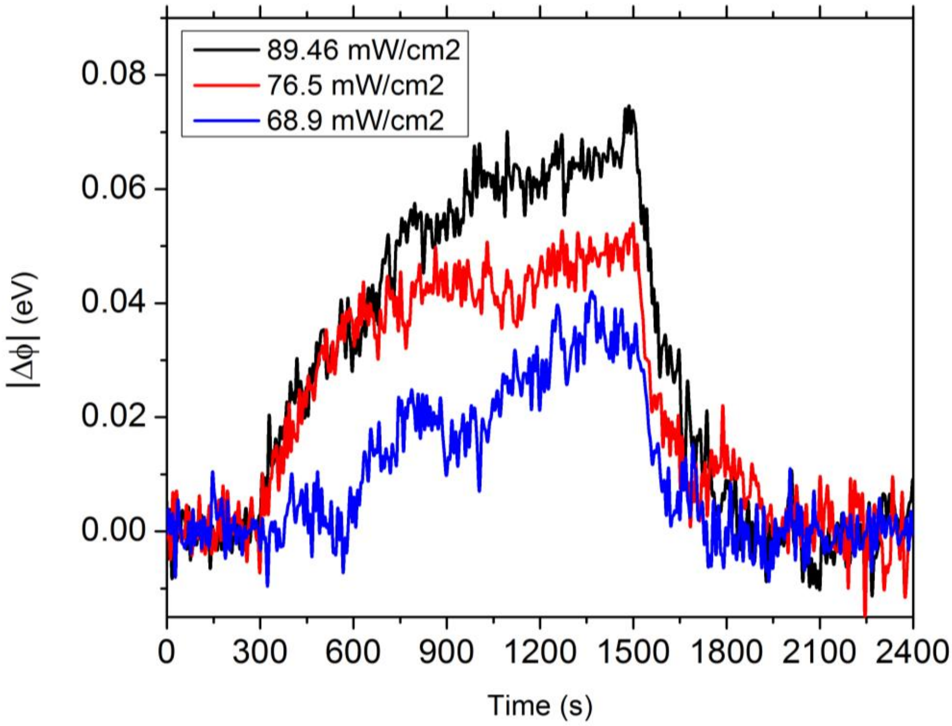

Figure 31: Work function shift transients on a single point on top of a protuberance of the Ag nanoplate for different illumination intensities (I_L).

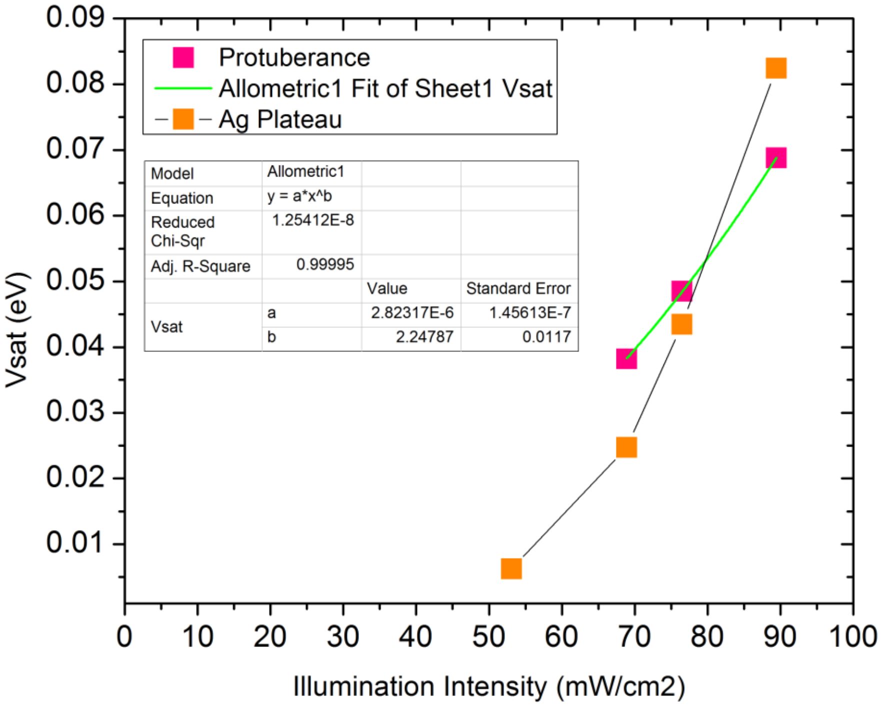

Figure 32: Saturation voltage (V_{sat}) plots. (Pink squares): V_{sat} for PEP transients on protuberances. (Orange squares): V_{sat} for PEP transients on Ag nanoplate plateaus. Green line shows the allometric function fitted to the data represented by pink squares.

Regarding the time constants for the activation and relaxation transients, they seem to be somehow higher on the protuberances (see Fig.33). Meaning the PEP in the protuberances are slower that in the plateaus. However, it is difficult to reach a final conclusion with the present data, so more experimental work is required on this regard.

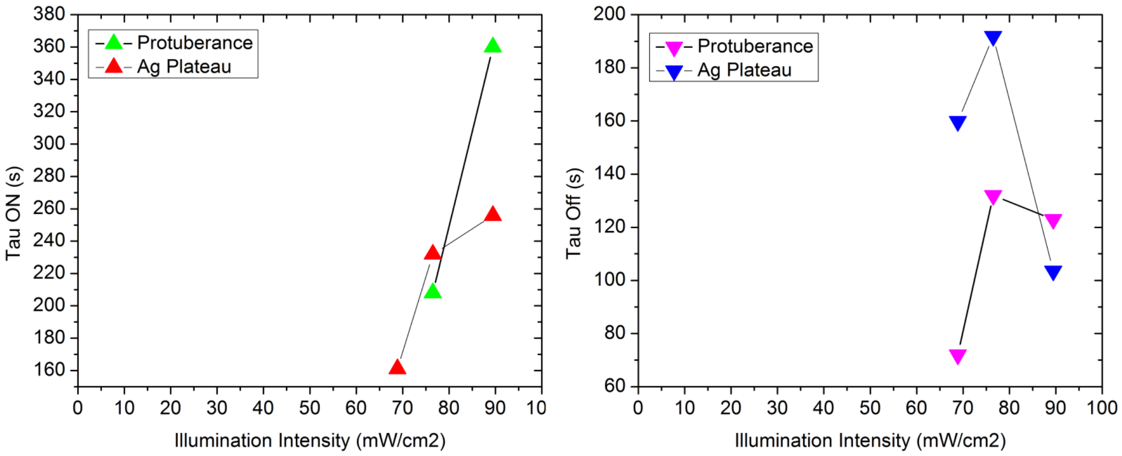

Figure 33: Time constant against Illumination intensity plots. (Left): Activation time constants (τ_{ON}). for protuberances (green triangles) and the plateaus (red triangles). (Right): Relaxation time constants (τ_{OFF}) for protuberances (pink triangles) and the plateaus (blue triangles).

5.6.3 Possible explanations for this phenomenon

According to the data presented until now, the sign of the PEP on the Ag nanoplate has a local dependence and it is related to the protuberances on the Ag nanoplate surface. These protuberances cannot be Ag (deformation or a dislocation of the Ag lattice) as if this was the case the PEP should have the same behaviour as the Ag on the plateaus. This is so because all the Ag on the nanoplate shares the same Fermi level. And the PEP is caused by a shift of the Fermi level. Therefore it cannot shift upwards in some places and downwards in other locations. Consequently, the protuberances have to be composed of a different material than the Ag nanoplate.

There is a number of substances that could be the origin on the protuberances. The PVP capping layer could be thicker in some parts of the plates so that it has a bulk behaviour, electronically speaking, rather than that of a thin film.

The Ag nanoplate synthesis by wet chemistry methods leaves residues that are not totally filtered out of the final product. So part of these residues could have deposited or attached to the Ag nanoplate and created the protuberances. These residues could be $AgNO_3$ for example as it is used commonly on Ag nanoparticle synthesis as a source of Ag atoms[79], or even extremely small Ag nanoparticles.

During the preparation of the samples, the colloidal Ag nanoplate solution was diluted and a very small quantity of HCl added to the mixture to prevent aggregation during the deposition process. So it is also a possibility that Cl^- ions have diffused through the PVP capping layer and reacted with Ag to for AgCl islands on the surface of the nanoplate.

Concerning the mechanism of how the protuberances also experience PEP. There are in principle two potential mechanisms:

-The protuberance is made of a plasmonic material and interacts with the incoming radiation: In this case, the protuberance is interacting with the incoming radiation on its own, somehow independently of the nanoplate. Therefore, a plasmon appears on the protuberance and causes an independent PEP by the same mechanism as the nanoplate. In this case the nanoplate would replace the ITO as a charge reservoir, and the characteristics of the transient would be determined by the nature of the protuberance-Ag interface.

-The protuberance is not a plasmonic material or if it is, it does not interact with the incoming radiation: In this case, the shift of the Fermi level, has to be caused by a charge transfer process with the Ag nanoplate excited by the laser. But while the nanoplate loses electrons and lowers its Fermi level, the protuberances gain electrons and raise their Fermi levels. So, if we imagine a sort of junction between Ag and protuberance where there is a charge double layer, akin of that of a pn junction or Schottky junction. The opposite behaviour of the Fermi level shift for the nanoplate and the protuberance under illumination shouldn't be possible. Which discards this hypothesis.

Therefore, the explanation for this phenomenon could be that the material of the protuberance somehow functions as an electron reservoir like the ITO substrate. Therefore, once the nanoplate is illuminated, it expels electrons towards wherever it can, including the protuberances. This causes the Fermi level of the protuberances to increase with the excess electrons while the Ferni level of the nanoplate decreases.

To sum up, this effect is very intricate because of the multiple physics involved and because the dimensions of the system place it already on the quantum realm. Where counterintuitive effects might be taking place that cause this phenomenon. Therefore, further studies targeting this specific matter are necessary to shed light over physics that govern it.

5.7 Conclusion

In this chapter, the PEP transients of Ag nanoplates on ITO under different illumination intensities have been studied as a potential method to tune the WF.

In order to explain the PEP transients it was proposed that the Ag nanoplate-PVP-ITO system behaves like a nanocapacitor. Whose charging and discharging is triggered by laser illumination. The PEP were found to happen at low temperatures. Which confirmed that the cause for the PEP is not temperature related. The time constants for the activation and relaxation time of the PEP are of the order of hundreds of seconds and follow a decaying exponential trend. Which is believed to be caused by the slow charge transport rate through the nanoplate-ITO interface.

Upon analysis of the Ag-PVP-ITO interface, it was concluded that the charge transfer mechanism is quantum tunnelling. Which in turn explains the high resistance of the PVP interface and the high values of the time constants.

Furthermore it was reported that the sign of PEP has a local dependence within the Ag nanoplates. The sign inversion is related with protuberances on the surface of the Ag nanoplate that could made of a different material than Ag. However, the mechanism for this phenomenon is still not clear.

This study was the first one to date that studied the PEP transients on nanoparticles. Its results, summarised above, shed light over the mechanics of the still novel field of PEP and offer possibilities to open new research paths. The fact that there are PEP of opposite signs on a nanoparticle can have important implications for plasmon assisted catalysis[80,81] , where the WF of the catalyst has important implications for the charge transfer with reactants. Also the reported time constants for some plasmon assisted catalytic processes with nanoparticles are of the same order of magnitude as the ones reported here[82]. Which points to a possible relation of plasmon assisted catalysis with PEP. Furthermore, Transient measurements of PEP seem a good tool to study the properties of molecular thin films. These could be placed on the interface between nanoparticle and substrate so that the transients would carry information about their electronic properties.

Acronyms

LSP: Localised Surface Plasmon.

PEP: Plasmoelectric Potential.

SP: Surface Potential

UHV: Ultra High Vacuum

ITO: Indium Tin Oxide

WF: Work Function

CPD: Contact Potential Difference

PVP: Polyvinylchloride

EELS: Electron Energy Loss Spectroscopy

TEM: Transmission Electron Microscopy

EF-PEEM: Energy Filtered Photoelectric Electron Microscope

NC: Nanocapacitor

SJ: Schottky Junction

List of figures

References

1. Sheldon, M. T., van de Groep, J., Brown, a. M., Polman, A. & Atwater, H. a. Plasmoelectric potentials in metal nanostructures. *Science* **828,** (2014).

2. Nonnenmacher, M., O'Boyle, M. P. & Wickramasinghe, H. K. Kelvin probe force microscopy. *Applied Physics Letters* **58,** 2921 (1991).

3. van de Groep, J., Sheldon, M. T., Atwater, H. A. & Polman, A. Thermodynamic theory of the plasmoelectric effect. *Scientific Reports* **6,** 23283 (2016).

4. Nano Composix. 1050 nm Resonant PVP NanoXact ^{TM} Silver Nanoplates. 92111 Available at: https://tools.nanocomposix.com:48/cdn/coa/Silver/Nanoplates/1050 Resonant PVP_NX_Low_ Ag_ Plates_DMW0162.pdf?012 445.

5. Rodríguez-González, B., Pastoriza-Santos, I. & Liz-Marzán, L. M. Bending Contours in Silver Nanoprisms. *The Journal of Physical Chemistry B* **110,** 11796–11799 (2006).

6. López-García, M. *et al.* Enhancement and Directionality of Spontaneous Emission in Hybrid Self-Assembled Photonic-Plasmonic Crystals. *Small* **6,** 1757–1761 (2010).

7. Maier, S. A. *Plasmonics: Fundamentals and Applications*. **1,** (Springer US, 2007).

8. Barnes, W. L. Surface plasmon–polariton length scales: a route to sub-wavelength optics. *Journal of Optics A: Pure and Applied Optics* **8,** S87–S93 (2006).

9. Kreibig, U. & Vollmer, M. *Optical Properties of Metal Clusters*. **25,** (Springer Berlin Heidelberg, 1995).

10. Pastoriza-Santos, I. & Liz-Marzan, L. M. Colloidal silver nanoplates. State of the art and future challenges. *Journal of Materials Chemistry* **18,** 1724–1737 (2008).

11. D. Steiner, E. P. G. An Equation for the Prediction of Bare Work Functions. *Proc. 27th Conf. on Phys. Electronics* 160–168 (1967).

12. Chelvayohan, M. & Mee, C. H. B. Work function measurements on (110), (100) and (111) surfaces of silver. *Journal of Physics C: Solid State Physics* **15,** 2305–2312 (1982).

13. Dweydari, A. W. & Mee, C. H. B. Work function measurements on (100) and (110)

surfaces of silver. *Physica Status Solidi (a)* **27,** 223–230 (1975).

14. Shim, J. W. *et al.* Polyvinylpyrrolidone-modified indium tin oxide as an electron-collecting electrode for inverted polymer solar cells. *Applied Physics Letters* **101,** 73303 (2012).

15. Lampande, R., Kim, G. W., Pode, R. & Kwon, J. H. Effectiveness of a polyvinylpyrrolidone interlayer on a zinc oxide film for interfacial modification in inverted polymer solar cells. *RSC Adv.* **4,** 49855–49860 (2014).

16. Zhou, Y. *et al.* A Universal Method to Produce Low-Work Function Electrodes for Organic Electronics. *Science* **336,** 327–332 (2012).

17. Sharma, A., Kippelen, B., Hotchkiss, P. J. & Marder, S. R. Stabilization of the work function of indium tin oxide using organic surface modifiers in organic light-emitting diodes. *Applied Physics Letters* **93,** 163308 (2008).

18. Destruel, P. *et al.* Influence of indium tin oxide treatment using UV–ozone and argon plasma on the photovoltaic parameters of devices based on organic discotic materials. *Polymer International* **55,** 601–607 (2006).

19. Schlaf, R., Murata, H. & Kafafi, Z. . Work function measurements on indium tin oxide films. *Journal of Electron Spectroscopy and Related Phenomena* **120,** 149–154 (2001).

20. Kim, S. Y., Lee, J.-L., Kim, K.-B. & Tak, Y.-H. Effect of ultraviolet–ozone treatment of indium–tin–oxide on electrical properties of organic light emitting diodes. *Journal of Applied Physics* **95,** 2560–2563 (2004).

21. Sugiyama, K., Ishii, H., Ouchi, Y. & Seki, K. Dependence of indium–tin–oxide work function on surface cleaning method as studied by ultraviolet and x-ray photoemission spectroscopies. *Journal of Applied Physics* **87,** 295–298 (2000).

22. Andrade, H. D. *et al.* Use of energy-filtered photoelectron emission microscopy and Kelvin probe force microscopy to visualise work function changes on diamond thin films terminated with oxygen and lithium mono-layers for thermionic energy conversion. *International Journal of Nanotechnology* **x,** 1–12 (2014).

23. Sheldon, M. T. *et al.* Nanophotonics. Plasmoelectric potentials in metal nanostructures. *Science (New York, N.Y.)* **346,** 828–31 (2014).

24. Brown, A. M., Sundararaman, R., Narang, P., Goddard, W. A. & Atwater, H. A. Nonradiative Plasmon Decay and Hot Carrier Dynamics: Effects of Phonons, Surfaces, and Geometry. *ACS Nano* **10,** 957–966 (2016).

25. Brongersma, M. L., Halas, N. J. & Nordlander, P. Plasmon-induced hot carrier science and technology. *Nature Nanotechnology* **10,** 25–34 (2015).

26. Link, S. & El-Sayed, M. A. Shape and size dependence of radiative, non-radiative and photothermal properties of gold nanocrystals. *International Reviews in Physical Chemistry* **19,** 409–453 (2000).

27. Hölzl, J., Schulte, F. K. & Wagner, H. *Solid Surface Physics*. **85,** (Springer-Verlag, 1979).

28. Malov, J. I., Shebzukhov, M. D. & Lazarev, V. B. Work functions of binary alloy systems with different kinds of phase diagrams. *Surface Science* **44,** 21–28 (1974).

29. Shott, M. & Walton, A. J. Changes in the chemical potential of tin on becoming superconducting. *Physics Letters A* **60,** 53–54 (1977).

30. Hill, R. V., Stefanakos, E. K. & Tinder, R. F. Changes in the Work Function of Iron in the α⇌γ Transformation Region. *Journal of Applied Physics* **42,** 4296–4298 (1971).

31. Ramanathan, K. G., Yen, S. H. & Estalote, E. A. Total hemispherical emissivities of copper, aluminum, and silver. *Applied Optics* **16,** 2810 (1977).

32. Lang, N. D. & Kohn, W. Theory of Metal Surfaces: Work Function. *Physical Review B* **3,** 1215–1223 (1971).

33. O'Donnell, K. M. *et al.* Diamond Surfaces with Air-Stable Negative Electron Affinity and Giant Electron Yield Enhancement. *Advanced Functional Materials* n/a-n/a (2013). doi:10.1002/adfm.201301424

34. Maier, F., Ristein, J. & Ley, L. Electron affinity of plasma-hydrogenated and chemically oxidized diamond (100) surfaces. *Physical Review B* **64,** 165411 (2001).

35. Ibach, H. *Physics of Surfaces and Interfaces*. (Springer Berlin Heidelberg, 2006). doi:10.1007/3-540-34710-0

36. Tsiplakides, D., Neophytides, S. & Vayenas, C. G. Investigation of electrochemical

promotion using temperature- programmed desorption and work function measurements. *Solid State Ionics* **136–137,** 839–847 (2000).

37. Rehn, V. & Rosenberg, R. A. in *Synchrotron Radiation Research* **1,** 327–381 (Springer US, 1992).

38. Pate, B. B., Hecht, M. H., Binns, C., Lindau, I. & Spicer, W. E. Photoemission and photon- stimulated ion desorption studies of diamond(111): Hydrogen. *Journal of Vacuum Science and Technology* **21,** 364–367 (1982).

39. Hoheisel, W., Jungmann, K., Vollmer, M., Weidenauer, R. & Träger, F. Desorption stimulated by laser-induced surface-plasmon excitation. *Physical Review Letters* **60,** 1649–1652 (1988).

40. King, D. A. Thermal desorption from metal surfaces: A review. *Surface Science* **47,** 384–402 (1975).

41. Thomas, R. E., Rudder, R. A. & Markunas, R. J. Thermal desorption from hydrogenated and oxygenated diamond (100) surfaces. *Journal of Vacuum Science & Technology A: Vacuum, Surfaces, and Films* **10,** 2451–2457 (1992).

42. Oura, K., Katayama, M., Zotov, A. V., Lifshits, V. G. & Saranin, A. A. *Surface Science*. (Springer Berlin Heidelberg, 2003). doi:10.1007/978-3-662-05179-5

43. Sivaiah, K., Kumar, K. N., Naresh, V. & Buddhudu, S. Structural and Optical Properties of Li+:PVP & Ag+: PVP Polymer Films. *Materials Sciences and Applications* **2,** 1688–1696 (2011).

44. Taylor, L. S. & Zografi, G. Spectroscopic characterization of interactions between PVP and indometacin in amophous molecular dispersions. *Pharmaceutical Research* **14,** 1691–1698 (1997).

45. Crivillers, N. *et al.* Photoinduced work function changes by isomerization of a densely packed azobenzene-based SAM on Au: a joint experimental and theoretical study. *Physical chemistry chemical physics : PCCP* **13,** 14302–14310 (2011).

46. Masillamani, A. M. *et al.* Light-induced reversible modification of the work function of a new perfluorinated biphenyl azobenzene chemisorbed on Au (111). *Nanoscale* **6,** 8969 (2014).

47. Méjard, R. *et al.* Energy-Resolved Hot-Carrier Relaxation Dynamics in Monocrystalline Plasmonic Nanoantennas. *ACS Photonics* **3,** 1482–1488 (2016).

48. Adleman, J. R., Boyd, D. A., Goodwin, D. G. & Psaltis, D. Heterogenous catalysis mediated by plasmon heating. *Nano Letters* **9,** 4417–4423 (2009).

49. Coates, D. An electron microscopy study of the low temperature catalyzed steam gasification of graphite. *Journal of Catalysis* **80,** 215–220 (1983).

50. Tysoe, T., Yee, G. & Casanova, R. Low temperature methane production by the catalyzed reaction of graphite and water vapor. 77–78

51. Neil W. Ashcroft and N. David Mermin. *Solid state physics*. (Saunders College, 1976).

52. Hugh D. Young, Freedman A., R. & Ford, A. L. *University physics with modern physics*. (Addison-Wesley, 2013).

53. Rawat, A., Mahavar, H. K., Tanwar, A. & Singh, P. J. Dielectric relaxation studies of polyvinylpyrrolidone (PVP) and polyvinylbutyral (PVB) in benzene solutions at microwave frequency. *Indian Journal of Pure and Applied Physics* **52,** 632–636 (2014).

54. Khan, W. S., Asmatulu, R. & Eltabey, M. M. Dielectric Properties of Electrospun PVP and PAN Nanocomposite Fibers at Various Temperatures. *Journal of Nanotechnology in Engineering and Medicine* **1,** 41017 (2010).

55. Bohn, D. *Quantum theory*. (Dover Publications, 1989).

56. Pérez-González, O. *et al.* Optical Spectroscopy of Conductive Junctions in Plasmonic Cavities. *Nano Letters* **10,** 3090–3095 (2010).

57. van Wees, B. J. *et al.* Quantized conductance of point contacts in a two-dimensional electron gas. *Physical Review Letters* **60,** 848–850 (1988).

58. Feng, H. & Fichthorn, K. a. Adsorption of Polyvinylpyrrolidone on Ag Surfaces: Insight into a Structure-Directing Agent. *Nano letters* **12,** 997–1001 (2012).

59. Sheng, P., Sichel, E. K. & Gittleman, J. I. Fluctuation-Induced Tunneling Conduction in Carbon-Polyvinylchloride Composites. *Physical Review Letters* **40,** 1197–1200 (1978).

60. Zhu, X. *et al.* Nanostructural instability of single-walled carbon nanotubes during electron beam induced shrinkage. *Carbon* **49,** 3120–3124 (2011).

61. Sheng, P. Fluctuation-induced tunneling conduction in disordered materials. *Physical Review B* **21,** 2180–2195 (1980).

62. Bao, W. S., Meguid, S. A., Zhu, Z. H. & Weng, G. J. Tunneling resistance and its effect on the electrical conductivity of carbon nanotube nanocomposites. *Journal of Applied Physics* **111,** (2012).

63. Hwang, J., Shim, Y., Yoon, S.-M., Lee, S. H. & Park, S.-H. Influence of polyvinylpyrrolidone (PVP) capping layer on silver nanowire networks: theoretical and experimental studies. *RSC Adv.* **6,** 30972–30977 (2016).

64. Brooke, R. J. *et al.* Single-Molecule Electrochemical Transistor Utilizing a Nickel-Pyridyl Spinterface. *Nano Letters* **15,** 275–280 (2015).

65. Wu, L. *et al.* Fowler–Nordheim Tunneling Induced Charge Transfer Plasmons between Nearly Touching Nanoparticles. *ACS Nano* **7,** 707–716 (2013).

66. Sigle, D. O. *et al.* Observing Single Molecules Complexing with Cucurbit[7]uril through Nanogap Surface-Enhanced Raman Spectroscopy. *The Journal of Physical Chemistry Letters* **7,** 704–710 (2016).

67. Benz, F. *et al.* Nanooptics of Molecular-Shunted Plasmonic Nanojunctions. *Nano Letters* **15,** 669–674 (2015).

68. Kittel, T. & Roduner, E. Charge Polarization at Catalytic Metal-Support Junctions. Part A: Kelvin Probe Force Microscopy Results of Noble Metal Nanoparticles. *Journal of Physical Chemistry C* **120,** 8917–8926 (2016).

69. Hägglund, C. & Zhdanov, V. P. Charge distribution on and near Schottky nanocontacts. *Physica E: Low-dimensional Systems and Nanostructures* **33,** 296–302 (2006).

70. Tung, R. T. The physics and chemistry of the Schottky barrier height. *Applied Physics Reviews* **1,** 11304 (2014).

71. Pérez-García, B., Zúñiga-Pérez, J., Muñoz-Sanjosé, V., Colchero, J. & Palacios-Lidón,

E. Formation and Rupture of Schottky Nanocontacts on ZnO Nanocolumns. *Nano Letters* **7,** 1505–1511 (2007).

72. Smit, G. D. J., Rogge, S. & Klapwijk, T. M. Scaling of nano-Schottky-diodes. *Applied Physics Letters* **81,** 3852–3854 (2002).

73. Sommerfeld, A. & Bethe, H. in *Aufbau Der Zusammenhängenden Materie* 333–622 (Springer Berlin Heidelberg, 1933). doi:10.1007/978-3-642-91116-3_3

74. Holm, R. The Electric Tunnel Effect across Thin Insulator Films in Contacts. *Journal of Applied Physics* **22,** 569–574 (1951).

75. Simmons, J. G. Electric Tunnel Effect between Dissimilar Electrodes Separated by a Thin Insulating Film. *Journal of Applied Physics* **34,** 2581 (1963).

76. Zhang, P. Scaling for quantum tunneling current in nano- and subnano-scale plasmonic junctions. *Scientific Reports* **5,** 9826 (2015).

77. Clavero, C. Plasmon-induced hot-electron generation at nanoparticle/metal-oxide interfaces for photovoltaic and photocatalytic devices. *Nature Photonics* **8,** 95–103 (2014).

78. Benz, F. *et al.* Generalized circuit model for coupled plasmonic systems. *Optics Express* **23,** 33255 (2015).

79. Saidi, W. A., Feng, H. & Fichthorn, K. A. Binding of polyvinylpyrrolidone to Ag surfaces: Insight into a structure-directing agent from dispersion-corrected density functional theory. *Journal of Physical Chemistry C* **117,** 1163–1171 (2013).

80. Mukherjee, S. *et al.* Hot electrons do the impossible: Plasmon-induced dissociation of H 2 on Au. *Nano Letters* **13,** 240–247 (2013).

81. Mukherjee, S. *et al.* Hot-electron-induced dissociation of H2 on gold nanoparticles supported on SiO2. *Journal of the American Chemical Society* **136,** 64–67 (2014).

82. Christopher, P., Xin, H. & Linic, S. Visible-light-enhanced catalytic oxidation reactions on plasmonic silver nanostructures. *Nature Chemistry* **3,** 467–472 (2011).

I see no good reason why the views given in this volume should shock the religious feelings of any one.

-Charles Darwin

6

Conclusions

This thesis has examined the physics of two methods for the modification of the work function of a surface. One of them is well established and uses atom adsorption to modify the work function. This method is explored in relation to its application on hydrogenated diamond surfaces employed on thermionic emission devices. The other method consists of work function tuning *via* laser exited plasmo-electric potentials, which is studied with an exploratory approach in order to clarify the physics of this phenomenon.

In this chapter, a summary of the main findings is presented, along with suggestions for future work that would allow to continue with the research lines initiated in this thesis.

6.1 Use of molybdenum gratings as plasmonic heaters

In chapter 3 a method is presented for the heating of thin diamond films based on molybdenum plasmonic gratings. This method is intended to be used primarily to perform thermionic emission experiments on diamond thin films grown on molybdenum substrates. However, it can also be used for other purposes such as for temperature-dependence tests to measure the resistivity of diamond.

This plasmonic heating method is based on the illumination of a molybdenum substrate with a high-power laser. A plasmonic grating engraved on the molybdenum is used to increase its absorbance, which increases the maximum temperatures reached by the substrate. This allows to extend the range of temperatures at which the test can be performed.

This laser-based method has advantages over other heating alternatives (e.g. resistive heating). Firstly, is does not produce leakage currents or electrical noise that could interfere with the measurement of thermionic current. Secondly, the control of the temperature can be very accurate as the sample temperature can be maintained within 0.5 K of the set temperature. Finally, there is very little thermal inertia which enables the use of complex heating-cooling patterns or routines.

In this thesis, we explored the heating capabilities of a number of gratings with different design parameters, namely filling factor and grating period, in order to find the optimal values to maximise the highest temperature that the molybdenum substrates could reach. It was concluded that a plasmonic grating with a period of 10.6 μm and a filling factor of 20% reaches the highest temperature ($T_{\max}$ = 1011 °C), which is an increase of ≈ 150 % when compared to the temperature that a bare molybdenum substrate can reach ($T \approx$ 400 °C). The range of temperatures achieved by this method is more than sufficient to perform thermionic emission experiments on thin diamond films.

6.1.1 Future work

A possible route to further increase the temperature range of this heating method would be the use of tungsten instead of molybdenum as a substrate for the plasmonic grating. Preliminary finite element simulations carried out by our group show that tungsten would increase the maximum temperature by a few dozen degrees.

6.2 An alternative thermionic emission model for hydrogen terminated diamond surfaces

In chapter 4 we proposed a new theoretical model for the thermionic emission from hydrogenated diamond surfaces and validated it against experimental thermionic emission data obtained from a hydrogenated <100> single crystal surface.

The model currently used to describe the thermionic emission is the Richardson-Dushman equation, which assumes that the emitting surface is stable at all temperatures. However, this model fails to reproduce the effect of hydrogen desorption from the diamond surface on the thermionic current. This leads to poor fittings of the experimental data and to an inadequate extraction of parameters.

In our proposed model, we added a new term to the Richardson-Dushman equation that accounts for the variation of the work function as a function of the hydrogen surface coverage. The coverage is calculated using the Wigner-Polanyi equation for desorption kinetics.

The model was validated against experimental thermionic emission data from a hydrogenated <100> single crystal diamond surface. The result was that the proposed model is able to very successfully reproduce the experimental thermionic emission data. Moreover, the new model allowed the extraction of a series of parameters from the fitting, namely: Richardson constant, initial hydrogen coverage, frequency prefactor and activation energy of desorption.

Regarding the first two parameters, their values (A = 79 A/cm^2 K^2, υ = 2.7×10^{13} s^{-1}) are very close to their theoretical ones (A = 120 A/cm^2 K^2, υ = 1×10^{13} s^{-1}), which gives an indication of the good quality of the fitting and the strength of the model. The extracted values of the desorption energy agree with the ones reported in the literature, which were obtained with temperature programmed desorption experiments. This opens the door to the use of thermionic emission as a tool for surface analysis, when used in combination with the new thermionic model.

The thermionic emission from the hydrogenated <100> single crystal surface was found to have two main components with different desorption energies. One of them is likely to correspond to the contributions from the fully hydrogenated dimers on the flat terraces of the <100> surface, while the other component could be caused by either partially terminated dimers on the flat terraces or fully terminated dimers on the boundaries of these terraces.

Thermionic emission from hydrogenated polycrystalline diamond was also measured and the new model was successfully fitted to the experimental data, allowing the extraction of several surface parameters. However, even though the values of the extracted parameters were reasonable, due to the complexity of the polycrystalline surface, they have to be taken with some reserve.

When comparing the thermionic emission of single crystal and polycrystalline diamond, the single crystal proved to be a much better emitter with a maximum current of J_{max} = 1.5 mA/cm^2 while the polycrystalline diamond only produced 0.3 mA/cm^2. This means that a potential thermionic device would be more efficient if fabricated with single crystal diamond.

The information obtained with the new thermionic model allowed us to relate emission contributions to certain surface phases present in single crystal diamond. This gives an indication of how to improve the efficiency of a potential device by promoting the creation of a particular surface phase by the application of surface treatments.

6.2.1 Future work

Although the new thermionic emission model proved to be strong there are a couple of features that could be improved. One of them is the use of the work function as a free parameter for the fitting, which the model cannot do at the moment. The other is the use of a cubic function to describe the variation of the work function with the coverage, that at the moment is approximated with a linear piecewise function. Therefore, there is still potential for further developments of the model.

The model can also be improved by measuring the work function of hydrogenated diamond surfaces for different coverages with ultraviolet photoelectron spectroscopy, so that this data can be incorporated on the model to make it more accurate.

Additional thermionic emission tests should be done on the other single crystal surfaces of diamond to gain more understanding of its surface properties and the kinetics of hydrogen desorption.

6.3 Work function tuning *via* plasmo-electric potentials

The tuning of the work function *via* laser excited plasmo-electric potentials has been explored in this thesis. This line of research in quite novel, so the aim was to improve the understanding of the plasmo-electric potentials to see if they could be applied to tune the work function.

The focus of the research was on the transient behaviour of plasmo-electric potentials upon laser illumination on silver nanoplates deposited on indium tin oxide. It was found that the plasmo-electric potential transient have a nanocapacitor-like behaviour with long activation and relaxation time constants ($\tau \approx 100$ s). These values were found to be caused by the poor charge transfer capabilities of the nanoplate-substrate interface. The plasmo-electric potentials are caused by charge being transferred in or out of the nanoplates through the nanoplate-substrate interface. Consequently, poor charge transfer properties on this interface would lead to long time constants. The high resistance of the interface was found to be caused by the fact that the charge transfer mechanism is quantum tunnelling.

The maximum value of the plasmo-electric potentials under our illumination conditions (I_L = 89 mW/cm^2) was≈ 0.08 eV. V arying the illumination intensity led to the finding that both the magnitude of the plasmo-electric potentials and their time constants show a strong dependence with I_L, which agrees with other published studies.

We also report on the fact that the sign of the plasmo-electric potential can change within the same nanoplate. This behaviour was unexpected and it is theorised that it could be produced by the presence of impurities on the surface on the nanoplates.

This is the first study, to the best of the author's knowledge, that analyses the plasmo-electric potential transient behaviour on plasmonic nanoparticles. It also offers a good insight on the mechanism of this phenomenon by highlighting the importance of the nanoparticle-substrate interface. We adventure to suggest that this finding could be used to study the properties of molecular or atomic monolayers placed on the nanoparticle-substrate interface. Conversely, taking into account the value of the time constants for the plasmo-electric potentials and some reports on plasmon assisted catalysis, lead us to think that there could be a relation between the two phenomena that has not been uncovered yet.

6.3.1 Future work

The field of plasmo-electric potentials is still at an early development stage where more work needs to be done, both theoretically and experimentally, to fully comprehend this phenomenon.

As a continuation of the experiments reported here, it would be interesting to repeat the experiment with silver nanoplates deposited on a metal substrate instead of indium tin oxide, to see is plasmo-electric potentials are still present.

As mentioned on the previous section, changing the characteristics of the nanoparticle-substrate interface with molecular or atomic monolayers, could lead to interesting findings.

Lastly, studying the possible relation between plasmo-electric potentials and plasmon-assisted catalysis could bring a potential breakthrough in the understanding of this type of catalysis.